

Technical Basis for Scaling of Air Sparging Systems for Mixing in Non-Newtonian Slurries

A. P. Poloski	B. G. Fritz
S. T. Arm	R. P. Mueller
J. A. Bamberger	F. Nigl
B. Barnett	Y. Onishi
R. Brown	L. A. Schienbein
B. J. Cook	L. A. Snow
C. W. Enderlin	S. Tzemos
M. S. Fountain	M. White
M. Friedrich	J. A. Vucelick

February 2005

Prepared for Bechtel National, Inc.
under Contract 24590-101-TSA-W000-00004

LEGAL NOTICE

This report was prepared by Battelle Memorial Institute (Battelle) as an account of sponsored research activities. Neither Client nor Battelle nor any person acting on behalf of either:

MAKES ANY WARRANTY OR REPRESENTATION, EXPRESS OR IMPLIED, with respect to the accuracy, completeness, or usefulness of the information contained in this report, or that the use of any information, apparatus, process, or composition disclosed in this report may not infringe privately owned rights; or

Assumes any liabilities with respect to the use of, or for damages resulting from the use of, any information, apparatus, process, or composition disclosed in this report.

Reference herein to any specific commercial product, process, or service by trade name, trademark, manufacturer, or otherwise, does not necessarily constitute or imply its endorsement, recommendation, or favoring by Battelle. The views and opinions of authors expressed herein do not necessarily state or reflect those of Battelle.

Technical Basis for Scaling of Air Sparging Systems for Mixing in Non Newtonian Slurries

A. P. Poloski	B. G. Fritz
S. T. Arm	R. P. Mueller
J. A. Bamberger	F. Nigl
B. Barnett	Y. Onishi
R. S. Brown	L. A. Schienbein
B. J. Cook	L. A. Snow
C. W. Enderlin	S. Tzemos
M. S. Fountain	M. White
M. Friedrich	J. A. Vucelick

February 2005

Test specification: 24590-WTP-TSP-RT-03-006, Rev. 0


Test plan: TP-RPP-WTP-290 Rev 0

Test exceptions: 24590-WTP-TEF-RT-04-00008
24590-WTP-TEF-RT-04-00020

R&T focus area: Pretreatment & Vitrification

Test Scoping Statement(s): B-100

Battelle—Pacific Northwest Division
Richland, Washington 99352


for W. Tamosady 3/4/05
ACCEPTED FOR
WTP PROJECT USE

Completeness of Testing

This report describes the results of work and testing specified by Test Specification 24590-WTP-TSP-RT-03-006, Rev. 0 and Test Plan TP-RPP-WTP-290 Rev. 0. The work and any associated testing followed the quality assurance requirements outlined in the Test Specification/Plan. The descriptions provided in this test report are an accurate account of both the conduct of the work and the data collected. Test plan results are reported. Also reported are any unusual or anomalous occurrences that are different from expected results. The test results and this report have been reviewed and verified.

Approved:



Gordon H. Beeman, Manager
WTP R&T Support Project



Date

Summary

Objectives

This investigation was conducted according to the Test Plan TP-RPP-WTP-290 Rev 0 “Additional Sparger Scaling Zone of Influence Tests to be run in Small and Large-Scale Test Platforms” in response to the test specification 24590-WTP-TSP-RT-03-006, Rev. 0, “Determination of PJM Design Parameter Scale Laws for Scaled Testing.” The test objective was satisfied. A summary of the test objective and how it was satisfied is provided in Table S.1.

Table S.1. Test Objective Evaluation

Test Objective	Objective Met (Y/N)	Discussion
Provide assessment of pulse jet mixer (PJM) operating parameters on waste mobilization and potential mixing effectiveness on selected non-Newtonian waste streams anticipated for the Waste Treatment Plant (WTP).	Yes	This report contains data that can be used by WTP engineers to design a sparging system for PJM vessels. The combination of sparging and PJM operation should provide an effective waste mobilization strategy for the WTP.

Test Exceptions

Table S.2 discusses the test exceptions applied to this test.

Table S.2. Test Exceptions

List Test Exceptions	Describe Test Exceptions
24590-WTP-TEF-RT-04-00008	Testing is needed to determine the performance of sparge tubes for mixing and to enable the design of a satisfactory hybrid (PJM/sparge) mixing system.
24590-WTP-TEF-RT-04-00020	Additional single- and multi-tube sparger large-scale testing are needed to determine the performance of proposed multi-tube sparge tube configurations for mixing and to provide a satisfactory hybrid (PJM/sparge) mixing system design and operational understanding.

Results and Performance Against Success Criteria

Table S.3 discusses the success criterion provided in Test Specification 24590-WTP-TSP-RT-03-006, Rev. 0 “Determination of PJM Design Parameter Scale Laws for Scaled Testing.”

Table S.3. Discussion of Test Success Criterion

List Success Criteria	Explain How the Tests Did or Did Not Meet the Success Criteria
Zone of influence (profile and volume) will be determined as a function of air-flow rate and sparger submergence using a single sparge tube located where there is minimum tank wall boundary influence.	The tests did meet success criterion. A series of such tests were performed and are discussed in Section 6.0 of this report.
Zone of influence (profile and volume) and tank contents flow will be determined as appropriate, as a function of air-flow rate for a sparger array (such as three spargers forming an equilateral triangle) based on the single sparger testing results (to determine sparger spacing and submergence). The array configuration may be varied during testing.	The tests did not meet success criterion. This test criterion is described in 24590-WTP-TEF-RT-04-00008. A later test exception, 24590-WTP-TEF-RT-04-00020, provides revised guidance on the performance of such multi-tube sparging tests. For this reason, these tests were not performed in the manner described in the previous test exception 24590-WTP-TEF-RT-04-00008.
Zone of influence (profile and volume) will be determined, as appropriate, as a function of air-flow rate for a PJM and/or sparger array using various sparging patterns (such as sequential tube/PJM air flow and intermittent tube/PJM air flow). Tests using PJMs will utilize the current 4-PJM setup in the supernatant tank.	The tests did not meet success criterion. This test criterion is described in 24590-WTP-TEF-RT-04-00008. A later test exception, 24590-WTP-TEF-RT-04-00020, addresses a large scale PJM/sparging demonstration task in a different manner. For this reason, these tests were not performed in the manner described.
Aerosol entrainment during sparging will be conducted in consultation with WTP project cognizant engineers.	The tests did meet success criterion. A series of such tests were performed and are discussed in Section 11.0 of this report.
Determine the time to establish a steady-state velocity profile and provide a plot of zone of influence (ZOI) diameter versus time using surface measurements. Experiments will be conducted in a single sparge tube over an air-flow rate of 5 to 40 ACFM. If possible, measure and report the ZOI shape, both beneath the sparge tubes and above, over the bounding air-flow range. A velocity probe will be used to determine steady-state velocity.	The tests did meet success criterion. A series of ZOI surface measurement tests were performed and are discussed in Section 6.0 of this report. The tests did meet success criterion. A series of velocity probe measurement tests were performed to determine subsurface ZOI shape and time to reach steady-state flow. These tests are discussed in Section 7.0 of this report. Additional ZOI shape tests using passive integrated transponder (PIT) tag technology are discussed in Section 8.0.

Table S.3 (contd)

List Success Criteria	Explain How the Tests Did or Did Not Meet the Success Criteria
Determine the non-Newtonian slurry circulation time and provide a plot of circulation time through a single ZOI as a function of air-flow rate. Experiments will be conducted with a single sparge tube over an air-flow rate of 5 to 40 ACFM with multiple sparge tube heights.	The tests did meet success criterion. A series of tracer tests to determine circulation time through a ZOI were performed and are discussed in Section 10.0 of this report.
Determine the gas release characteristics of non-Newtonian simulants when agitated by a sparging system. The purpose of this task is to deliver a set of plots that show gas holdup levels as a function of time after sparging is initiated as a function of initial gas holdup.	The tests did meet success criterion. A series of gas retention and release tests were performed and are discussed in Section 12.0 of this report.
Determine the surface tension for non-Newtonian simulants.	The tests did meet the success criterion. A series of surface tension measurements were obtained with a Kaolin/Bentonite clay simulant and a pretreated AZ-101 slurry simulant. These results are provided in Appendix A.

Quality Requirements

PNWD implements the RPP-WTP quality requirements by performing work in accordance with the PNWD Waste Treatment Plant Support Project quality assurance project plan (QAPjP) approved by the RPP-WTP Quality Assurance (QA) organization. This work has been performed to the quality requirements of NQA-1-1989 Part I, Basic and Supplementary Requirements, and NQA-2a-1990, Part 2.7. These quality requirements are implemented through PNWD’s *Waste Treatment Plant Support Project (WTPSP) Quality Assurance Requirements and Description Manual*. The analytical requirements are implemented through WTPSP’s Statement of Work (WTPSP-SOW-005) with the Radiochemical Processing Laboratory (RPL) Analytical Service Operations (ASO).

Experiments that are not method-specific were performed in accordance with PNWD’s procedures QA-RPP-WTP-1101 “Scientific Investigations” and QA-RPP-WTP-1201 “Calibration Control System,” verifying that sufficient data were taken with properly calibrated measuring and test equipment (M&TE) to obtain quality results.

As specified in Test Specification, 24590-WTP-TSP-RT-03-006 Rev 0, BNI’s QAPjP, PL-24590-QA00001, is not applicable because the work will not be performed in support of environmental/regulatory testing, and the data will not be used as such.

PNWD addresses internal verification and validation activities by conducting an independent technical review of the final data report in accordance with PNWD’s procedure QA-RPP-WTP-604. This

review verifies that the reported results are traceable, that inferences and conclusions are soundly based, and that the reported work satisfies the Test Plan objectives. This review procedure is part of PNWD’s *WTPSP Quality Assurance Requirements and Description Manual*.

R&T Test Conditions

Table S.4 discusses the R&T test condition provided in Test Exception 24590-WTP-TEF-RT-04-00004.

Table S.4. Discussion of R&T Test Condition

List R&T Test Conditions	Were Test Conditions Followed?
Utilize large diameter tank(s) (336 Slurry and Supernatant Tanks) for testing.	Yes, a large diameter tank described in Section 5.0 was used for the testing described in this report.
Test with bounding WTP fluid rheology (~30 Pa yield stress and ~30 cP consistency); other rheology property values may also be tested)	Yes, a WTP bounding non-Newtonian simulant described in Section 5.2 was used for the testing described in this report.
Single- and multi-tube sparger system arrays will be tested as appropriate with the outlet of the tubes located approximately 6 inches from the tank bottom immediately under each tube (in addition, single-tube work will be done with the tube located approximately 24 inches from the tank bottom).	Yes, a sparger tube schematic consistent with these test conditions was employed and is described in Section 5.1 of this report.

Simulant Use

A kaolin/bentonite clay simulant was used in this test to duplicate the properties of the non-Newtonian fluids that will be processed in the Hanford Waste Treatment Plant. A thorough discussion of the kaolin/bentonite simulant used can be found in WTP-RPT-111 Rev 0. A pretreated AZ-101 simulant was used in the surface tension measurements.

Discrepancies and Follow-on Tests

No discrepancies were identified nor remain unresolved.

Acronyms

ACFM	actual cubic feet per minute
ASO	Analytical Service Operations
BB	Brilliant Blue FCF
BNI	Bechtel National Inc.
CBT	cone bottom tank
DAS	data acquisition system
DOE	U.S. Department of Energy
EW	east-west
GEMS	graphical exposure modeling system
GUI	graphical user interface
ISE	ion-specific electrode
ISO	International Standards Organization
LRB	laboratory record book
M&TE	Measuring and Test Equipment
NIST	National Institute for Standards and Technology
PC	personal computer
PIT	passive integrated transponder
PJM	pulse jet mixer
PNNL	Pacific Northwest National Laboratory
PNWD	Battelle—Pacific Northwest Division
PVC	polyvinyl chloride

QA	Quality Assurance
QAPjP	Quality Assurance Project Plan
RF	radio frequency
ROB	region of bubbles
RPL	Radiochemical Processing Laboratory
RPP	River Protection Project
R&T	Research and Technology
SCFM	standard cubic feet per minute
SNT	supernatant tank
SOW	statement of work
TSI	thermocouple selector indicator
TSP	total suspended particulates
UFP	Ultrafiltration Process
USB	universal serial bus
UT	ultrasonic testing
UVP	ultrasonic velocity probe
VAC	volts alternating current
VDC	volts direct current
WTP	Waste Treatment Plant
WTPSP	Waste Treatment Plant Support Project
ZOI	zone of influence

Contents

Summary	iii
Acronyms	vii
1.0 Introduction.....	1.1
2.0 Quality Requirements	2.1
3.0 Background.....	3.1
4.0 Small Scale Sparger Testing in Transparent Simulant (T-34 Tests).....	4.1
4.1 Description of Apparatus, Including Simulants and Rheology	4.2
4.1.1 Setup.....	4.2
4.1.2 Operation.....	4.3
4.1.3 Carbopol® Simulant Rheology	4.4
4.2 Results and Discussion	4.4
4.2.1 Region of Bubbles-ROB	4.5
4.2.2 Bubble Formation.....	4.5
4.2.3 Flow Patterns and Recirculation Time	4.7
5.0 Large Scale Sparging Test Stand	5.1
5.1 Description of the Apparatus	5.1
5.2 Description of the Simulant	5.6
5.3 Calculation of Nozzle Air Flow Rates	5.7
6.0 ROB and ZOI Surface Measurements Using Video Imaging.....	6.1
6.1 Materials and Methods	6.1
6.1.1 Apparatus	6.1
6.1.2 Simulant	6.1
6.1.3 Methods Used.....	6.1
6.2 Results and Discussion	6.3
6.2.1 Steady-State Measurements	6.3
6.2.2 Transient Measurements	6.4
7.0 ZOI Subsurface Measurements Using an Ultrasonic Velocity Probe	7.1
7.1 Materials and Methods	7.1
7.1.1 Apparatus	7.1

7.1.2	Simulant	7.1
7.1.3	Methods Used.....	7.1
7.2	Results and Discussion	7.5
7.2.1	Subsurface ZOI Boundary Profiles	7.5
7.2.2	Subsurface Transient ZOI Behavior.....	7.7
7.2.3	ZOI Velocity Profiles	7.9
7.2.4	Depth of the ZOI Boundary Below the Sparger Nozzle.....	7.10
8.0	ZOI Subsurface Measurements Using Passive Integrated Transponders Tags.....	8.1
8.1	Materials and Methods	8.1
8.1.1	Apparatus	8.1
8.1.2	Simulant	8.1
8.1.3	Methods Used.....	8.1
8.2	Results and Discussion	8.5
9.0	ROB Subsurface Measurements Using An Ultrasonic Probe.....	9.1
9.1	Materials and Methods	9.1
9.1.1	Apparatus	9.1
9.1.2	Simulant	9.1
9.1.3	Methods Used.....	9.1
9.2	Results and Discussion	9.6
9.2.1	Data Sets.....	9.7
9.2.2	Measurements at Nominal 30 ACFM	9.10
9.2.3	30 ACFM Data Synopsis.....	9.13
9.2.4	Measurements at Nominal 12 ACFM	9.14
9.2.5	Measurements at Nominal 5 ACFM	9.16
9.3	Summary of Ultrasonic Subsurface Observations	9.17
10.0	ROB and ZOI Circulation Time	10.1
10.1	Materials and Methods	10.1
10.1.1	Apparatus	10.1
10.1.2	Simulant	10.1
10.1.3	Methods Used.....	10.1
10.2	Results and Discussion	10.2
11.0	Aerosol Generation	11.1
11.1	Materials and Methods	11.1
11.1.1	Apparatus	11.1
11.1.2	Simulant	11.1

11.1.3 Methods Used.....	11.2
11.2 Results and Discussion	11.3
11.2.1 Experimental Accuracy	11.6
12.0 Gas Retention and Release Behavior.....	12.1
12.1 Materials and Methods	12.1
12.1.1 Apparatus	12.1
12.1.2 Simulant	12.2
12.1.3 Methods Used.....	12.2
12.2 Results and Discussion	12.4
13.0 Results of Acoustic Pressure Measurements During PJM Overblows in the Large Scale 4-PJM Test Setup	13.1
13.1 Materials and Methods	13.1
13.1.1 Apparatus	13.1
13.1.2 Simulant	13.1
13.1.3 Method Used	13.1
13.1.4 Measurement Locations	13.3
13.1.5 Acoustic Pressure Generation	13.3
13.1.6 Recorded Data	13.3
13.1.7 Data Processing.....	13.3
13.2 Results and Discussion	13.5
14.0 Discussion and Conclusions	14.1
15.0 References.....	15.1
Appendix A: Surface Tension and Yield Stress Measurements on Kaolin/Bentonite Clay Simulant and Simulated Pre-Treated AZ-101 High-Level Waste Slurries	A.1

Figures

1.1. Illustration of Hybrid PJM/Sparger Mixing Concept	1.2
3.1. Illustration of Sparger Fluid Mechanics Concepts in Non-Newtonian Fluids.....	3.2
4.1. T-34 Tank Setup for Sparging in Carbopol®—Side View.....	4.2
4.2. T-34 Tank Setup for Sparging in Carbopol®-Top View.....	4.3
4.3. Distance Above Nozzle Versus ROB Radius in Carbopol® for Submerged Sparger Depths of 54 Inches and 78 Inches and Selected Airflow Rates.....	4.6
4.4. Bubble Formation for Increasing Air-Flow Rates from 0.5 To 2.5 ACFM (left to right)	4.6
4.5. Bubble Reach Versus Sparger Discharge Air-Flow Rate for Sparger Submergence of 78 Inches.....	4.7
4.6. Bubble Velocity in Carbopol® at Various Air-Flow Rates for Sparger Submergence of 78 Inches.....	4.7
4.7. Flow Pattern of Tracer in Carbopol® for ½-in. Sparger Submerged 69 Inches; Flow Path Depicted as Liquid Depth Versus Radial Distance from Sparger.....	4.8
4.8. Recirculation Time of Tracer in Carbopol® for ½-in. Sparger Submerged 69 Inches; “Time Path” Plotted as Liquid Depth Versus Elapsed Time	4.9
4.9. Flow Pattern of Tracer in Carbopol® for ¾-in. Sparger Submerged 69 Inches; Flow Path Depicted as Liquid Depth Versus Radial Distance from Sparger.....	4.9
4.10. Recirculation Time of Tracer in Carbopol® for ¾-in. Sparger Submerged 69 Inches; “Time Path” Plotted as Liquid Depth Versus Elapsed Time	4.10
4.11. Flow Pattern of Tracer in Carbopol® for ¼-in. Sparger Submerged 69 Inches; Flow Path Depicted as Liquid Depth Versus Radial Distance from Sparger.....	4.11
4.12. Recirculation Time of Tracer in Carbopol® for ¼-in. Sparger Submerged 69 Inches; “Time Path” Plotted as Liquid Depth Versus Elapsed Time	4.11
4.13. The Tracer Recirculation Time Versus the Inverse Square of the Sparger Air-Flow Rate for Sparger Tube Diameters of ¼-in., ¾ in. and ½ in. that Are Submerged 69 Inches in Carbopol®	4.12
5.1. Overall View of the Cone Bottom Tank (CBT).....	5.1
5.2. View of the CBT Tank Bottom Showing the Simulant Fill and Pump Out Line	5.2

5.3. Schematic of a Sparge Tube Test Setup	5.3
5.4. Photographs of the Air-Flow Control and Measurement Manifold.....	5.3
5.5. View of the Tank Top Configuration Showing the Walkway, Plastic Sheeting, and Several Sparge Tubes	5.4
5.6. Plan View of the Multitube Sparging Test Setup in the CBT.....	5.5
5.7. Plan View of the Multitube Sparging Test Setup in the CBT.....	5.6
6.1. Image Showing Reference Laser Points (upper right quadrant near walkway) and Several Ping Pong Balls on the Liquid Surface	6.2
6.2. ZOI and ROB Diameters at Various Air-Flow Rates	6.3
6.3. Adjacent ZOI and ROB Interaction Options	6.4
6.4. Surface Tracer Position Versus Time after Start of Sparger Air-Flow and After Tracer Repositioning.....	6.5
6.5. Surface Tracer Positions after Start of Sparger Air Flow (40 ACFM nominal) and After Repositioning Surface Tracers 25 Minutes into the Test Run	6.7
7.1. Schematic of the Dimensions Used to Establish the Positions of the Sparge Tube and UVP in the CBT.....	7.2
7.2. UVP and Sparge Tube Setup	7.3
7.3. Subsurface ZOI Boundary Measurement Data for all Test Runs	7.6
7.4. Subsurface ZOI Boundary Measured Data for 40 ACFM Including Polynomial Curve Fit	7.7
7.5. Subsurface “Time to ZOI” Measurement Results Using the UVP (15 ACFM top; 40 ACFM bottom)	7.8
7.6. UVP Probe Calibration Results for Range of Interest	7.9
7.7. ZOI Vertical Velocity Profiles for Various Sparger Nozzle Air-Flow Rates (40 ACFM top; 5 ACFM middle; 5 and 40 ACFM bottom)	7.10
7.8. Results for ZOI Boundary Below the Sparger Nozzle.....	7.11
8.1. Approximate Antenna Ranges of Three Custom Antennas Used to Identify PIT Tags	8.2
8.2. An Automated System for Moving PIT Tag Antennas Inside of Antenna Wells.....	8.3
8.3. PIT Tag Data at 5 ACFM Nominal Air Flow and 117-in. Nozzle Submergence.....	8.6

8.4. PIT Tag Data at 5 ACFM Nominal Air Flow and 66.5-in. Nozzle Submergence	8.6
8.5. PIT Tag Data at 12 ACFM Nominal Air Flow and 66-in. (Upper) and 118-in. (Lower) Nozzle Submergence	8.7
8.6. PIT Tag Data at 30 ACFM Nominal Air Flow and 66.5-in. Nozzle Submergence	8.8
8.7. PIT Tag Data at 30 ACFM Nominal Air Flow and 117-in. Nozzle Submergence	8.8
8.8. ZOI Boundary Summary from PIT Tag Data Various Air-Flow Rates and Nozzle Submergence Depths	8.9
9.1. Ultrasonic Sensor	9.3
9.2. Sensor Control System Architecture	9.4
9.3. Toneburst Signal Appearing on the Computer Monitor	9.5
9.4. Sample Data Set	9.7
9.5. Sensor Locations Evaluated 2004-03-01 at Nominal 12 ACFM	9.8
9.6. Sensor Locations Evaluated 2004-03-02 at Nominal 12 ACFM	9.8
9.7. Sensor Locations Evaluated 2004-03-02 at Nominal 30 ACFM	9.9
9.8. Sensor Locations Evaluated 2004-03-03 at Nominal 30 ACFM	9.9
9.9. Sensor Locations Evaluated 2004-03-03 at Nominal 5 ACFM	9.10
9.10. Plot of 30 ACFM Locations with Amplitude <0.2 V Max for Two Sequential Days of Testing	9.11
9.11. Plot of 30 ACFM Locations with Amplitude <0.01 V Max for Two Sequential Days of Testing	9.12
9.12. Plot of Bubble Duration at 30 ACFM for Locations with Amplitude <0.01 V max for Two Sequential Days of Testing	9.13
9.13. Plot of 12 ACFM Locations with Amplitude <0.01 V Max	9.15
9.14. Plot of Bubble Duration at 12 ACFM for Locations with Amplitude <0.01 V Max	9.16
9.15. Plot of 5 ACFM Locations with Amplitude <0.01 V max Equal to those Observed at <0.2 V Max	9.18
9.16. Plot of Sparging Bubble Radius as a Function of Elevation for the Three Sparger Flow Rates of 5, 12, and 30 ACFM	9.19
10.1. Schematic of Significant Locations for Sparging Tracer Test	10.2

10.2. Tracer Testing Concepts	10.3
10.3. Circulation Time Test Results for ISE A at 15 ACFM.....	10.4
10.4. Circulation Time Test Results for ISE B at 15 ACFM.....	10.5
10.5. Circulation Time Test Results for ISE A at 40 ACFM.....	10.5
10.6. Circulation Time Test Results for ISE B at 40 ACFM.....	10.6
11.1. Distribution of Aerosol Mass Concentrations ($\pm 20\%$) at each Sample Height for each Size Fraction During the $\frac{1}{3}$ Full Flow Test.....	11.3
11.2. Distribution of Aerosol Mass Concentrations ($\pm 20\%$) at Each Sample Height for each Size Fraction During the Full Flow Test	11.5
11.3. Distribution of Aerosol Mass Concentrations ($\pm 20\%$) at each Sample Height for each Size Fraction During the $\frac{7}{5}$ Times Full Flow Test.....	11.5
11.4. Distribution of Total Suspended Particulate Mass Concentrations ($\pm 20\%$) at Sampling Location 1 (14 inches above liquid surface) for each of the Three Tests	11.6
12.1. Simulant Surface Before Sparger Operation on July 8, 2004	12.5
12.2. Simulant Surface During Sparger Operation with 171 ACFM Air Flow on July 8, 2004.....	12.6
12.3. Simulant Surface Before Sparger Operation on June 11, 2004	12.7
12.4. Simulant Surface During Sparger Operation on June 11, 2004 with 68 ACFM Air Flow	12.8
12.5. Relative Ultrasonic Level Probe Readings While Sparging at Full Air Flow	12.9
12.6. Relative Ultrasonic Level Probe Readings While Sparging at $\frac{1}{3}$ the Full Air Flows	12.10
12.7. Estimated Gas Release for Test Conducted on July 8, 2004.....	12.13
12.8. Estimated Gas Release While Sparging at Full Air Flow	12.15
12.9. Estimated Gas Release While Sparging at Full Air Flow for the First 30 Minutes	12.16
12.10. Estimated Gas Release While Sparging at $\frac{1}{3}$ of the Full Air Flow	12.17
13.1. Hydrophone Locations and Designation in the Supernatant Tank.....	13.2
13.2. Pressure Versus Time for PJM Overblow with 500 kPa (5-bar) Drive Pressure.....	13.5
13.3. Pressure Versus Time for PJM Overblow with 500 kPa (5-bar) Drive Pressure.....	13.6
13.4. Pressure Versus Time for PJM Overblow with 500 kPa (5-bar) Drive Pressure.....	13.6

13.5. Pressure Versus Time for PJM Overblow with 500 kPa (5-bar) Drive Pressure.....	13.7
13.6. Pressure Versus Time for PJM Overblow with 500 kPa (5-bar) Drive Pressure.....	13.7
14.1. ZOI Boundary Below Sparger Nozzle as a Function of Air-Flow Rate	14.2
14.2. Summary Diagram of Non-Newtonian Sparger Boundaries and Flow Patterns.....	14.2

Appendix A Figures

A.1. Schematic of Wilhelmy Plate Method	A.2
A.2. Correlation Between Bingham Yield Stress and Kaolin/Bentonite Clay Slurry Concentration at Ambient Temperature	A.4
A.3. Correlation Between Bingham Yield Stress and Simulated HLW Slurry Concentration at Ambient Temperature	A.5
A.4. Surface Tension of Kaolin/Bentonite Clay Simulant Slurry as a Function of Percent Solids	A.8
A.5. Surface Tension of Diluted Kaolin/Bentonite Clay Slurry for Representative Samples	A.8
A.6. Surface Tension of Simulated HLW Slurry as a Function of Percent Solids	A.10
A.7. Surface Tension of Diluted Simulated HLW Slurry for Representative Samples	A.11

Tables

S.1. Test Objective Evaluation.....	iii
S.2. Test Exceptions.....	iii
S.3. Discussion of Test Success Criterion.....	iv
S.4. Discussion of R&T Test Condition.....	vi
4.1. Typical Rheological Model Fit for Carbopol® Simulant at Ambient Temperature.....	4.5
5.1. Rheological Model Fit for Typical Sample of Kaolin/Bentonite Simulant at Ambient Temperature.....	5.7
6.1. Estimated Radius of Steady-State ZOI Boundary at Liquid Surface Versus Sparger Air-Flow Rate.....	6.7
9.1. Data File Naming Convention.....	9.6
9.2. X-Coordinate Conversion.....	9.6
9.3. Submerged ROB Measurement Positions.....	9.8
10.1. Minimum Circulation Time Calculations at 15 ACFM/40 ACFM.....	10.7
10.2. Average Circulation Time Calculations at 15 ACFM/40 ACFM.....	10.7
11.1. Summary of Results for Aerosol Testing in the Headspace of a Tank Under Sparging Conditions.....	11.4
12.1. Multitube Sparger Test Conditions.....	12.9
12.2. Summary of Multitube Sparging Test Results with Kaolin-Bentonite Simulant to Investigate Gas Release.....	12.18
13.1. Data File Names and Corresponding Hydrophone Locations and Associated Prescon Settings.....	13.4

Appendix A Tables

A.1. Measured Values of Surface Tension (mN/m) for Kaolin/Bentonite Clay Simulant Slurry.....	A.7
A.2. Measured Values of Surface Tension (mN/m) for Simulated HLW Slurry.....	A.10
A.3. Effect of Dissolved Solids Content on Surface Tension.....	A.12

1.0 Introduction

Pulse jet mixer (PJM) technology has been selected for implementation in the Hanford Waste Treatment Plant (WTP). This system has been selected for use in so called “black cell” regions of the WTP. Within these regions of the plant, maintenance capability will not be available for the operating life of the WTP. PJM technology was selected for use in these regions because of the lack of moving mechanical parts that will require maintenance. The concept behind PJM technology involves a pulse tube coupled with a jet nozzle. The tube is immersed in the tank while vacuum, vent, and pressurized air are sequentially supplied to the opposite end of the pulse tube periodically. Application of the vacuum, vent, and pressurized air functions create various operating modes for the pulse tube. These operating modes include the drive cycle (pressure) where the contents of the PJM tube are discharged at high velocity through the nozzle, the refill mode (vacuum) where the tank contents refill the pulse tube, and an equilibration mode (vent) where the pulse tube and tank fill levels approach the same level. These operating modes produce an operating cycle where the PJM system is operated in drive, vent, and vacuum modes. The PJM system uses this sequence of operating modes to produce a sequence of drive cycles that form a turbulent mixing region at the bottom of the tank. The volume of this mixing region as a function of jet velocity and rheological properties is significant in evaluating the performance of the mixing system.

However, PJM technology with non-Newtonian fluids that will be processed through these tanks is not mature. Consequently, an effort has been undertaken to investigate PJM performance in scaled versions of PJM vessels with non-Newtonian fluids that behave similarly to the actual waste. These efforts have shown that PJM mixing systems produce an active mixing cavern at the bottom of the mixing vessels. In these systems, the upper portion of the vessel was unaffected by the PJM mixing system. Consequently, this portion of the vessel is quiescent, and gas produced by radiolysis can accumulate in the stagnant, non-Newtonian gel to form hydrogen-containing bubbles. Mixing in this portion of the vessel is needed to release this gas as it is generated. Unfortunately, expanding the volume of the mixing cavern to encompass entire working volume of the vessel resulted in designs that were complex and economically infeasible. Therefore, additional technology to augment PJM mixing systems and mix the upper portion of the vessel was investigated. The additional technology selected was air sparging. The combination of PJM and air sparging results in a hybrid mixing system where the PJM technology turbulently mixes the bottom portion of the vessel, and air sparging transfers material between the top portion of the vessel and the turbulent PJM mixing region. In this manner, the entire contents of the vessel should be exposed to turbulent mixing. An illustration of this mixing concept is shown in Figure 1.1. The objective of this report is to investigate the behavior and mechanics of the fluid motion caused by the sparger system.

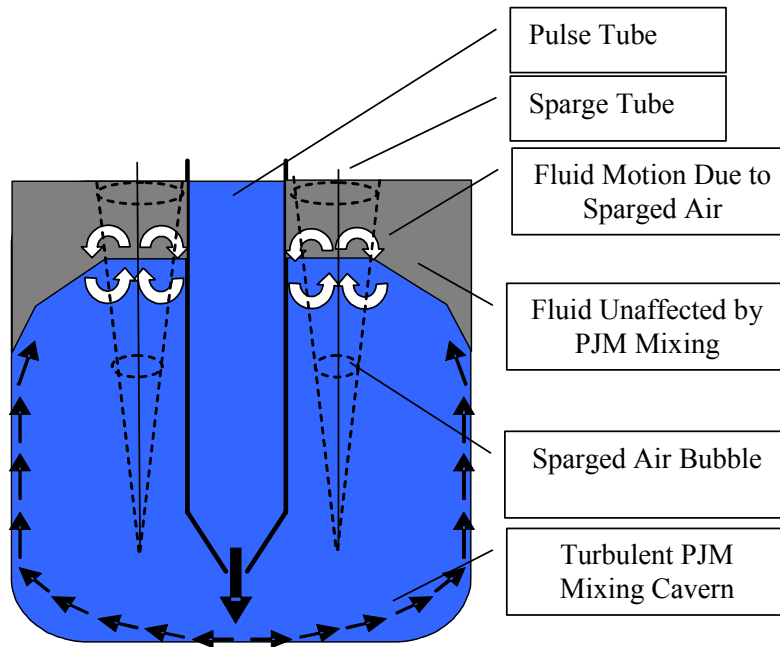


Figure 1.1. Illustration of Hybrid PJM/Sparger Mixing Concept

The testing and design approach for the hybrid PJM/sparger system involves several related efforts. The full-scale PJM mixing performance is projected on the basis of scaled prototype testing results. The technical basis for this approach is addressed in WTP-RPT-113.^(a) This document describes the theoretical basis for the scale-up and verifies the approach by presenting experimental results obtained at three different scales. The sparging system configurations are based on nearly full-scale tests with single and multi-sparger tube test stands. The scaling approach involves a distribution of sparger tubes such that the cross section of the vessel is covered by the zone of influence (ZOI) of the sparger tubes and is based on the information reported in this document. To investigate the performance of the hybrid PJM sparger system, testing has been completed in a scaled prototype (WTP-RPT-128^(b)). Testing was performed in a half-scale lag storage vessel containing PJMs and spargers placed according to the scaling rules developed with the results reported in this document (WTP-RPT-132^(c)).

The information presented in this report consists of only a portion of the hybrid design strategy, test results of sparged air systems in non-Newtonian simulants. Understanding the fluid mechanics of a non-Newtonian air sparger system will allow the hybrid PJM/sparger vessels to be properly designed with the goal that the entire tank contents are circulated and are exposed to the turbulent PJM mixing cavern. This design goal may be achieved by selecting a sparger tube layout and operating flow rates such that the upper portion of the PJM vessel is in motion, and no quiescent regions exist. This document addresses

-
- (a) J.A. Bamberger et al. *Technical Basis for Testing Scaled Pulse Jet Mixing Systems for Non-newtonian Slurries*. WTP-RPT-113, Battelle—Pacific Northwest Division, Richland, WA.
- (b) M.D. Johnson et al. 2004. *Hybrid Mixing System Test Results for Prototype Ultrafiltration Feed Process and high-Level Waste Lag Storage Vessels*. WTP-RPT-128, Battelle—Pacific Northwest Division, Richland, WA.
- (c) J.R. Bontha et al. *Performance Data for a Hybrid PJM/Sparger Mixing System in a Half-Scale Lag Storage Vessel with Non-newtonian Slurries*. WTP-RPT-132, Battelle—Pacific Northwest Division, Richland, WA.

the following fluid mechanics questions for non-Newtonian air sparger systems such that this design goal may be met:

- What flow patterns exist in the regions influenced by air sparger systems in non-Newtonian fluids?
- What is the size and shape of these regions as a function of air flow on the surface and in the subsurface?
- What are the resulting fluid velocities in these regions?
- What is the circulation time of a parcel of fluid in these systems?
- What amount of time is needed to fully establish these flow patterns?
- Can gas generated by radiolysis be fully released by these systems?
- What degree of aerosol is generated by the air sparging system?

To address these questions, two non-Newtonian simulants were investigated, a transparent simulant and an opaque simulant. The first portion of this report discusses work involving the transparent simulant at small scale, which was primarily used for flow visualization purposes to answer the first question posed above. The second portion of the report discusses work involving the opaque simulant at large scale. The opaque simulant possesses rheological properties similar to the wastes expected to be processed in the WTP. The combination of large scale testing with full scale rheological properties allows for the primary design questions to be addressed through this testing. Consequently, the results of the opaque simulant testing provide the primary technical basis for scaling the WTP air sparge system..

2.0 Quality Requirements

Battelle—Pacific Northwest Division (PNWD) implements the River Protection Project (RPP)-WTP quality requirements by performing work in accordance with the PNWD Waste Treatment Plant Support Project quality assurance project plan (QAPjP) approved by the RPP-WTP Quality Assurance (QA) organization. This work has been performed to the quality requirements of NQA-1-1989 Part I, Basic and Supplementary Requirements, and NQA-2a-1990, Part 2.7. These quality requirements are implemented through PNWD's *Waste Treatment Plant Support Project (WTPSP) Quality Assurance Requirements and Description Manual*. The analytical requirements are implemented through WTPSP's Statement of Work (WTPSP-SOW-005) with the Radiochemical Processing Laboratory (RPL) Analytical Service Operations (ASO).

Experiments that are not method-specific were performed in accordance with PNWD's procedures QA-RPP-WTP-1101 "Scientific Investigations" and QA-RPP-WTP-1201 "Calibration Control System," verifying that sufficient data were taken with properly calibrated measuring and test equipment (M&TE) to obtain quality results.

As specified in Test Specification, 24590-WTP-TSP-RT-03-006 Rev 0, BNI's QAPjP, PL-24590-QA00001, is not applicable because the work will not be performed in support of environmental/regulatory testing, and the data will not be used as such.

PNWD addresses internal verification and validation activities by conducting an independent technical review of the final data report in accordance with PNWD's procedure QA-RPP-WTP-604. This review verifies that the reported results are traceable, that inferences and conclusions are soundly based, and that the reported work satisfies the Test Plan objectives. This review procedure is part of PNWD's *WTPSP Quality Assurance Requirements and Description Manual*.

3.0 Background

The mechanics of air sparger systems have been primarily investigated for aqueous-based Newtonian fluids. A limited amount of studies have been performed with air sparging with non-Newtonian fluids. Tilton et al. (1982) describes the fluid mechanics of air sparging systems in non-Newtonian fluids as having two primary flow regions. In the first region, fluid flows with the bubbles as they rise. In this work, we refer to this region as the “region of bubbles” (ROB). Outside of the ROB, the fluid flow is reversed and is opposite the direction of the bubble rise. This region is referred to as the “zone of influence” (ZOI). Further outside, the ZOI is a region of fluid that is unaffected by the air sparger system. Note that this fluid flow pattern is driven entirely by buoyant forces due to the density difference between sparged air and the test fluid.

Tilton describes the fluid flow regime in the ROB region as typically being turbulent while the ZOI region is laminar flow. The fluid outside of the ZOI region is quiescent. Each of these regions is separated by boundary layers that transition between the various regions and flow regimes. These concepts are illustrated in Figure 3.1.

In this document, we refer to the air flow in units of actual cubic feet per minute (ACFM) or standard cubic feet per minute SCFM. The ACFM designation indicates the air flow at the hydrostatic pressure at the bottom of the sparge tube at the temperature measured in the sparge tube hose. The SCFM designation indicates the air flow at atmospheric conditions and 70°F. In this manner, ACFM is the air flow at the sparger nozzle while SCFM is approximately the air flow in the headspace above the sparged vessel.

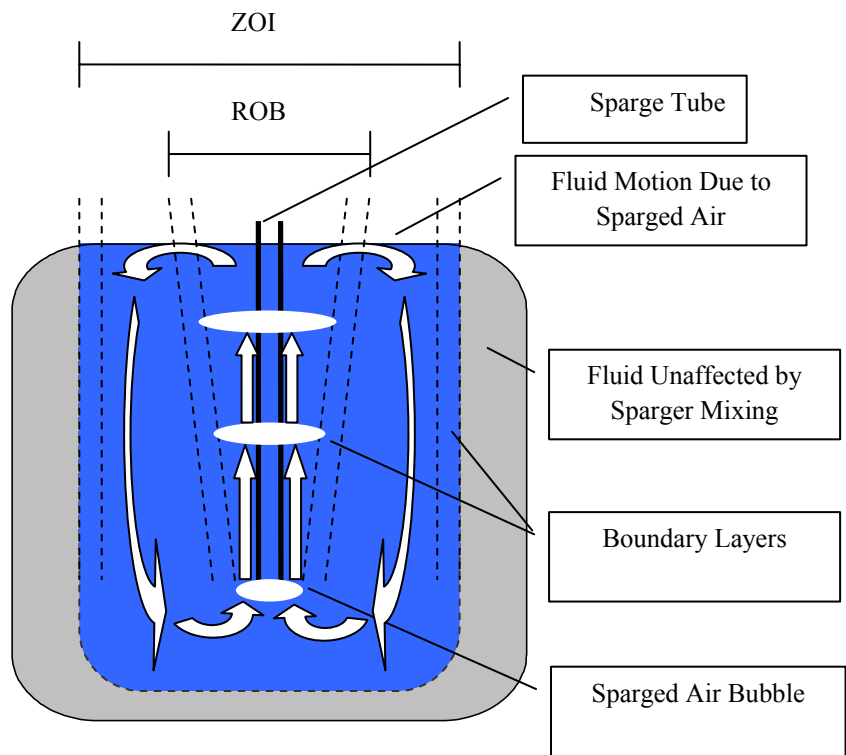


Figure 3.1. Illustration of Sparger Fluid Mechanics Concepts in Non-Newtonian Fluids

4.0 Small Scale Sparger Testing in Transparent Simulant (T-34 Tests)

The purpose of the small scale (34-in.-diameter transparent tank) T-34 experiments with transparent non-Newtonian fluids was to support and justify the approach proposed for the large scale (152-in. tank) sparging tests with opaque non-Newtonian fluid. To accomplish this purpose, the following test objectives were set:

1. Confirm the large-scale test approach of using visual surface measurements of the ROB as a function of tank elevation for varying sparger depths to map the profile of the ZOI and ROB.
2. Visually observe and measure the ROB at the sparger outlet with particular attention to the region below the sparger discharge to determine the minimum tank elevation for sparger placement to be used in the cone bottom tank (large scale test)
3. Evaluate the flow pattern and recirculation time as a function of sparger air-flow rate. Identify any submerged recirculation patterns that do not interact with the tank surface.
4. Determine whether any significant observations exist as the sparger air flow rate is increased that indicate that tank wall effects are influencing the recirculation.

These objectives have been met as follows:

1. In the T-34 tank, the ROB forms an approximately inverted cone that is the envelope of the bubble trajectories. The ROB radius at each horizontal cross section is primarily a function of the height (distance above the sparger nozzle). The nozzle's submerged depth (distance below the liquid surface) had no observed effect on the ROB radius as a function of elevation.

The depth to which the air bubbles reach below the sparger nozzle is a linear function of the air-flow rate.

2. The recirculation time through the ZOI was found to vary proportionally with the inverse square of the sparging air-flow rate. All tracer particles were introduced at the liquid surface and descended to various depths. Most of the circulation loops extended the full depth of the sparger tube. All observed circulation loops rose above the mid point of the sparger tube. No complete circulation loop was observed to totally exist below the mid point of the sparger tube (i.e., all observed tracer particles always rose above the sparger mid point before beginning to descend).
3. Visual observations of the ROB were made in both water and Carbopol®, and the bubbles released from the sparge tube in Carbopol were larger than those created in water. A distinct transition in the shape of the ROB near the liquid surface was observed as the air-flow rate increased. The transitions observed in water were more distinct than those seen in Carbopol®. At the lower (initial) sparger air-flow rates tested, the radius of the ROB could be measured on the tank surface, and all bubbles terminated and were released at the liquid surface. As the sparger air-flow rate was increased, a transition was observed in the ROB. The ROB extended toward the tank wall with a marked deviation from the cone profile observed at lower air-flow rates. Submerged bubbles were observed flowing radially towards the wall before reaching the surface. Minimal increases in the sparger air-flow rate, beyond that resulting in the ROB extending to the wall, caused the bubbles to become entrained in the downward flow and re-circulate back into the rising core of bubbles. Because of the larger bubbles that existed in the Carbopol®, the re-circulation of bubbles from the tank wall back to the ROB was not as distinct as that observed in water. As the bubbles in Carbopol® reached the tank wall and began to flow laterally inward, the majority of the bubbles tended to recirculate back into the

radially outward surface flow before reaching the rising core of bubbles. Based on the observations made in both water and Carbopol®, it was assumed that the shape of the ROB could be monitored to evaluate whether the tank wall was having a significant impact on the ZOI. No further discussion exists regarding the visual observations made in water.

4.1 Description of Apparatus, Including Simulants and Rheology

4.1.1 Setup

A 34-in.-I.D transparent tank was used to perform single sparger tests in Carbopol® using nozzle diameters of $\frac{1}{4}$, $\frac{3}{8}$, and $\frac{1}{2}$ inches and is referred to as the T-34 Tank. Schematics of the side view and top view of the T-34 configuration are presented in Figure 4.1 and Figure 4.2, respectively. For the smaller diameter tubes, the center sparge tube was inserted through a $\frac{1}{2}$ -in. galvanized pipe to provide structural support and dampen vibrations. Colored strings hung down the length of the tank at 3-inch intervals to provide visual reference marks for making radial measurements.

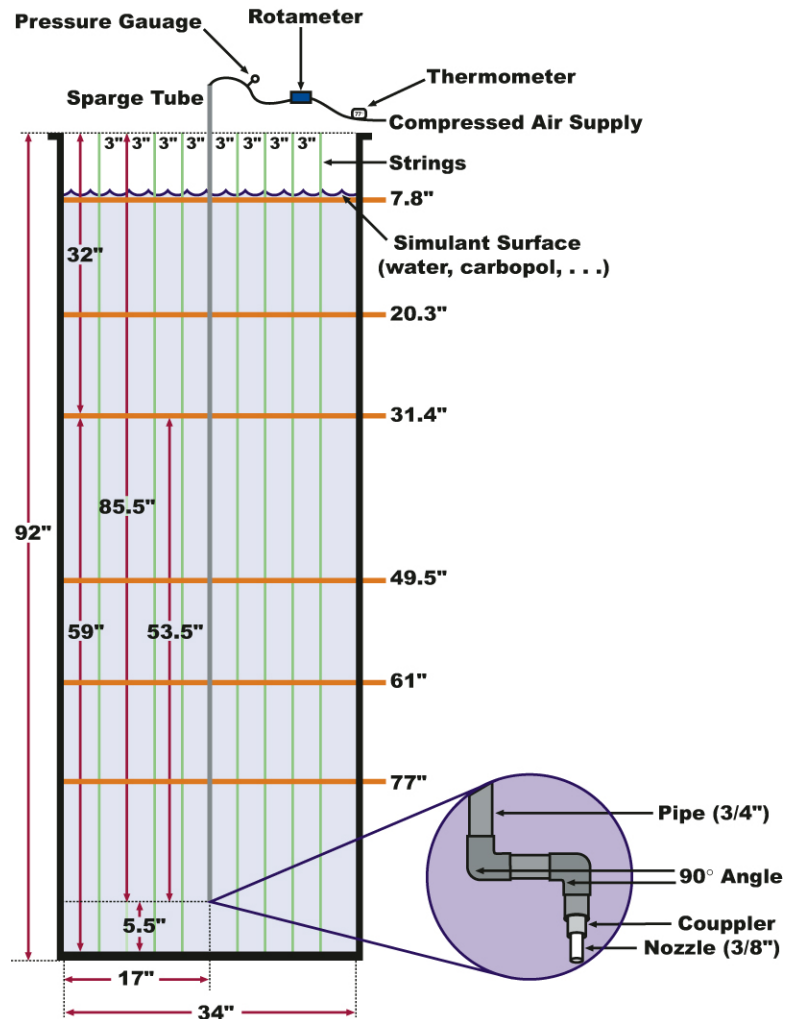


Figure 4.1. T-34 Tank Setup for Sparging in Carbopol®—Side View

The orange bands in Figure 4.1 indicate elevations. A rotameter, a pressure gauge, and a thermometer were used to calculate and adjust the actual airflow at the discharge of the sparge tube. The “S” shape nozzle was chosen to allow easy repositioning of the source of bubbles.

For some of the tests, a second plane of vertical strings was added to the aforementioned setup in a direction orthogonal to the first plane. The two planes intersect in the middle of the tank, passing through the sparger tube. Three camcorders were used to collect simultaneous recordings of the bubble flow; one recorded the activities on the tank surface, and the other two recorded side views.

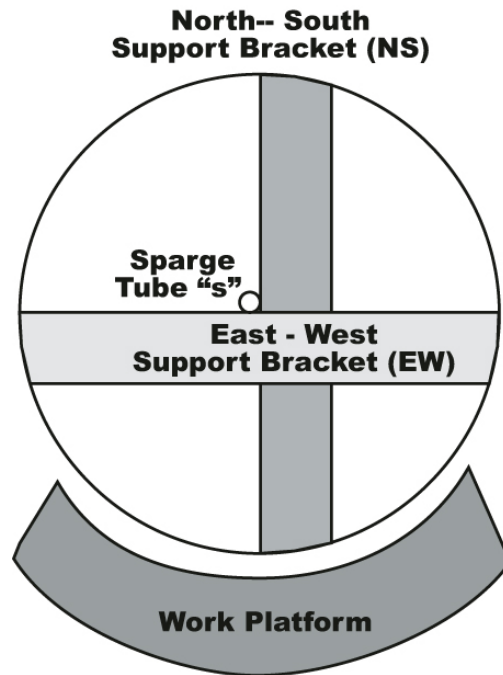


Figure 4.2. T-34 Tank Setup for Sparging in Carbopol®-Top View

4.1.2 Operation

The flow rate was adjusted and monitored using a rotameter that indicated the flow rate at standard pressure and temperature. Measurements of temperature and pressure were used to calculate the actual discharge sparger air-flow rate as described in Section 5.3. To achieve a desired flow rate, several iterations of flow adjustment followed by calculation of the actual air flow rate were performed.

Testing was possible over the range of air-flow rates from 0.3 to 3.0 ACFM. The rising bubbles create a circular pattern at the simulant surface. A tape measure was used to measure the ROB and bubble diameter at the simulant surface.

The suspended vertical strings and horizontal bands on the tank exterior were used to define the radial and vertical position of the ROB, respectively. The visual measurements of the bubble diameter were

made at several submerged elevations from the sparger discharge to the surface. The distance between each pair of strings was used to visually estimate the bubble diameter.

The maximum distance that the bottom of a bubble was observed below the sparger discharge, defined as the bubble reach, was measured using a submerged vertical tape measure. Times for bubble rise were obtained from video recordings of the experiments.

In the flow pattern experiments, two tracers were dropped on the surface of the simulant, and the position of each of the tracers was recorded with time. Each tracer was tracked as it moved down towards the bottom of the tank and then laterally towards the tank center. Next, it entered the ROB and was transported upwards to the surface, completing a recirculation loop or cycle. Tracking continued until at least one complete cycle was recorded. The tracer position was estimated using the submerged vertical strings and horizontal bands, and the corresponding times were obtained using a stop watch. Two types of tracer particles were used, bead and triangle tracers. The bead tracer was spherical, had a diameter of approximately 0.4 in, and a specific gravity of 1.0. The triangle tracer was formed from three 1-in.-long tubular beads that were strung together and bound to form an equilateral triangle. The triangle tracer had a specific gravity of 1.8. Because of its size and density, the motion of the bead tracer deviated less from the fluid flow than the triangle tracer. However, the triangle tracer was easier to visually track within the Carbopol®.

Testing was conducted according to TI-RPP-WTP-381, and test observations were recorded in LRB BNW-14522.

4.1.3 Carbopol® Simulant Rheology

Carbopol® is a cross-linked acrylic acid polymer. Carbopol® solution is a translucent to transparent suspension of hydrated spheres of the polymer. Rheologically, a typical Carbopol® solution is a pseudoplastic gel whose viscosity increases with concentration and depends strongly on pH. Table 4.1 shows the measured simulant rheological data for selected tests during the measurement period. Small variations in rheological properties were measured because of evaporation of water due to sparging.

4.2 Results and Discussion

The sparger discharges bubbles whose size and frequency depend on the sparger tube diameter and air-flow rate. The rising bubbles impart momentum to the fluid, resulting in an upward flow within the ROB. As the bubbles rise, they expand because of the decreasing hydrostatic pressure. The rising fluid entrains additional fluid, which along with the expanding bubbles causes the ROB to expand with increasing elevation.

To sustain the upward flow created within the ROB, a downward flow in an annular area around the ROB is formed; this is the ZOI. The combination of the rising central flow and downward annular flow sets up a recirculating flow pattern in which “one pass” or “cycle” will be defined as downward flow through the ZOI, lateral flow between the ZOI and ROB at the elevation of the sparger discharge, upward flow in the ROB, and lateral flow near the surface between ROB and ZOI.

Table 4.1. Typical Rheological Model Fit for Carbopol® Simulant at Ambient Temperature

Model/Model Parameter	T-34 Carbopol® Simulant
Bingham Plastic:	
τ_O^B —the Bingham yield stress (Pa)	60
η_p —the plastic viscosity (mPa·s)	109
standard error	44.2
Herschel-Bulkley:	
τ_O^H —the yield stress (Pa)	17
k—Herschel-Bulkley consistency coefficient (Pa·s ^{-b})	6.08
b—Herschel-Bulkley power law exponent	0.457
standard error	1.9

4.2.1 Region of Bubbles-ROB

Observations in the transparent fluid indicated the bubbles are not spherical but are uniform for a given flow rate. Bubble size is on the order of but larger than the sparger tube diameter. Because of the experimental setup, the sparging tube experienced lateral motion (less than 3/8 in.) due to bubble discharge. The lateral motion of the sparge tube may have contributed to the bubble shape and radial position at release from the sparge tube. Thus, the measured diameter of the ROB may be slightly larger than that obtained with a perfectly rigid sparge tube. ROB and ZOI are depicted in a schematic diagram in Section 3.0.

The ROB size as a function of sparger air-flow rate is shown in Figure 4.3. The ROB size is a non-linear function of elevation above the sparger nozzle and the air-flow rate. The data taken with a submerged nozzle of 54 inches matches the corresponding data for the submerged nozzle of 78 inches. This observation validates objective one; that is, surface measurements of the ROB can be taken as a function of sparger submergence depth to characterize the ROB profile. In other words, instead of measuring the size of ROB at various depths above a submerged sparger tube, the sparger is submerged in stages, and the size of ROB is measured on the simulant surface.

4.2.2 Bubble Formation

The bubble-formation photographs shown in Figure 4.4 depict bubbles as they form at the sparger nozzle. The bubbles were not spherical. As air was discharged from the nozzle, the growing bubble slipped and rotated in arbitrary directions until it reached the size at which release occurred. As soon as each bubble detaches from the nozzle, the bubble responds to the homogeneity of the environment and becomes nearly symmetrical. Only the bubble being formed at the sparger outlet extended below the sparger. Regardless of the air-flow rate, all detached bubbles rose immediately after releasing from the sparger.

The linear relationship between the bubble reach (maximum distance that the bubble extends below the sparger nozzle) and the sparger air-flow rate for the 3/8-in. nozzle is presented in Figure 4.5.

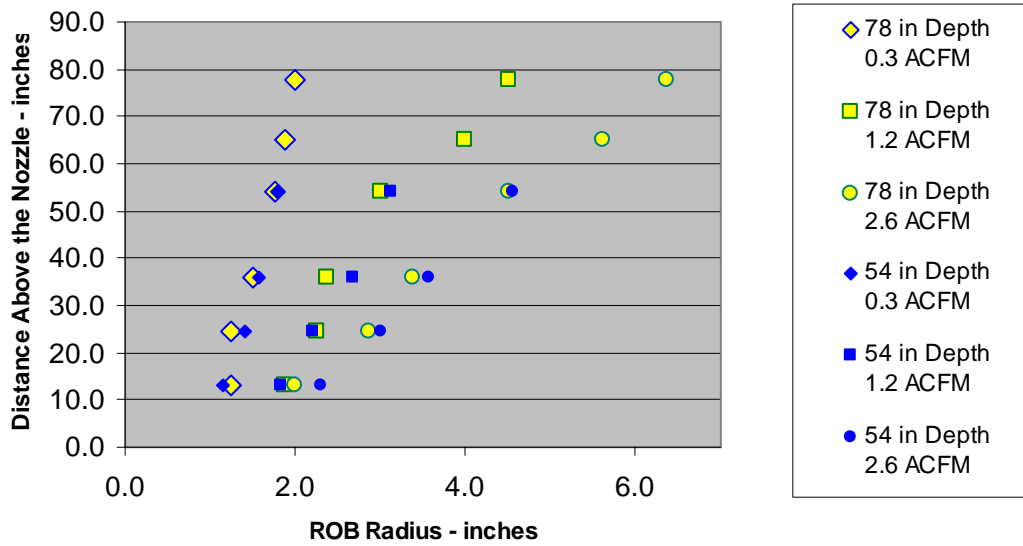


Figure 4.3. Distance Above Nozzle Versus ROB Radius in Carbopol® for Submerged Sparger Depths of 54 Inches and 78 Inches and Selected Airflow Rates

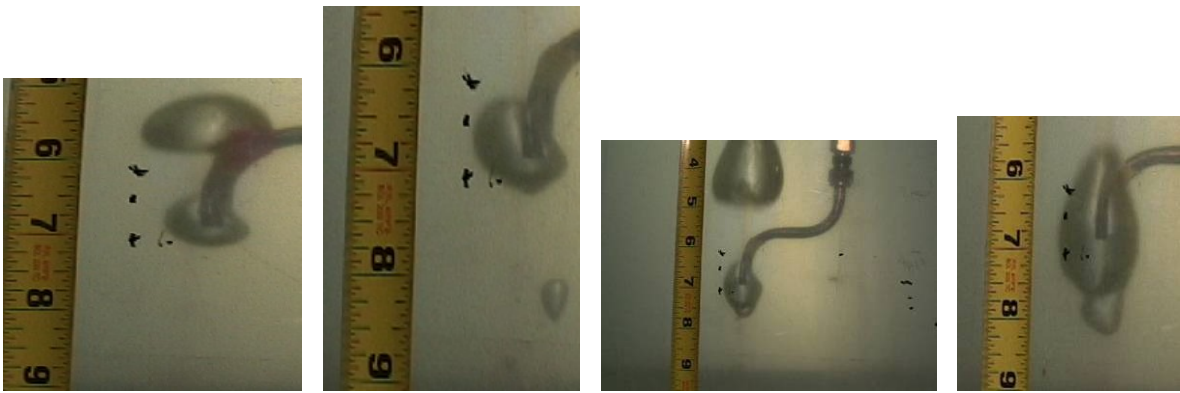


Figure 4.4. Bubble Formation for Increasing Air-Flow Rates from 0.5 To 2.5 ACFM (left to right). An unrelated independent bubble is presented in each view.

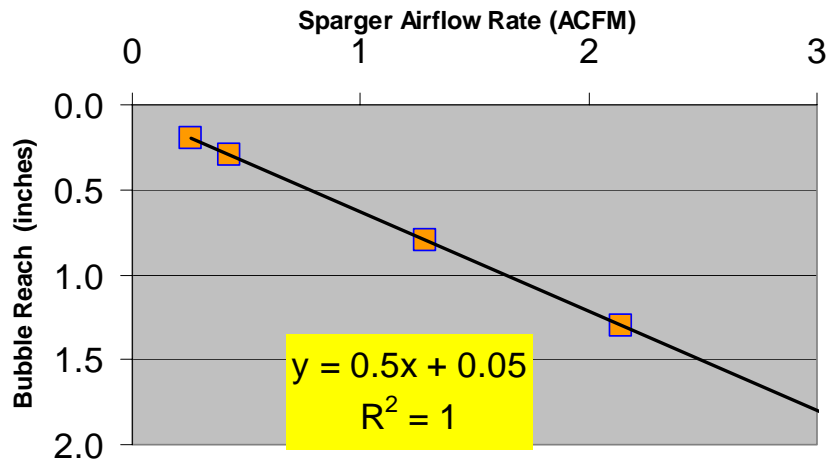


Figure 4.5. Bubble Reach Versus Sparger Discharge Air-Flow Rate for Sparger Submergence of 78 Inches

4.2.3 Flow Patterns and Recirculation Time

The bubble rise velocity was calculated using video recordings of the experiments for air-flow rates from 0.3 to 2.6 ACFM, and the results are presented in Figure 4.6. The bubble velocity ranges between 16 in./s and 28 in./s and is dependent on the sparger air-flow rate. Two distinct rise velocities were measured at each air-flow rate, which can be observed in Figure 4.6. A major contributor to the existence of two distinct velocities was the coalescing of bubbles. The smaller (initial) bubbles rose slower than the larger bubbles, which resulted from coalescence.

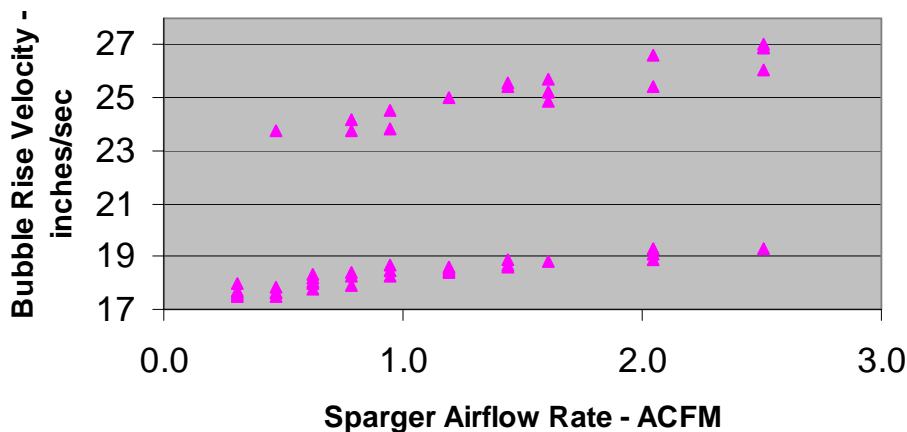


Figure 4.6. Bubble Velocity in Carbopol® at Various Air-Flow Rates for Sparger Submergence of 78 Inches

The flow patterns shown in this section are examples of the recirculation patterns that occurred in the small-scale testing. For a sparger air flow rate of 1.1 ACFM and nozzle diameters of $\frac{1}{4}$ in., $\frac{3}{8}$ in., and $\frac{1}{2}$ in., three pairs of tracer plots are depicted in Figure 4.7 through Figure 4.12. The path of a tracer is detailed in the plots from the moment it is dropped on the surface of the simulant through at least one full

cycle (one pass), that is, until the tracer comes back to the surface. The tracer flow path depicted in two dimensions, elevation and radial position, is presented in the first of each pair of plots. The tracer “time path” is presented in the second figure of each pair, with elevation plotted as a function of time. There is a one-to-one correspondence in elevation between the markers in each pair of plots. Therefore, the relative times between positions in the flow path can be obtained using the corresponding time path.

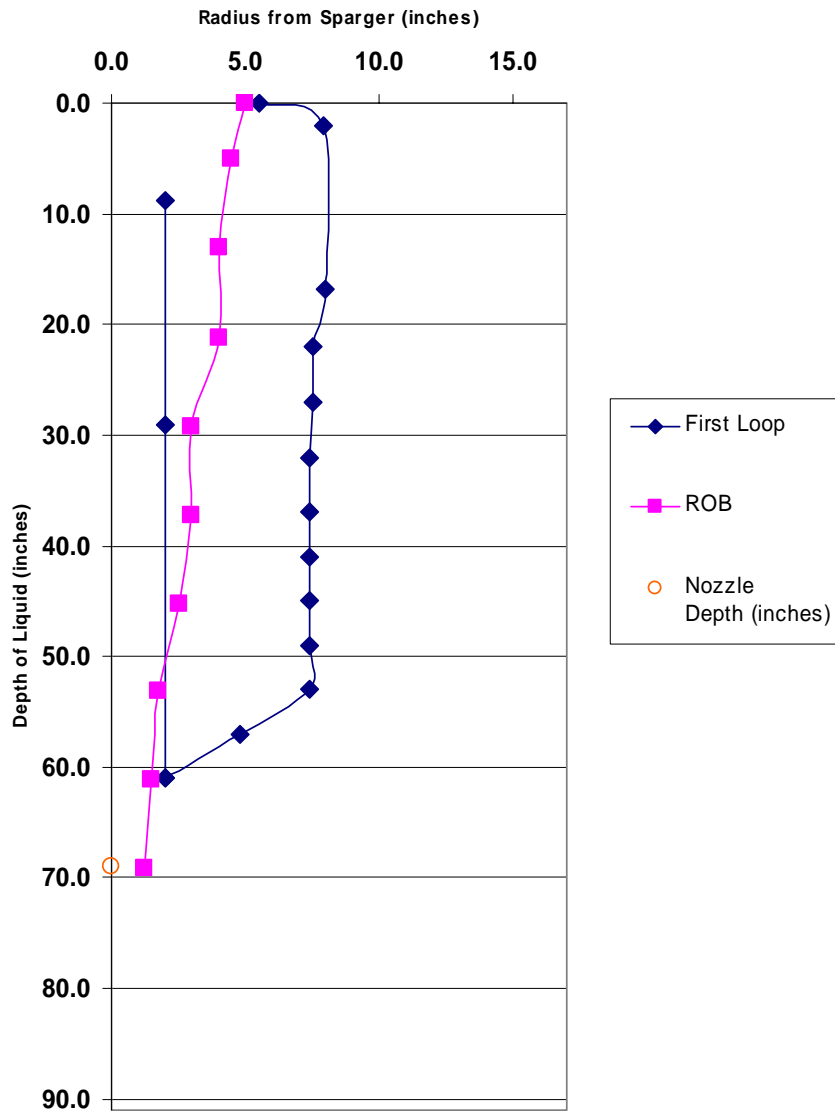


Figure 4.7. Flow Pattern of Tracer in Carbopol® for ½-in. Sparger Submerged 69 Inches; Flow Path Depicted as Liquid Depth Versus Radial Distance from Sparger

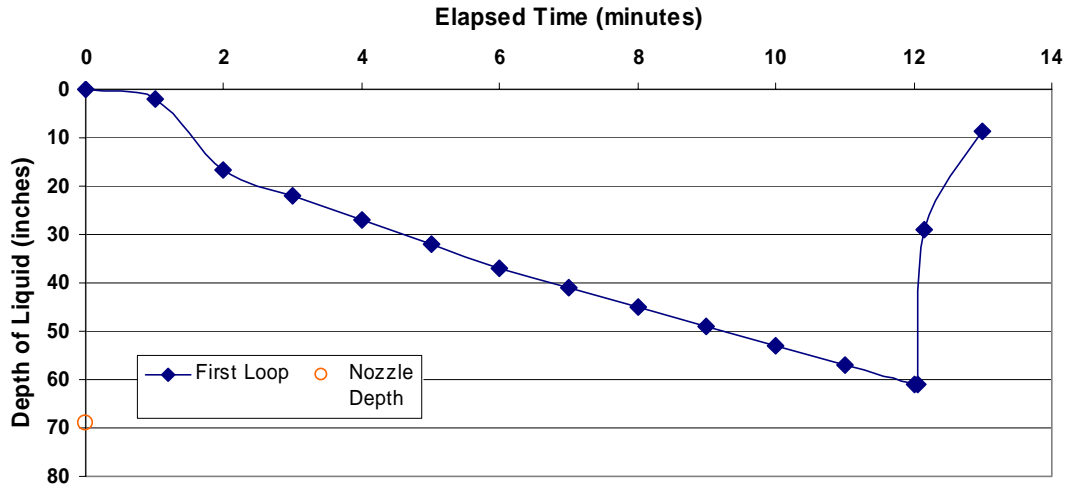


Figure 4.8. Recirculation Time of Tracer in Carbopol® for 1/2-in. Sparger Submerged 69 Inches; “Time Path” Plotted as Liquid Depth Versus Elapsed Time

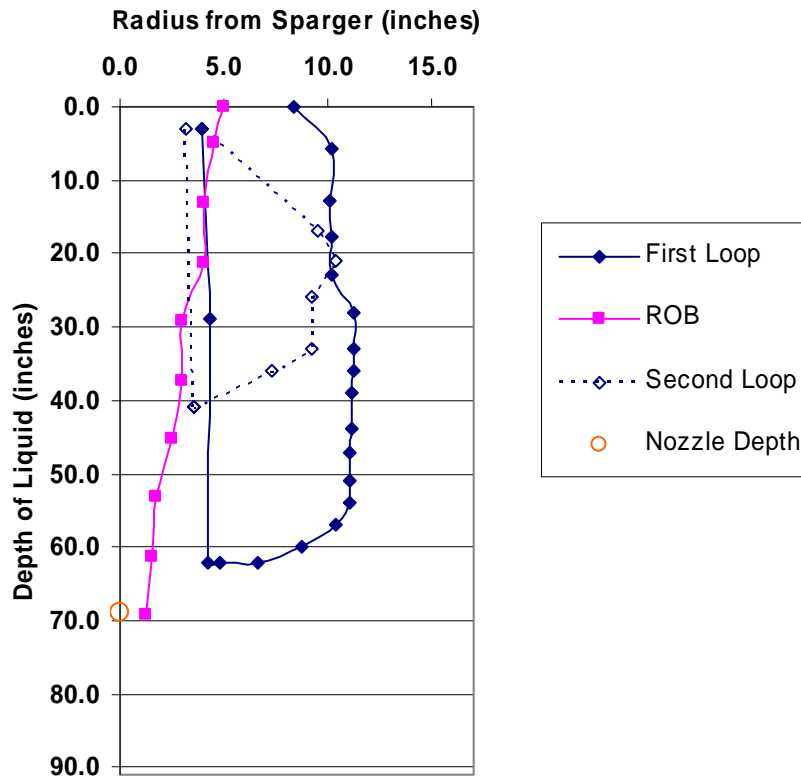


Figure 4.9. Flow Pattern of Tracer in Carbopol® for 3/8-in. Sparger Submerged 69 Inches; Flow Path Depicted as Liquid Depth Versus Radial Distance from Sparger

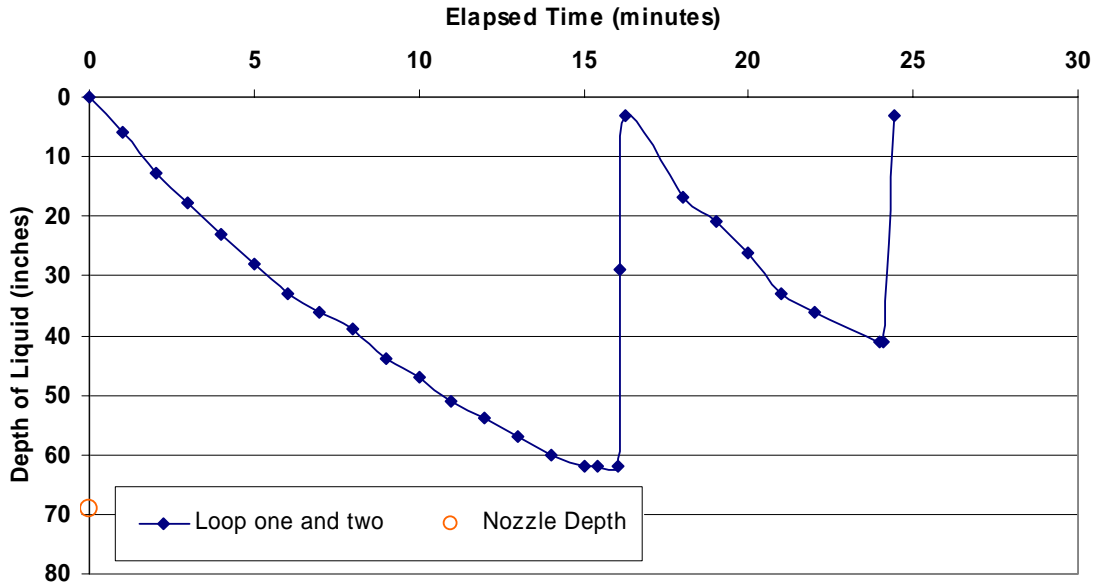


Figure 4.10. Recirculation Time of Tracer in Carbopol® for $\frac{3}{8}$ -in. Sparger Submerged 69 Inches; “Time Path” Plotted as Liquid Depth Versus Elapsed Time

The radius of the ROB is indicated (by square marks) on each flow-path plot. The velocity in the downward annular flow of the ZOI can be estimated from the time-path plots containing elevation as a function of time. At 0.4 ACFM, it took about 110 min for the bead tracer to do one pass; it took about 4 min for the triangle tracer to traverse the first loop for the 2.0 ACFM flow rate. The upward velocity of the tracers in the ROB was similar to that of the bubble velocity, which is shown in Figure 4.6 to be in the range of 16 in./sec to 28 in./sec. Because of the large upward velocity, the tracers often traveled from the bottom of the ZOI to the tank surface without a tracer position being recorded.

Occasionally, the tracer was not transported far from the ROB before exhibiting downward movement. Tracers that started their downward flow at a radius only slightly larger than that of the ROB moved downwards to approximately 30% or more of the submergence depth of the sparger before being entrained by the upward flow for a return trip to the surface. All of the second or subsequent passes (cycles) of the tracers ended at the surface independent of the starting position. No recirculation loops were observed spanning the lower half or the middle section of the sparger tube.

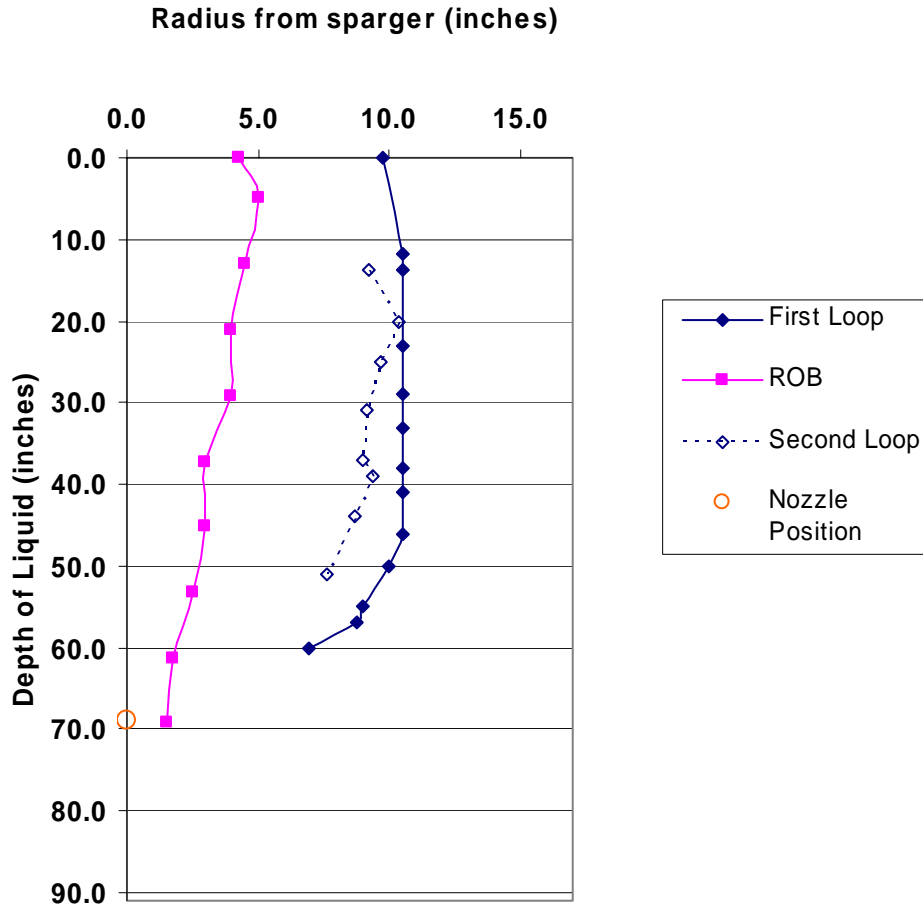


Figure 4.11. Flow Pattern of Tracer in Carbopol® for $\frac{1}{4}$ -in. Sparger Submerged 69 Inches; Flow Path Depicted as Liquid Depth Versus Radial Distance from Sparger

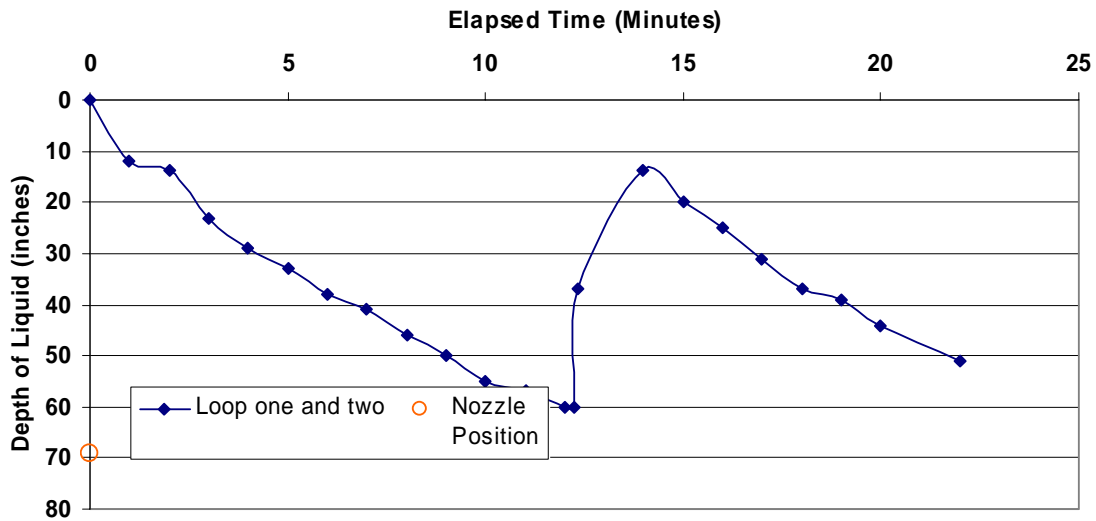


Figure 4.12. Recirculation Time of Tracer in Carbopol® for $\frac{1}{4}$ -in. Sparger Submerged 69 Inches; "Time Path" Plotted as Liquid Depth Versus Elapsed Time

For a sparger submergence depth of 69 in., air-flow rates between 0.4 ACFM and 1.9 ACFM, and sparge tube diameters of ¼ in., 3/8 in., and ½ in., a total of 40 tracer-path measurements were obtained, 20 measurements for each type of tracer (bead and triangle). Tube size had no noticeable effect on the sparging results. The tracer-path measurements were used to examine the relationship between tracer recirculation time and sparger air-flow rate. At flow rates less than 1.9 ACFM, the tank wall may have impacted the test results; however, no distinct observations were made to indicate such. At flow rates higher than 1.9 ACFM, observations of the ROB indicated that the upper region of the ZOI was constrained by the tank wall. This was defined as the limiting flow rate at which data/tests would be conducted in the T-34 tank. Based on the tracer-path measurements, it appears that the recirculation time is inversely proportional to the square of the sparging air-flow rate, which is illustrated in Figure 4.13. It is assumed that the inverse square relationship is caused by hydrodynamic drag dominating the recirculation process. The drag of the bubbles imparted on the fluid and therefore the velocity of the rising fluid within the ROB is proportional to the square of the volumetric flow rate. This upward flow is balanced by the viscous drag created by the downward flow at the unyielding boundary of the ZOI.

The relationship provides guidance for controlling the recirculation rate with the sparger air-flow rate. The relationship also demonstrates that the cross-sectional area of the ZOI is much larger than the ROB. In other words, a small amount of air re-circulates a large amount of liquid.

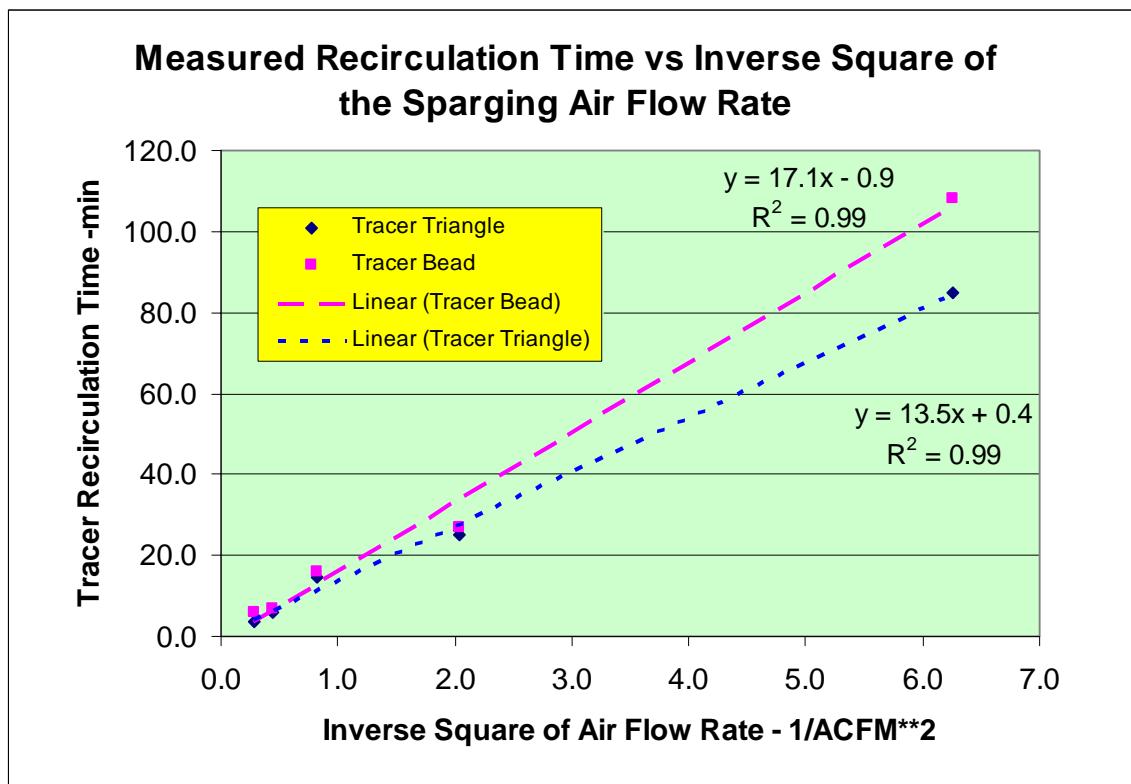


Figure 4.13. The Tracer Recirculation Time Versus the Inverse Square of the Sparger Air-Flow Rate for Sparger Tube Diameters of ¼-in., 3/8 in. and ½ in. that Are Submerged 69 Inches in Carbopol®

5.0 Large Scale Sparging Test Stand

5.1 Description of the Apparatus

The experimental apparatus consisted of a large-scale combined cylindrical and cone-shaped tank with either a single or multi-sparge tube array. The upper cylindrical portion of the tank has an inside diameter of 152 inches and extends 96 inches in height. The cone-shaped section extends a further 70 inches, tapering to a diameter of 12 inches at the tank bottom. The overall tank height is 166 inches. Figure 5.1 and Figure 5.2 are photographs of the tank.



Figure 5.1. Overall View of the Cone Bottom Tank (CBT)



Figure 5.2. View of the CBT Tank Bottom Showing the Simulant Fill and Pump Out Line

Three-quarter-inch Schedule-40 pipe was used for each of the sparge tubes for all tests, both single and multi-tube configurations. Each tube was immersed in the simulant to a known depth, and air was forced through the tube, exiting at the nozzle at the lower end. A dedicated rotameter, pressure gauge, and thermocouple were used to measure volumetric air flow rate, pressure, and temperature for each tube. A schematic of the overall test setup showing one of the sparge tube configurations is shown in Figure 5.3. Figure 5.4 shows the flow control and measurement manifold setup, and Figure 5.5 is a view overlooking the top of the drained tank when configured with multiple sparge tubes. Plastic sheeting was installed to minimize simulant being splashed from the tank. Several sparge tubes are visible.

Note also the walkway extending across the tank. The ultrasonic velocity probe (UVP), used extensively in subsurface measurements, was fixed to a mast (pipe). The mast was clamped to the walkway railing at various positions to facilitate testing.

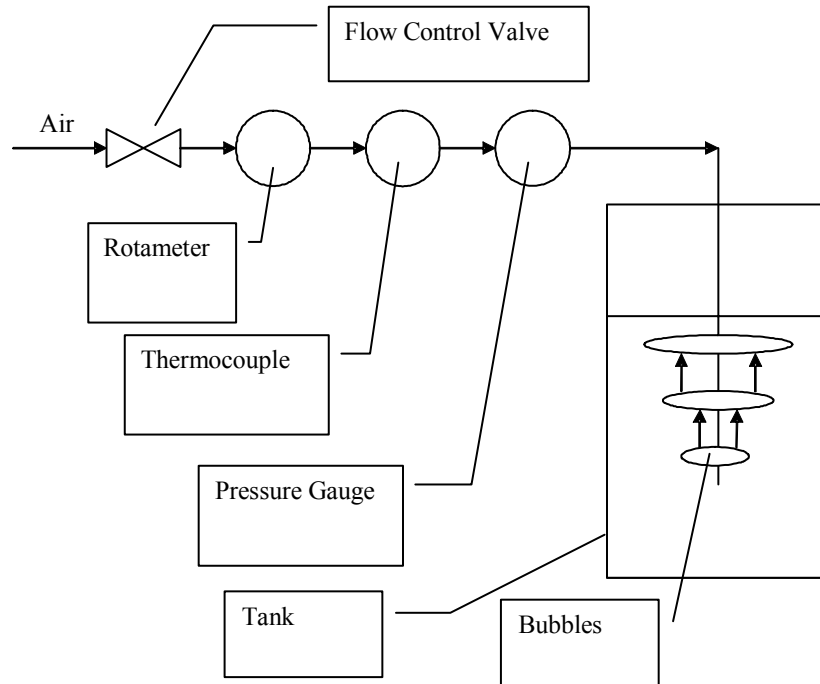


Figure 5.3. Schematic of a Sparge Tube Test Setup

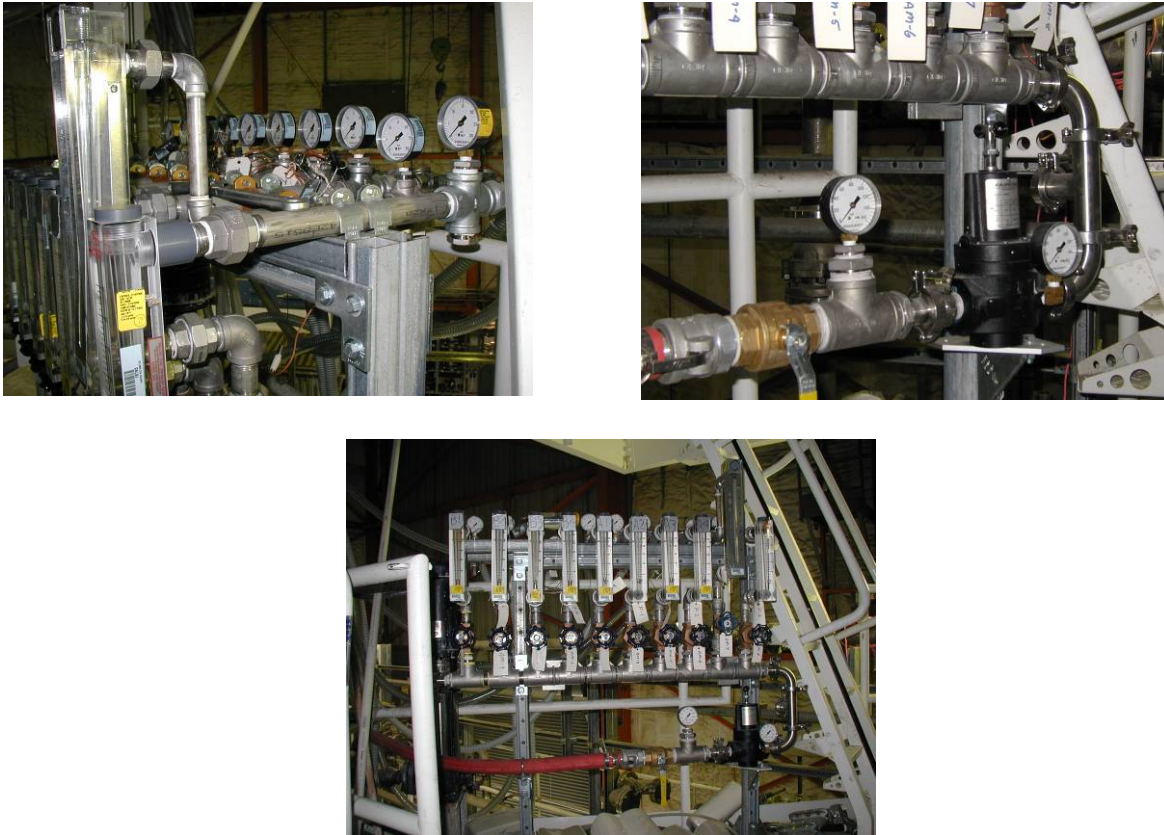


Figure 5.4. Photographs of the Air-Flow Control and Measurement Manifold



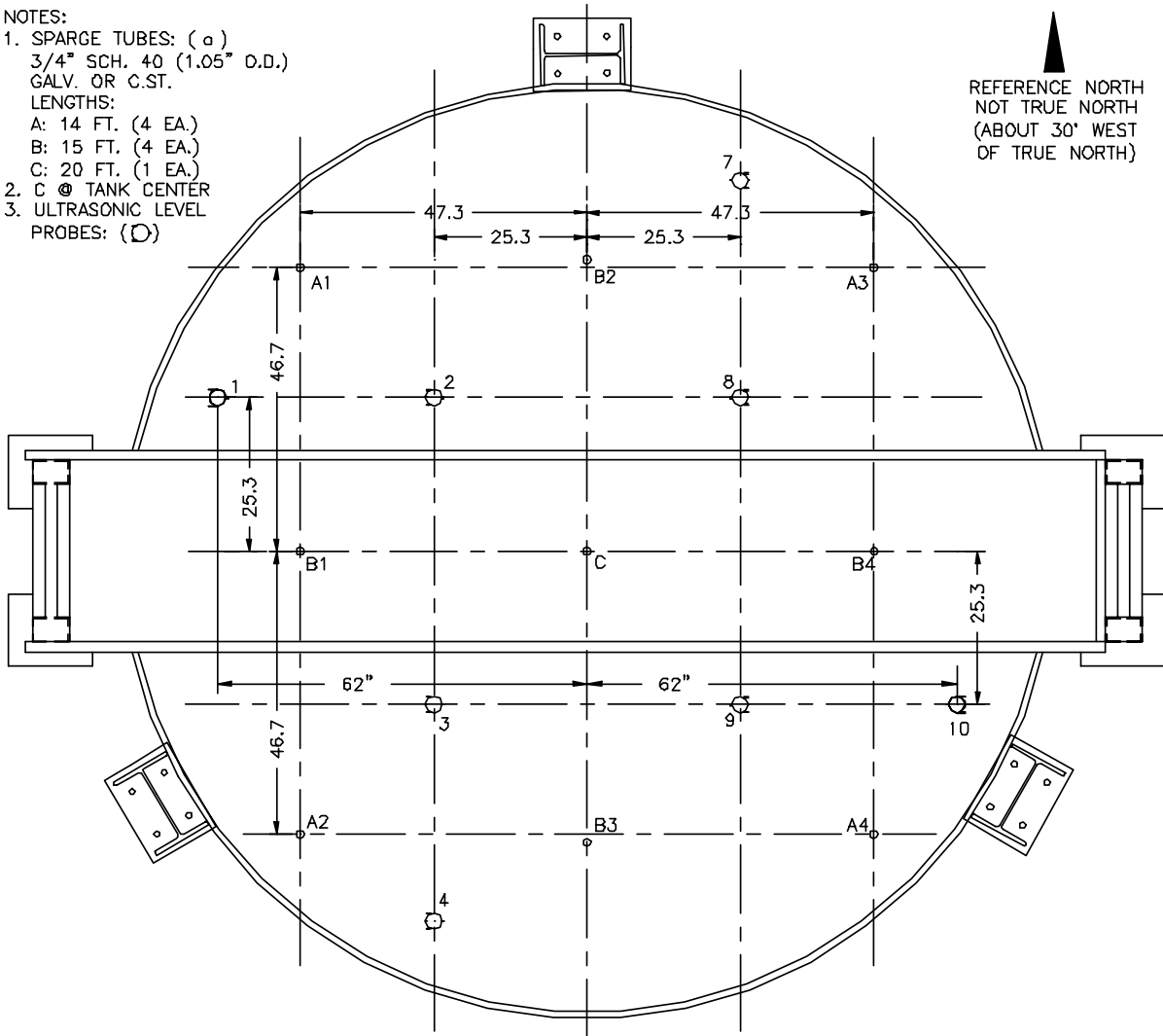
Figure 5.5. View of the Tank Top Configuration Showing the Walkway, Plastic Sheetting, and Several Sparge Tubes

The multi-tube sparging system tank layout is shown in Figure 5.6 and Figure 5.7. All single sparge tube tests were carried out with all sparge tubes removed except for the tube positioned on the vertical center line of the center of the tank shown as sparger “C.” For the single tube sparge tests, the nozzle was positioned 24 inches from the tank bottom, and the typical nozzle depth below the simulant surface was 120 ± 1 in. However, several tests were performed at different nozzle submergence depths. For example, tests were performed to determine the depth of ZOI below the sparge nozzle and were carried out at a nozzle submergence depth of 66 ± 1 in. and the nozzle 78 ± 1 in. above the tank bottom.

NOTES:

1. SPARGE TUBES: (a)
3/4" SCH. 40 (1.05" O.D.)
GALV. OR C.ST.
- LENGTHS:
A: 14 FT. (4 EA.)
B: 15 FT. (4 EA.)
C: 20 FT. (1 EA.)
2. C @ TANK CENTER
3. ULTRASONIC LEVEL PROBES: (D)

▲
REFERENCE NORTH
NOT TRUE NORTH
(ABOUT 30° WEST
OF TRUE NORTH)



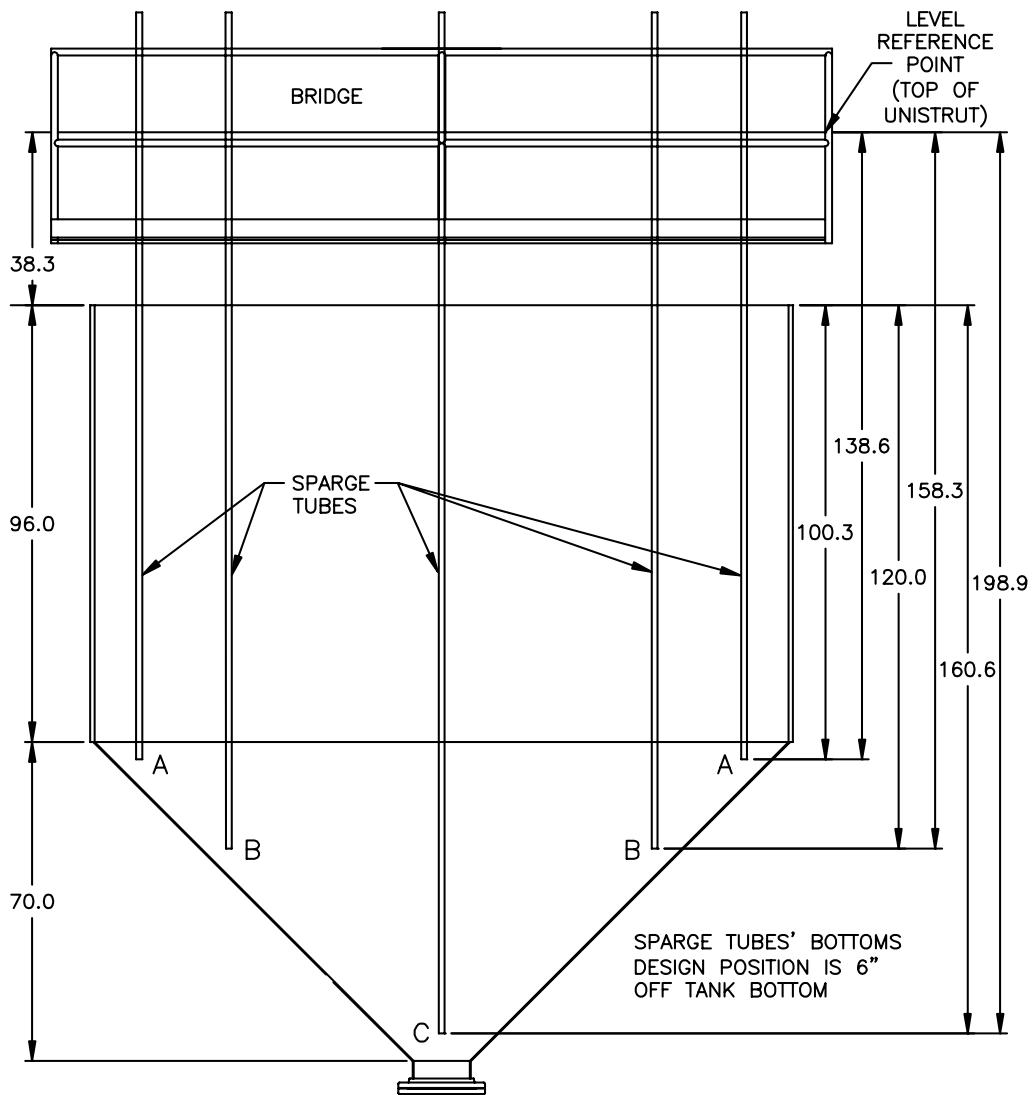
SPARGE TUBES & ULTRASONIC LEVEL PROBE POSITIONS
IN SLURRY TANK, PLAN VIEW

MIKE WHITE

SLURRY TANK 9 SPARGE TUBES & 10 LEV.PROBES.DWG

08/04/04

Figure 5.6. Plan View of the Multitube Sparging Test Setup in the CBT



SPARGE TUBE LOCATIONS IN THE SLURRY (CONE-BOTTOM) TANK, ELEVATION VIEW

Sparge Tube Locs-Elev.dwg Mike White 09/02/04

Figure 5.7. Plan View of the Multitube Sparging Test Setup in the CBT

5.2 Description of the Simulant

The simulant used for these tests consists of a mixture of kaolin clay (EPK Feldspar Pulverized) and bentonite clay (WYO-Ben Big Horn CH-200) in water. To meet the WTP bounding parameters of Bingham plastic consistency of 30 cP and yield stress of 30 Pa, a recipe was developed using these two clays. The recipe calls for a composite of 80% kaolin and 20% bentonite mixed with water to a loading of approximately 27 wt%. Water was then added to the simulant to adjust the rheological parameters to other target values. The bulk density of this degassed clay simulant is approximately 1.2 g/mL. Table 5.1 shows the measured simulant rheological data for a typical sample taken during the measurement period.

Small variations in rheological properties were measured because of evaporation of water due to sparging and peroxide/water additions. With these variations, the Bingham yield stress varied between approximately 30 to 40 Pa while the Bingham consistency varied between 20 to 25 cP. A thorough discussion of the kaolin/bentonite simulant used can be found in WTP-RPT-111 Rev 0 (Poloski et al. 2004).

Table 5.1. Rheological Model Fit for Typical Sample of Kaolin/Bentonite Simulant at Ambient Temperature

Model/model Parameter	336 Simulant After Gas Retention Test
Bingham Plastic:	
τ_O^B - the Bingham yield stress (Pa)	32
η_p - the plastic viscosity (mPa·s)	23
standard error	9.1
Herschel-Bulkley:	
τ_O^H - the yield stress (Pa)	30
k - Herschel-Bulkley consistency coefficient (Pa·s ^{-b})	0.098
b - Herschel-Bulkley power law exponent	0.80
standard error	2.1

5.3 Calculation of Nozzle Air Flow Rates

For all tests, the rotameter, pressure gauge, and thermocouple readings were converted to the actual volumetric air flow in the slurry at the sparger nozzle submergence depth. Isothermal expansion at the sparge tube orifice was assumed. The following equation was used for this calculation:

$$Q_{sparge} = \frac{Q_{rot}}{\rho_{sim} g h_{sparge} + P_0} \left(\frac{P_{std} P_{rot} T_{rot}}{T_{std}} \right)^{\frac{1}{2}} \quad (5.1)$$

where Q_{sparge} = actual volumetric air flow in the slurry at submergence depth of the sparge tube nozzle (ft³/min)

Q_{rot} = calibrated volumetric flow rate read from the rotameter at standard conditions (ft³/min)

P_{std} = absolute pressure at which the rotameter is calibrated (1 atm)

T_{std} = absolute temperature at which the rotameter is calibrated (530 R)

P_{rot} = absolute pressure read at the rotameter (atm)

T_{rot} = absolute temperature read at the rotameter (R)

ρ_{sim} = bulk density of the simulant tested (74.9 lb/ft³)

g = gravitational constant (32.2 ft/s²)

h_{sparge} = submerged depth of the sparger tube nozzle (ft)

P_0 = atmospheric pressure (1 atm).

6.0 ROB and ZOI Surface Measurements Using Video Imaging

This set of tests had two main objectives: 1) determine the steady-state size of the ROB and ZOI regions at the fluid surface at different flow rates and nozzle submergence depths and 2) determine the time required to establish a steady-state velocity profile and provide a plot of the ZOI diameter versus time using surface measurements.

6.1 Materials and Methods

6.1.1 Apparatus

The single tube sparging test stand described in Section 5.1 was used for these tests.

6.1.2 Simulant

The kaolin/bentonite simulant described in Section 5.2 was used in these tests.

6.1.3 Methods Used

The leading edge of the ZOI was measured by placing buoyant flow followers, or “surface tracers”, (ping pong balls or tracer dye) on the surface near the sparge tube. The surface tracers moved radially outward because of the induced secondary flow and stopped at the boundary where radial flow ceases and axial flow downward dominates.

The ZOI and ROB were measured with a laser reference system coupled with video imaging software. This technique involved placing two laser points 6 inches apart on the surface of the simulant. The surface of the simulant was video recorded. The video camera was fitted with a wide angle adapter, mounted on a tripod, and fastened securely overlooking the tank surface. The laser emitters for the reference system were securely fastened to a rigid frame that was in turn fastened securely to the safety railing. The laser emitter frame can be seen in Figure 6.1 slightly above and to the left of the laser points. The reference marks were used by the video analysis software to provide a reference of distance on the recorded video.

The frames from the video images were then analyzed to determine the number of pixels between various features in the frame. By knowing the number of pixels and the actual distance between the laser reference points, the actual distance between two features on the frame was determined. Figure 6.1 shows a video image from the video tape record for a test run at a target air-flow rate of 40 ACFM. Note the position of the laser points on the liquid surface (upper right quadrant appearing near the edge of the walkway) and two ping pong balls (lower left quadrant).

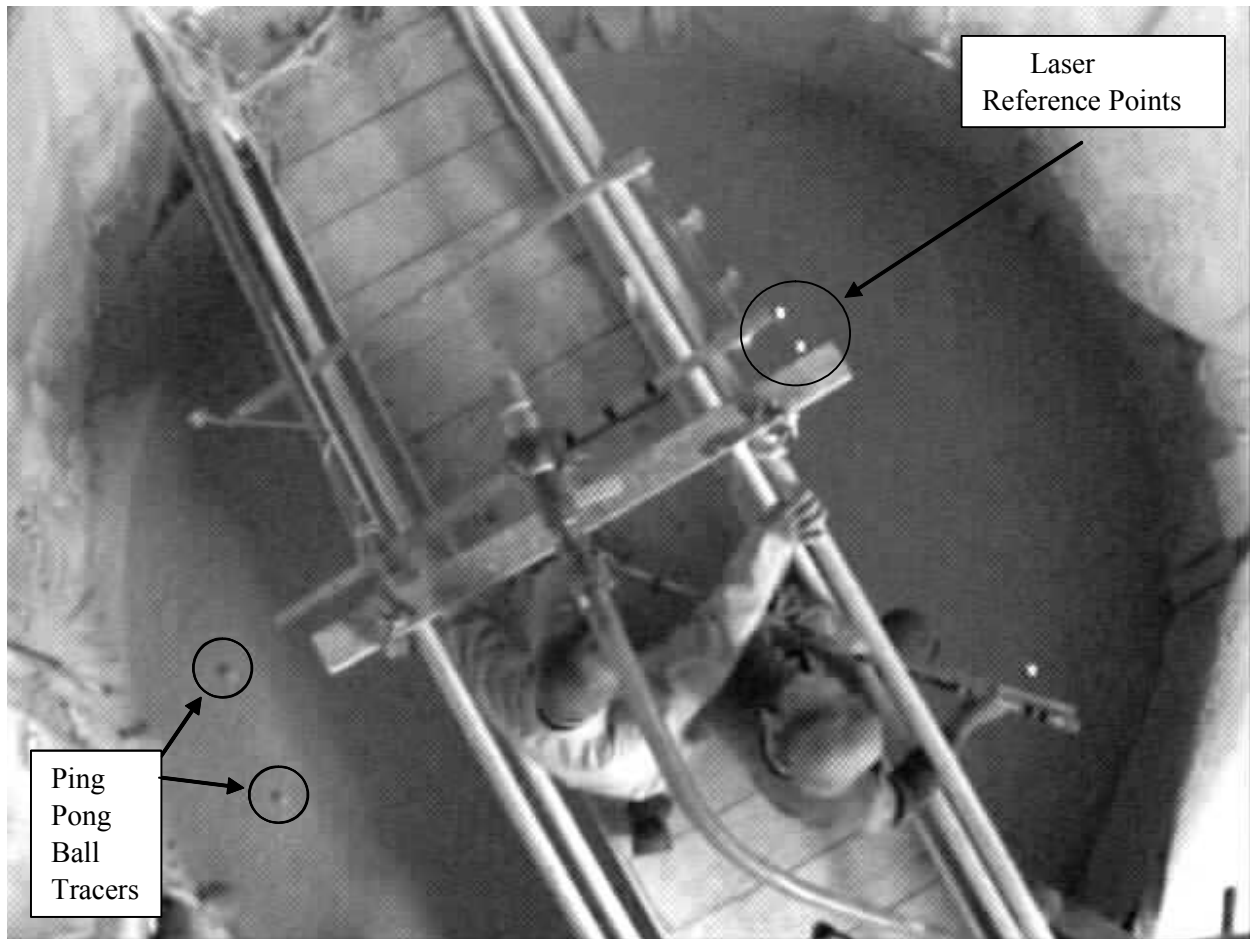


Figure 6.1. Image Showing Reference Laser Points (upper right quadrant near walkway) and Several Ping Pong Balls on the Liquid Surface

Two sets of experiments were performed using the video imaging technique. The first set of experiments measured the ZOI and ROB dimensions at steady state. For these steady-state experiments, air flow was started at a target volumetric flow rate at a known nozzle submergence depth. After the ping pong balls appeared to reach a constant position, the video imaging technique discussed above was used to determine the diameters of several air bubbles as they burst at the surface. The reported values are the average diameter of these measurements. In addition, the ZOI diameter was calculated by averaging the distances of the ping pong balls to the sparge tube.

The second set of experiments measured the positions of the surface tracers as a function of time after air flow started. For these transient experiments, surface tracers were placed near the sparge tube, and the air flow was started at a target volumetric flow rate at a known nozzle submergence depth. The position of each surface tracer was captured on video as a function of time. The ZOI radius was calculated using the video technique discussed above to determine the distance of each ping pong ball with respect to the sparge tube. For several of these tests, the ping pong balls were repositioned near the sparge tube after the steady-state positions had been obtained. These data were acquired to distinguish between transient ZOI formation and steady-state ZOI surface flow velocity.

6.2 Results and Discussion

6.2.1 Steady-State Measurements

The data shown in Figure 6.2 indicate that the ROB and ZOI diameters are a weak function of submergence depth, which suggests that these regions have a nearly cylindrical submerged vertical profile. Because the full-scale sparger systems will be submerged deeper than in these experiments, and because the ZOI and ROB diameters will increase slightly with submergence depth, using these data was concluded to be conservative. Accordingly, a correlation of the ROB and ZOI diameters to only the actual volumetric flow rate at the nozzle adequately describes the size of these regions (see Equations 6.1 and 6.2).

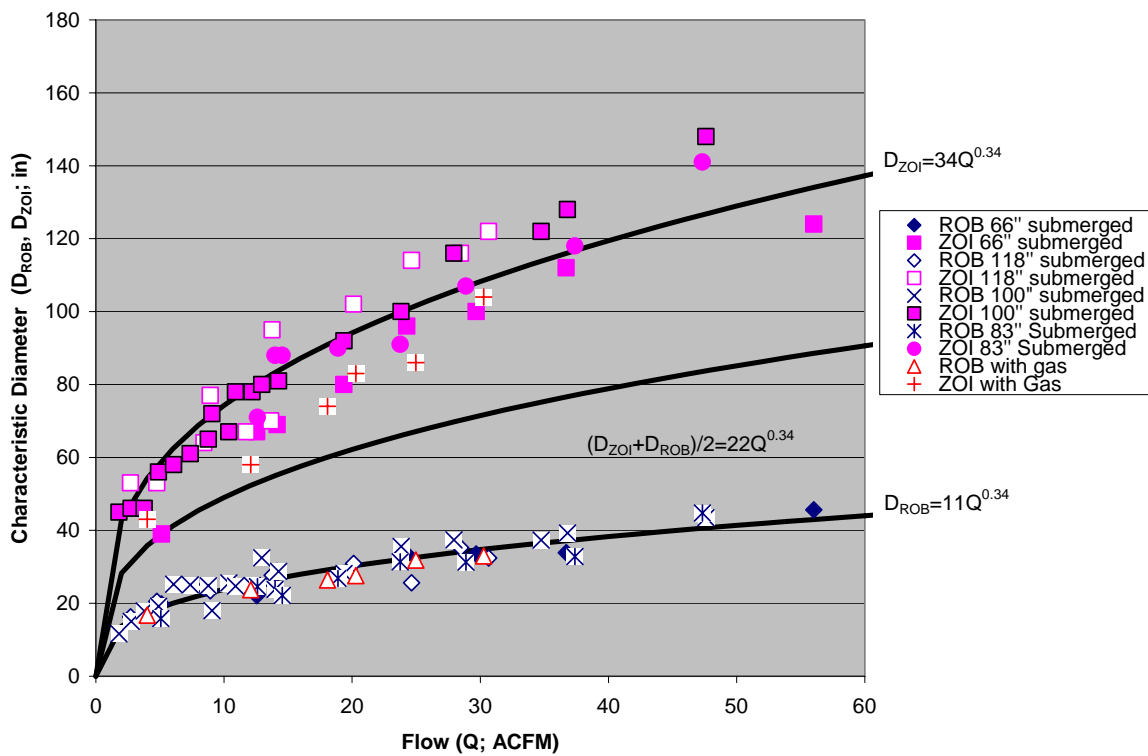


Figure 6.2. ZOI and ROB Diameters at Various Air-Flow Rates

$$D_{ROB} = 11Q_{air}^{0.34} \quad (6.1)$$

$$D_{ZOI} = 34Q_{air}^{0.34} \quad (6.2)$$

where D_{ROB} is the ROB diameter (in.), D_{ZOI} is the ZOI diameter (in.), and Q_{air} is the actual volumetric flow rate of the air in slurry at the end of the sparge tube (ft^3/min).

Combining Equations 6.1 and 6.2 shows that $D_{ZOI} \approx 3 \cdot D_{ROB}$. This suggests that a tank can be well mixed with spargers that are configured such that the ZOI from one sparge tube meets the ROB from an

adjacent sparg tube (see Figure 6.3). In this manner, the sparger spacing shown in Equation 6.3 can be specified. Thus, the $\frac{2}{3}$ ZOI diameter position was defined as one key position to be used for measurements of the time to establish the ZOI as reported herein.

$$\begin{aligned}
 D_s &= \frac{D_{ROB} + D_{ZOI}}{2} \\
 D_{ZOI} &= 3D_{ROB} \\
 D_s &= \frac{2}{3}D_{ZOI}
 \end{aligned}
 \tag{6.3}$$

where D_s is the sparger spacing, D_{ROB} is the ROB diameter, D_{ZOI} is the ZOI diameter.

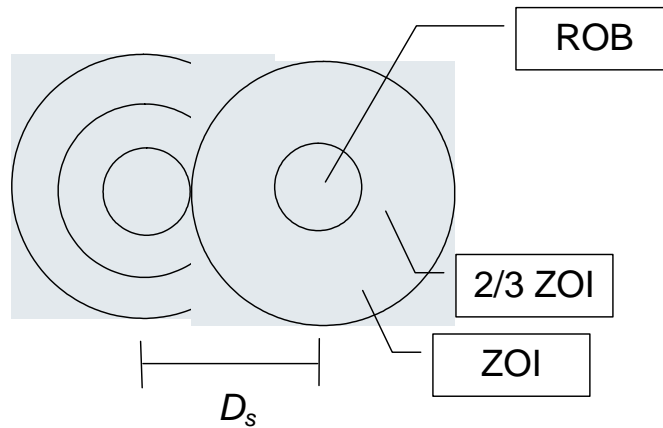


Figure 6.3. Adjacent ZOI and ROB Interaction Options

6.2.2 Transient Measurements

Figure 6.4 shows the measured data for “time to ZOI” for ping pong surface tracers at target air-flow rates of 5, 15, 25, and 40 ACFM. The charts show the measured positions of each selected ping pong ball following the beginning of air sparging. Note that the balls indicated were selected as being the most visible and having continuous visibility throughout the test (as recorded on the video tape). Although the ping pong balls were positioned as close to the sparge tube as possible before the sparger air was turned on, the first bubbles reaching the liquid surface “kicked” the balls immediately well into the ZOI..

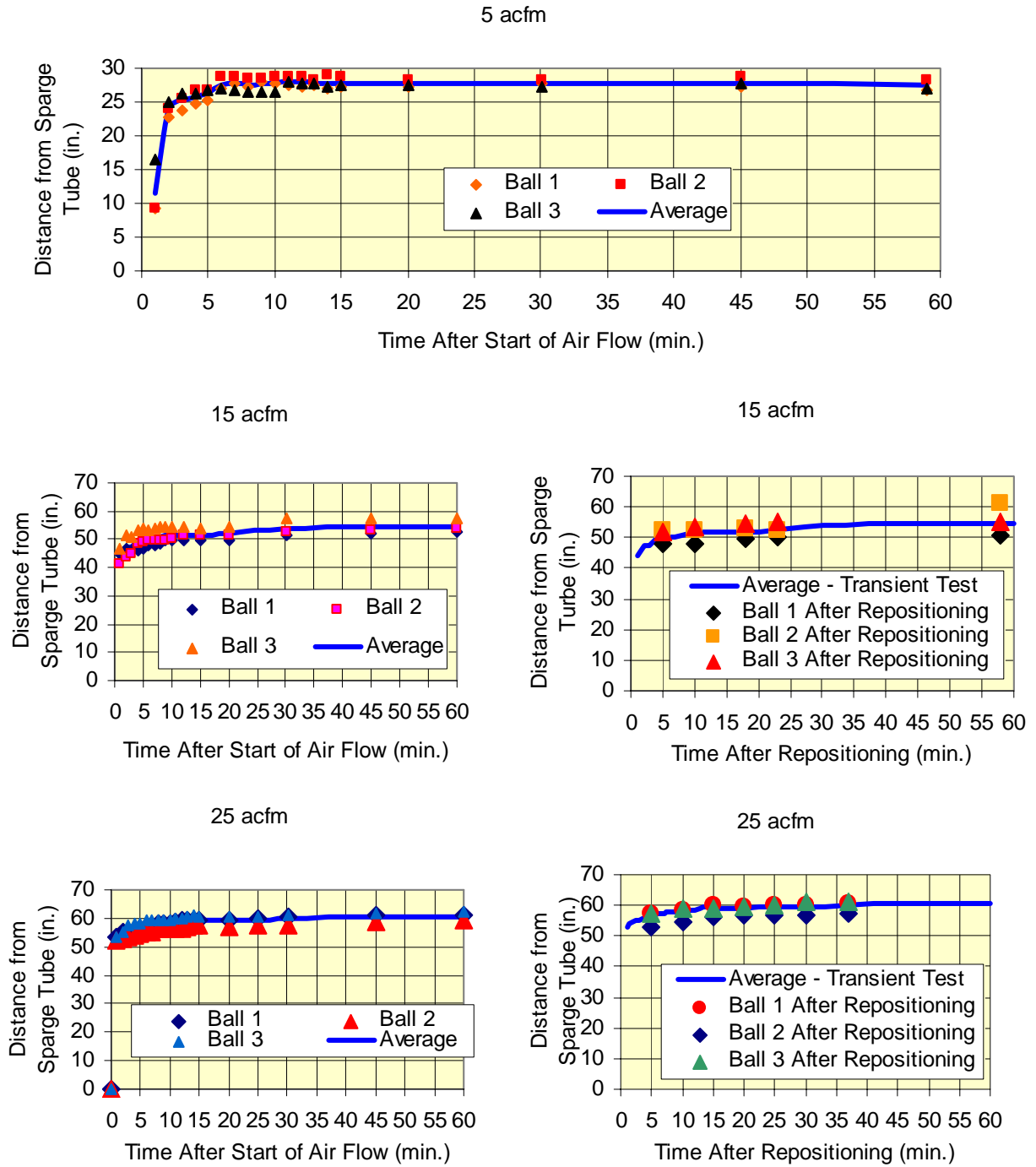


Figure 6.4. Surface Tracer Position Versus Time after Start of Sparger Air-Flow and After Tracer Repositioning

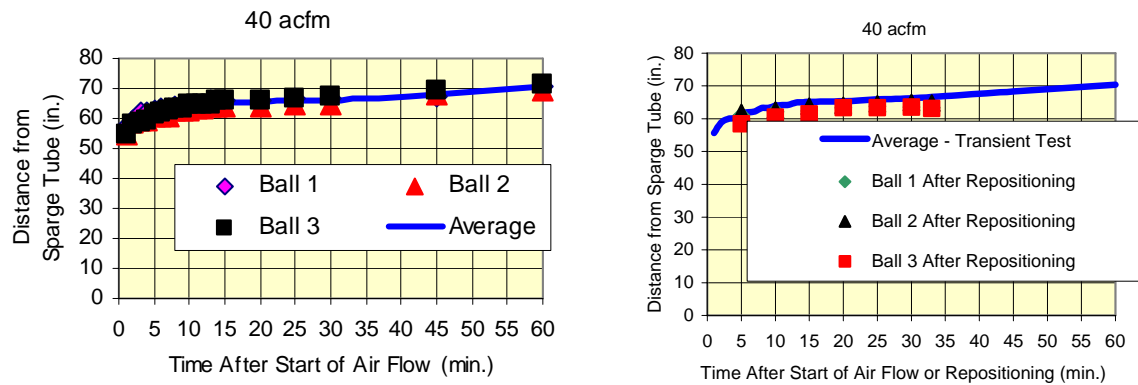


Figure 6.4 (contd)

The position of a given ball with time represents the progress of the ball in the transient flow field following the start of air flow. Therefore, in principle, the gradients cannot be used as a measure of the speed of the fluid at the surface in the ZOI. However, test results for subsurface “time to ZOI” reported later indicate that the ZOI is well established within one minute of the beginning of sparger air flow. Therefore, the gradients in Figure 6.4 (left side charts for 15, 25, and 40 ACFM flow rates) are representative of the actual fluid speed at the ZOI surface for various radial positions at the measured air-flow rates. Data shown in Figure 6.4 (charts on the right side for 15, 25, and 40 ACFM) support this conclusion. These charts show the movement of ping pong balls that were placed back at starting positions near the sparger tube 60 minutes after the start of sparger air flow. The air flow was continuous during the entire period. The solid curves are taken from the corresponding left side charts in Figure 6.4 and are the average position of the balls measured after the start of sparger air flow for the three air flow rates. The ball positions shown in Figure 6.4 seem to closely track the solid curves shown, indicating that the ZOI flow field is established quickly after the start of sparger air flow. Figure 6.5 (40 ACFM flow rate) provides further support for this conclusion. The movements of ping pong balls that were placed back at starting positions near the sparger tube 25 minutes after the start of sparger air flow are shown. Note that balls 1 and 2 “jumped” across the ZOI boundary at about 10 minutes following the start of sparger air flow. This is the result of the vigorous splashing at this high air-flow rate as verified by the video record.

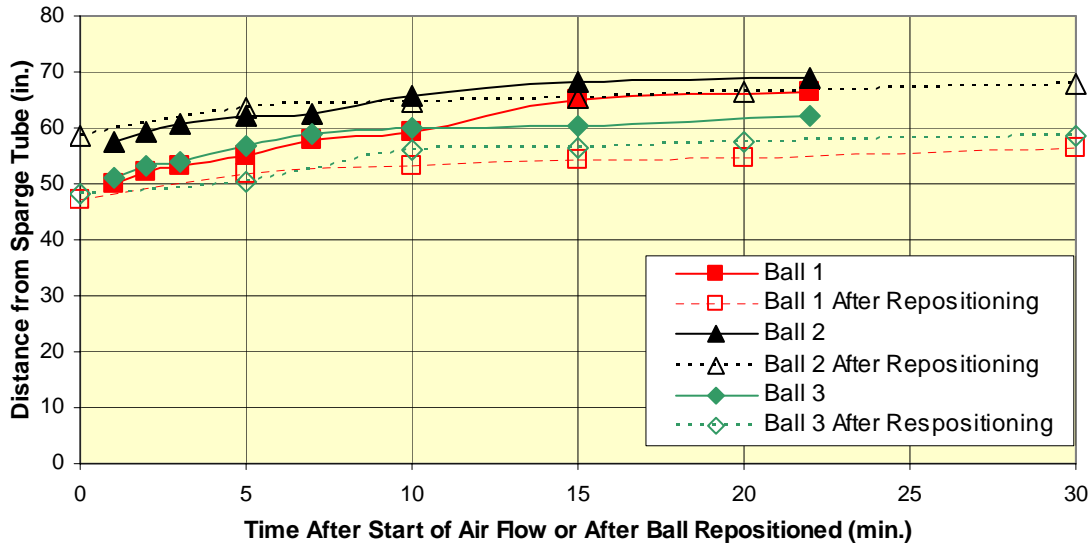


Figure 6.5. Surface Tracer Positions after Start of Sparger Air Flow (40 ACFM nominal) and After Repositioning Surface Tracers 25 Minutes into the Test Run

Based on the ping pong ball surface tracer tests, steady-state ZOI boundary radii at the surface for each flow rate were determined to be as shown in Table 6.1 (note that the tank radius is 76 inches). These data compare favorably to the steady-state results in the previous set of tests shown in Figure 6.2.

Table 6.1. Estimated Radius of Steady-State ZOI Boundary at Liquid Surface Versus Sparger Air-Flow Rate

Sparger Air-Flow Rate (ACFM Nominal)	Radius of Steady-State ZOI Boundary at Surface (in.)	ZOI Radius (in.) Calculated Using Relationship Shown in Figure 6.2
5	28	29
15	52	43
25	59	51
40	65	60

7.0 ZOI Subsurface Measurements Using an Ultrasonic Velocity Probe

This set of tests had the following objectives:

1. Determine the subsurface ZOI vertical boundary profile at steady state using an ultrasonic velocity probe (UVP).
2. Determine the time to reach the steady-state subsurface ZOI velocity profile using the UVP. The probe was placed at radii of approximately 67% and 95% of the ZOI radius (± 1 inch) at an immersion depth of $\frac{1}{2}$ of the sparge tube depth.
3. Determine ZOI vertical velocity profiles at 55 inches (nominal) below the liquid surface using the UVP.
4. Determine the location of the ZOI boundary below the sparger nozzle.

7.1 Materials and Methods

7.1.1 Apparatus

The single tube sparging test stand described in Section 5.1 was used for these tests.

7.1.2 Simulant

The kaolin/bentonite simulant described in Section 5.2 was used in these tests.

7.1.3 Methods Used

7.1.3.1 Determining Sparger Nozzle Submergence Depth and UVP Sensor Depth and Lateral Position

Figure 7.1 is a schematic of the UVP and sparge tube relative to the bridge top handrail and floor. The sparge tube nozzle submergence depth (D_{NS}) was readily obtained using the top of the upper bridge handrail as a reference and the measured values of D_{NRef} , D_{NH} , and D_L .

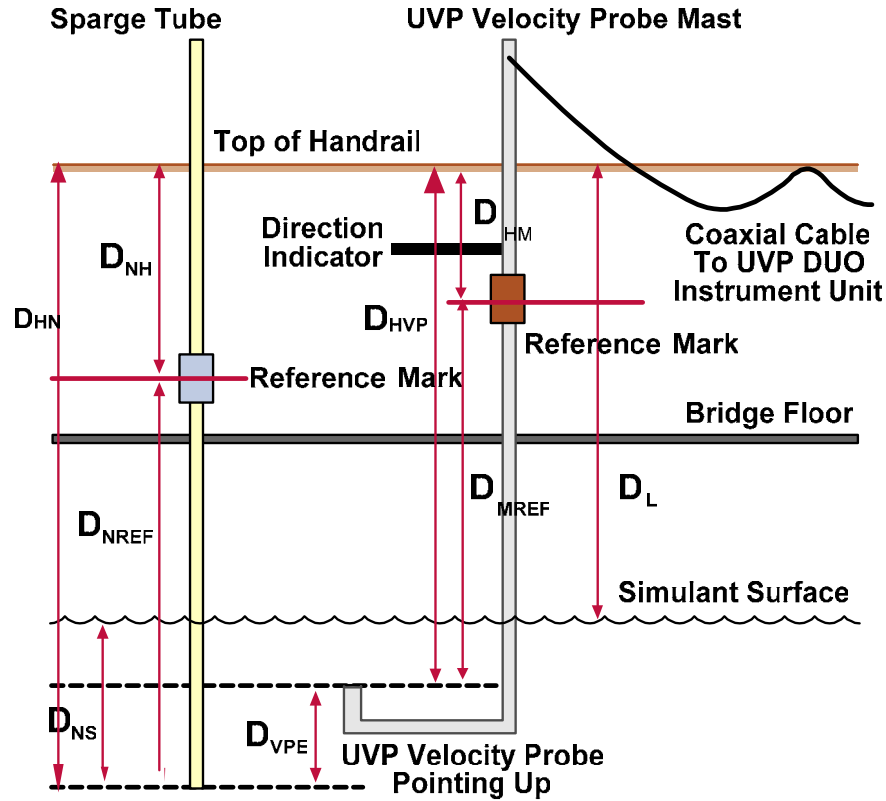


Figure 7.1. Schematic of the Dimensions Used to Establish the Positions of the Sparge Tube and UVP in the CBT

The velocity probe mast was marked at a distance D_{MREF} from the sensor face before inserting the UVP into the tank. The distance D_{HVP} from the sensor to the top of the handrail was found using the measured values of D_{HM} and D_{MREF} . D_{VPE} , the distance of the sensor above the sparge tube, was calculated using the measured values of D_{HN} and D_{HVP} .

The UVP mast was positioned so that the top of the handrail was at a distance D_{HM} from the mast reference mark (Figure 7.2) and then secured to the handrail. The UVP sensor direction indicator at the top of the mast was verified to be pointing toward the sparge tube and the probe mast was ensured to be vertical using a bubble level. The radial distance of the velocity probe mast to the sparge tube (D_{MLOC}) was calculated using the measured values of D_{MLOCX} and D_{MLOCY} . Because the 10.5-inch-long probe arm (shown in Figure 7.2) was always directed at the sparge tube, the true radial distance of the velocity probe from the sparge tube (D_{VP}) was therefore 10.5 inches less than D_{MLOC} .

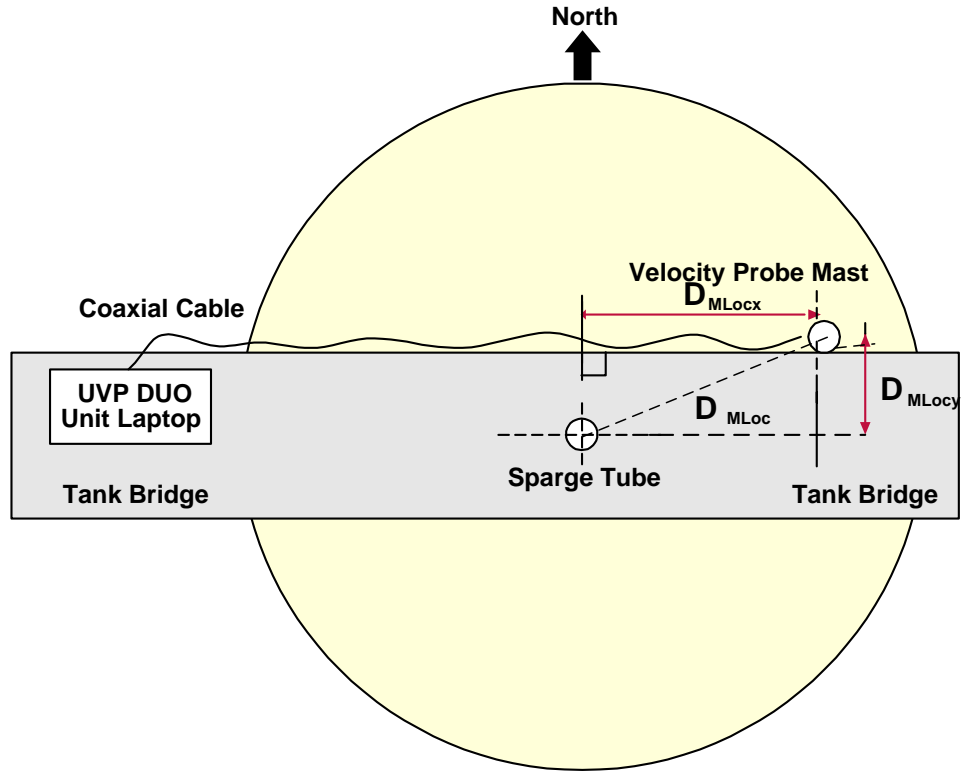


Figure 7.2. UVP and Sparge Tube Setup

7.1.3.2 UVP and Control Computer Setup

The instrument package consisted of a Met-Flow UVP-DUO MX velocity processing unit and an ImaSonic ultrasonic probe. The system was set up to measure fluid motion toward and away from the face of the transducer. The two tangential velocity components were not measured. The UVP probe was connected to the velocity processing unit that was in turn connected to a control computer. Measurement parameters, such as the speed of sound, the signal frequency, the velocity range and the sampling time, were set using the supplied computer software.

Sampling time was selected to ensure logging for at least one minute and measurement stopped when the selected logging period had elapsed. The average velocity value for the measurement band 40 mm from the probe face was used. Because the “zero range” for the UVP is specified by the manufacturer as an average velocity of 0 ± 2 mm/s, average velocity values measured within that range were considered to indicate no flow.

7.1.3.3 ZOI Subsurface Boundary Profile

The procedure for determining the boundary profile points of the steady state ZOI is described below. At least four boundary points at various depths were determined for each air-flow rate so that the shape of the profile could be resolved in sufficient detail.

The air-flow valve on the manifold was opened to obtain the desired flow rate and the actual flow rate at the sparger nozzle was calculated. Air flow was adjusted as required to bring the flow rate at the nozzle to within ± 2 ACFM of the desired flow rate. Air flow was then stopped using a valve upstream of the sparger nozzle. The UVP software was initialized, as described previously, and the measurement parameters were saved.

The sensor support arm alignment with the direction indicator on the probe mast was checked using a laser level and adjusted as required. The UVP mast was then moved along the handrail to position the sensor just outside the ZOI steady state boundary radius for the selected sensor submergence depth and sparger air flow rate. The UVP sensor was lowered to the prescribed depth and the mast was clamped in position. The valve upstream of the sparger was opened and sparging was carried out for the time period required to ensure steady state conditions.

The ZOI boundary point for each selected measurement depth was determined using a binary search method. The process was considered complete for the selected sensor depth when a velocity inside the zero range and a velocity outside the zero range had been measured within 3 inches (laterally) of each other. The ZOI boundary position for the selected sensor depth was assumed to be the average of the two radial distances of the sensor probe from the sparge tube.

7.1.3.4 Subsurface Transient ZOI Behavior

The test procedure for the “time to ZOI” tests is summarized below.

The sparger air flow was stopped during the positioning of the UVP mast. The sensor arm alignment with the indicator on the probe mast was checked and adjusted as required. The UVP mast was moved along the handrail to the position corresponding to the radial position with respect to the sparger where the vertical velocity as a function of time was to be monitored—66% and 95% of the steady state ZOI boundary radius at the prescribed depth. The UVP sensor was lowered to the prescribed depth and the mast was clamped in position.

The air-flow valve on the manifold was opened to obtain the desired flow rate. The actual flow rate at the sparger nozzle was calculated and the air flow was adjusted as required to bring the flow rate at the nozzle to within ± 2 ACFM of the desired flow rate. Air flow was shut off using a valve upstream of the sparger nozzle. The UVP software was initialized, as described previously, and the measurement parameters were saved. Logging of the velocity probe data was started. The valve upstream of the sparger was opened and the start time for the initiation of air flow was recorded. The time, air-flow rate, air pressure, temperature, and manifold line number (e.g., F-1) were recorded in the LRB and on the data sheet and periodically throughout the test run. The test run continued until near constant velocities were observed for a period of about 15 minutes.

7.1.3.5 ZOI Velocity Profile Measurements

The test procedure for the vertical velocity measurements in the ZOI are summarized below.

The air-flow valve on the manifold was opened to obtain the desired flow rate. The actual flow rate at the sparger nozzle was calculated and the air flow was adjusted as required to bring the flow rate at the

nozzle to within ± 2 ACFM of the desired flow rate. Air flow was shut off using the valve upstream of the sparger nozzle. The UVP software was initialized and the measurement parameters were saved.

The sensor arm alignment with the indicator on the probe mast was checked and adjusted as required. The UVP mast was moved along the handrail to position the sensor just beyond the ZOI steady state boundary radius for the selected sensor submergence depth and sparger air-flow rate. The UVP sensor was lowered to the prescribed depth and the mast was clamped in position.

The valve upstream of the sparger was opened and sparging was carried out for the time period required to ensure steady state conditions. The velocity was measured and recorded. The UVP mast was moved inboard along the handrail a distance of about 6 inches. The UVP sensor lateral and vertical positions were verified and adjusted as required. The vertical velocity was measured and recorded. This process was repeated until the UVP sensor was about $\frac{1}{3}$ of the ZOI boundary radius from the sparge tube.

7.1.3.6 ZOI Boundary Below the Sparger Nozzle

The test procedure to measure the ZOI boundary position below the sparger nozzle was similar to that previously described for vertical velocity profile measurements in ZOI. In preparation for these tests, the UVP sensor mounting arm length was increased to 20 inches from 10.5 inches. The sensor orientation remained vertical. The UVP mast was moved to a position along the handrail such that the sensor was about 24 inches directly below the sparger nozzle. The mast was clamped in position and the vertical velocity component was measured. The mast was then moved upward in increments of 1 to 4 inches until a positive average velocity (indicating up flow) outside of the zero range was measured. The mast was clamped in position before each measurement was made.

7.2 Results and Discussion

7.2.1 Subsurface ZOI Boundary Profiles

Figure 7.3 shows the results of the ZOI subsurface boundary measurements for all tests. Surface ZOI boundary data are based on the surface tracer tests (see Table 6.1). Note that the liquid surface, tank walls, and sparge tube are shown, including the position of the sparger nozzle. The boundary position with respect to the sloping portion of the tank wall appears to be consistent with the slope of the wall. The uncertainty in the vertical position of the UVP sensor was estimated to be ± 2 inches. Uncertainty in the lateral position was estimated to be about ± 4 inches for measurements made between 0 and about 50 inches from the tank bottom (“tank elevations”). Lateral position uncertainties for tank elevations greater than 50 inches were estimated to be about ± 2 inches. Figure 7.4 shows a second order polynomial fit of the data for 40 ACFM. Confidence boundaries of 95% are shown. Data presented in the next section for the depth of ZOI below the sparger nozzle suggest that the polynomial fit shown is not adequate for vertical positions within 10 inches of the tank bottom.

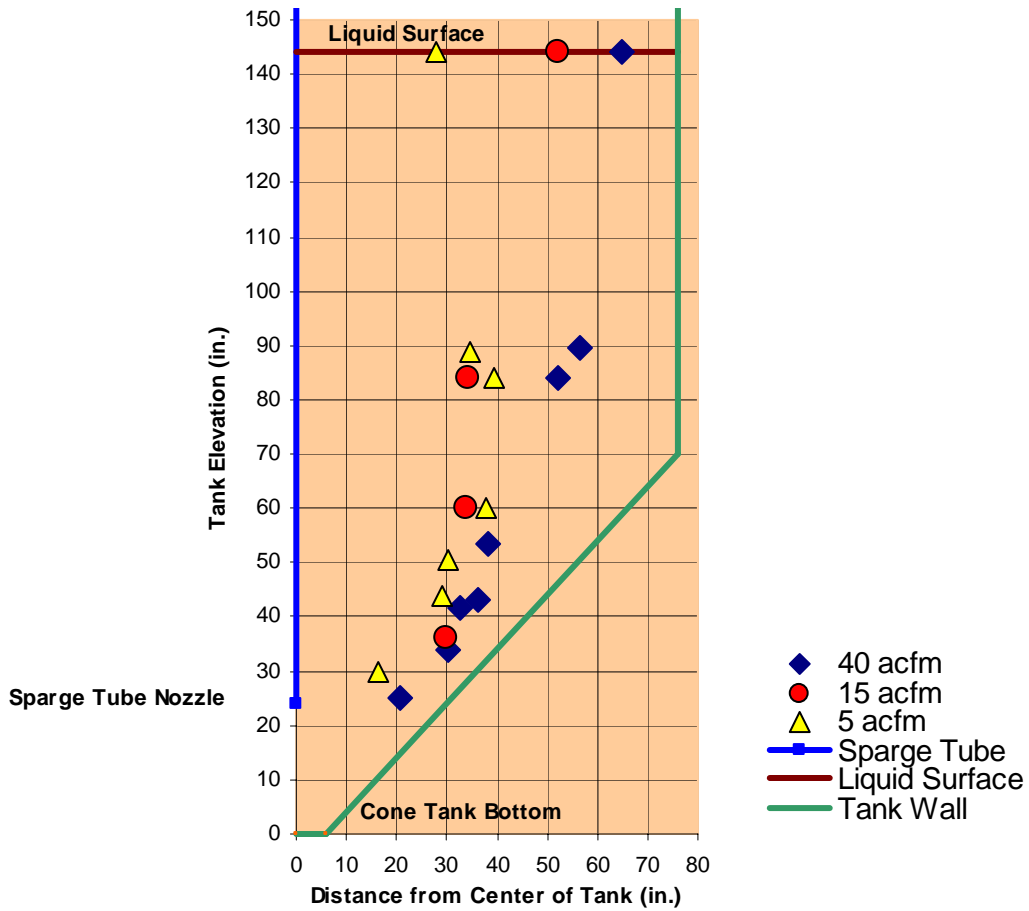


Figure 7.3. Subsurface ZOI Boundary Measurement Data for all Test Runs

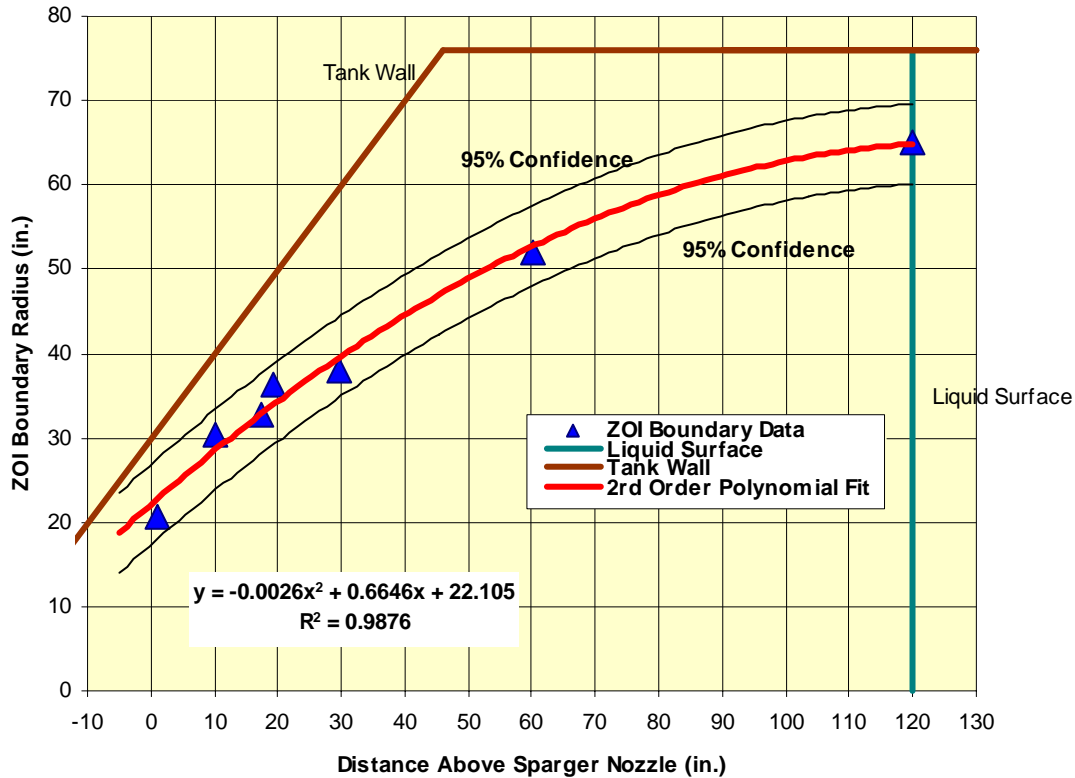


Figure 7.4. Subsurface ZOI Boundary Measured Data for 40 ACFM Including Polynomial Curve Fit

7.2.2 Subsurface Transient ZOI Behavior

Figure 7.5 shows the results of tests at 15 and 40 ACFM (nominal) with the UVP sensor positioned at both 66% and 95% (nominal) of the ZOI radius, 55 inches and 60 inches below the liquid surface. The data for 15 ACFM suggest that steady-state ZOI conditions are established within about one minute of the start of sparger air flow, beginning with a quiescent tank. The data for 40 ACFM, with the sensor positioned at a radius of 66% of the expected ZOI steady-state boundary radius, also support this conclusion. The data for 40 ACFM with the sensor positioned at a radius of 95% of the expected ZOI steady-state boundary radius suggest that the probe was positioned too close to the ZOI boundary, possibly within the boundary itself. This is indicated by the more pronounced velocity fluctuations (ranging from about 1 to 8 mm/s) during the 30-minute duration of the test and the lower than expected absolute velocity values. Note that for all tests, the UVP sensor was positioned to measure only the vertical velocity component, and negative velocity values indicate flow toward the tank bottom.

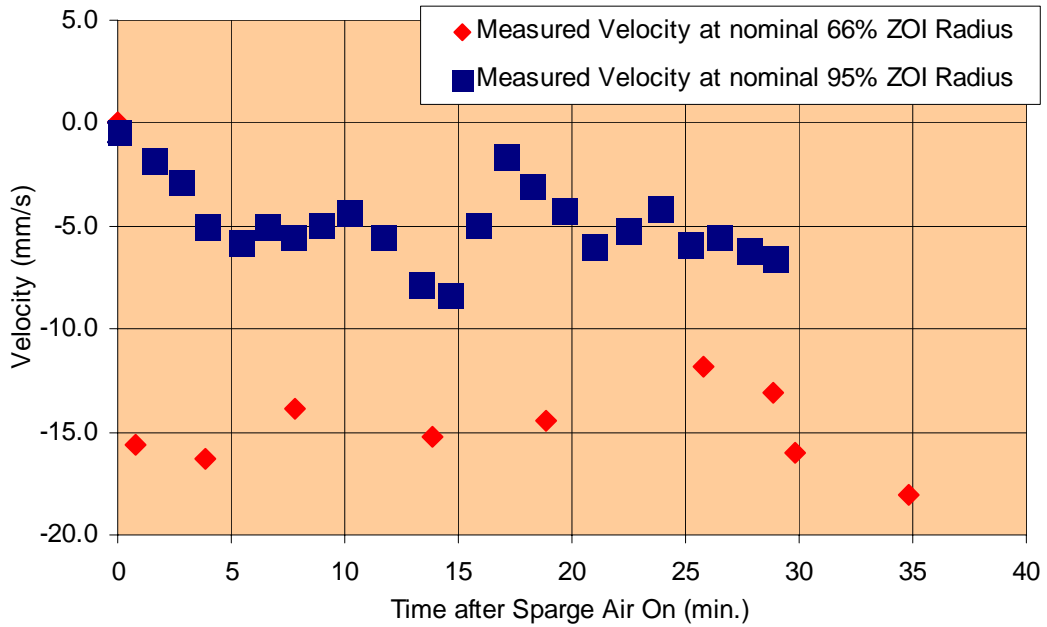
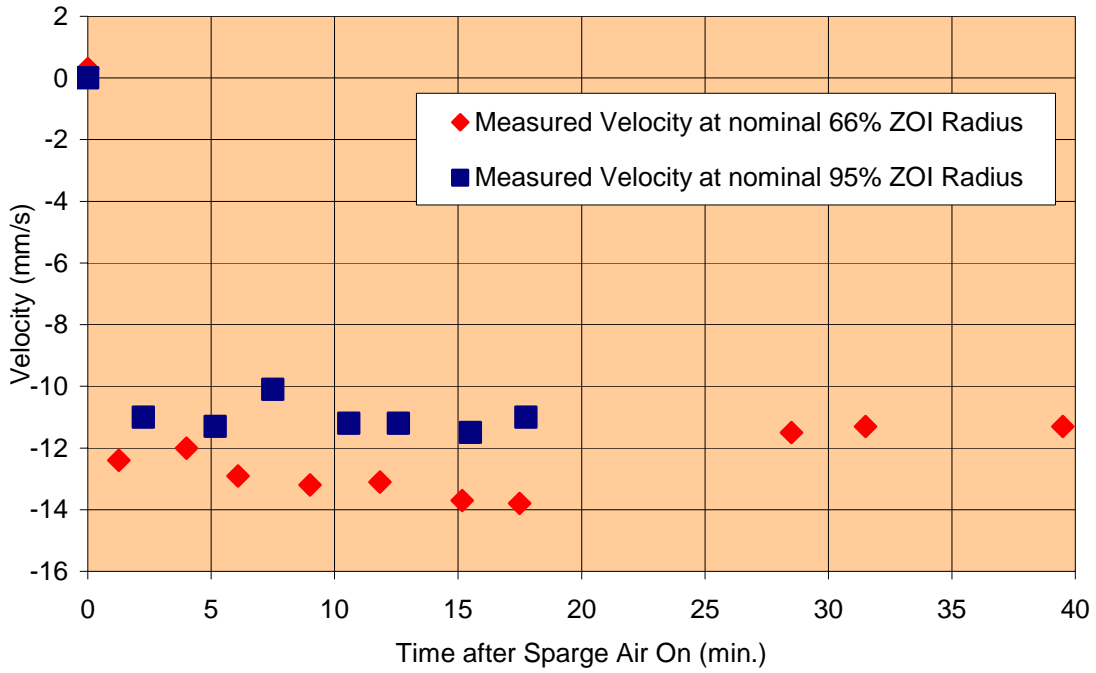


Figure 7.5. Subsurface “Time to ZOP” Measurement Results Using the UVP (15 ACFM top; 40 ACFM bottom)

7.2.3 ZOI Velocity Profiles

Velocity profile data were adjusted using the UVP calibration data shown in Figure 7.6. Calibration corrected data for the two flow rates (5 and 40 ACFM) are shown in Figure 7.7. Note that here downward velocity is shown as positive. The “Zero Range” for the UVP is specified by the manufacturer as an average velocity of 0 ± 2 mm/s. Average velocity values measured within that range were considered to indicate no flow. The pronounced “dips” in both velocity profiles may indicate the presence of outer and inner ZOI flow cells. The ZOI cellular structure observed in the T-34, clear tank tests, is discussed in Section 4. The ZOI boundary points indicated are also plotted in Figure 7.3 and Figure 7.4.

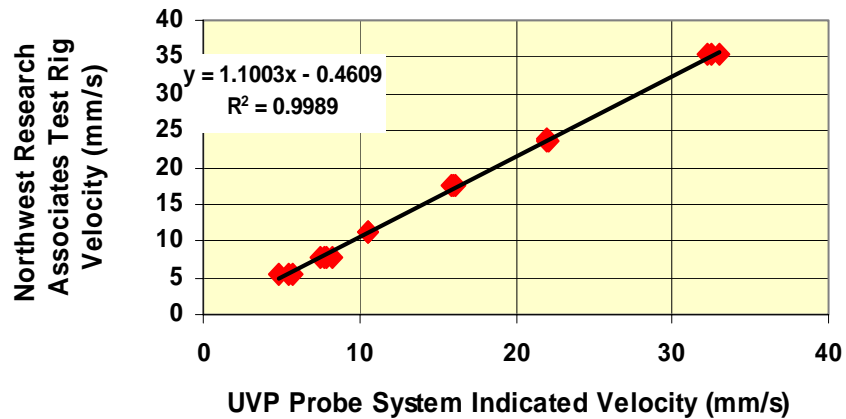


Figure 7.6. UVP Probe Calibration Results for Range of Interest

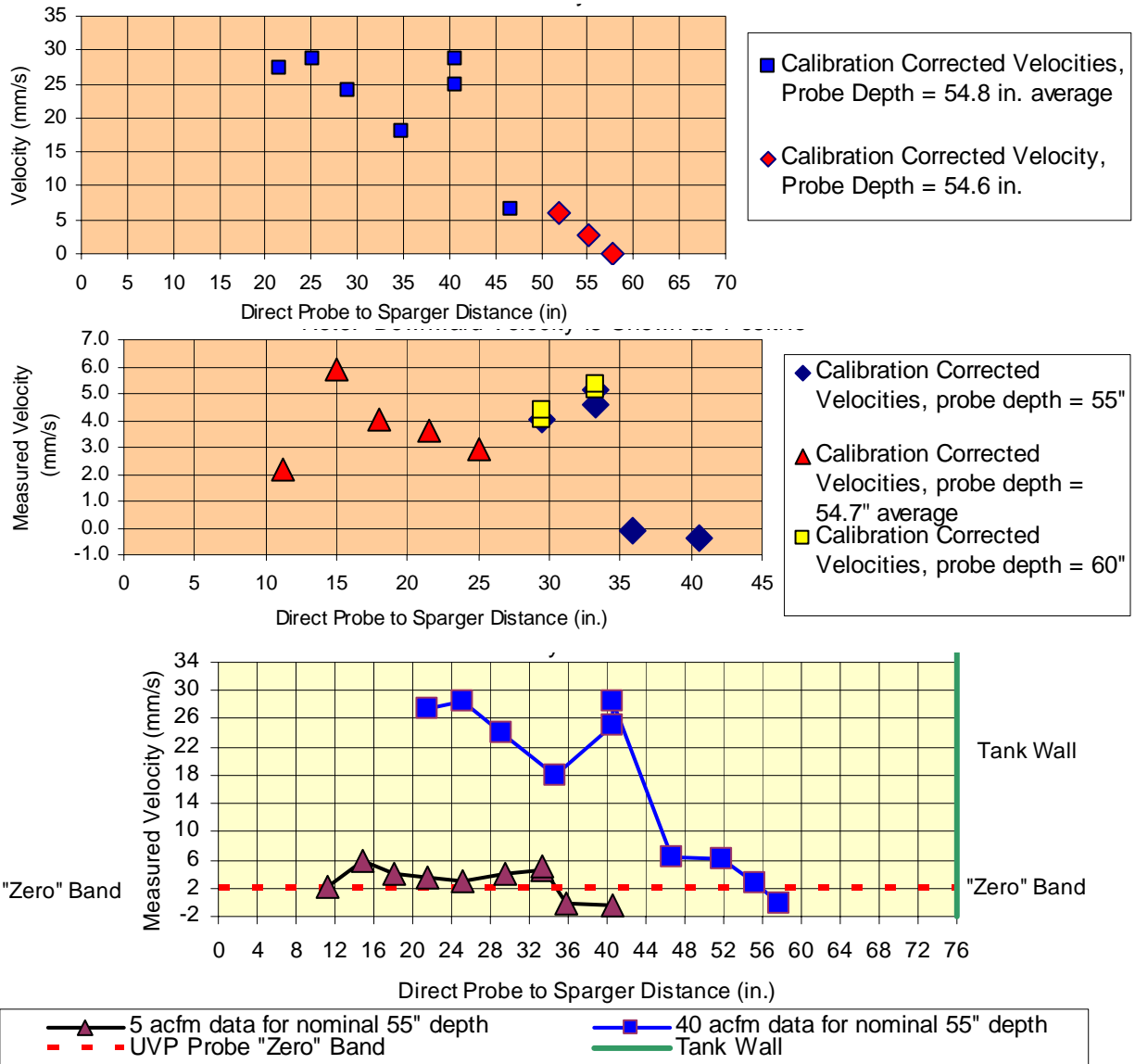


Figure 7.7. ZOI Vertical Velocity Profiles for Various Sparger Nozzle Air-Flow Rates (40 ACFM top; 5 ACFM middle; 5 and 40 ACFM bottom)

7.2.4 Depth of the ZOI Boundary Below the Sparger Nozzle

Figure 7.8 shows the results of tests carried out using the UVP to determine the position of the ZOI boundary directly below the sparger nozzle for nominal sparger air-flow rates of 5 and 40 ACFM. The nozzle was positioned 78 inches above the tank bottom and 66 inches below the liquid surface for these tests. As previously described, the UVP sensor was positioned well below the nozzle and moved incrementally vertically upward toward the nozzle until positive (upward) velocities were indicated.

The interpretation of the results is complicated by the fact that the UVP zero range is ± 2 mm/s. Nevertheless, it appears that measurable upward flow, probably due to entrainment by the forming

bubbles at the sparger nozzle, can be detected about 8 to 9 inches below the nozzle for 40 ACFM and about 2 to 3 inches below the nozzle at a nozzle flow rate of 5 ACFM. Evidence of the ultrasonic beam having penetrated the bubbles was clear for data sets gathered closer to the nozzle. The standard deviation of velocity was observed to increase rapidly (“explosively”) with increasing distance from the probe face when the sensor was moved closer than the closest positions shown for the two flow rates in Figure 7.8. These data are not shown in Figure 7.8. Note that positive average velocity indicates upward flow. Overall, the results suggest that the flow/no flow boundary directly below the nozzle are within 10 inches of the nozzle for flow rates up to 40 ACFM. For 5 ACFM, the flow/no flow boundary is within 3 inches of the nozzle.

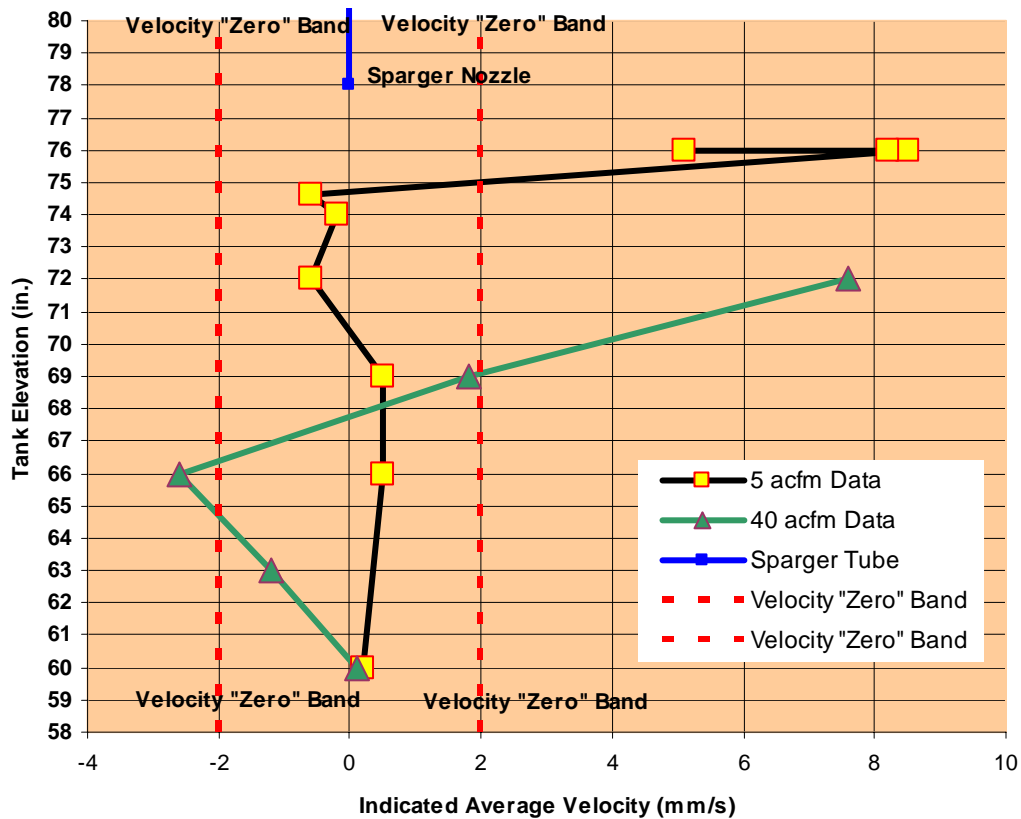


Figure 7.8. Results for ZOI Boundary Below the Sparger Nozzle

8.0 ZOI Subsurface Measurements Using Passive Integrated Transponders Tags

The objective of this set of tests was to determine the subsurface ZOI vertical boundary profile at steady state using passive integrated transponders (PIT tags) techniques.

8.1 Materials and Methods

8.1.1 Apparatus

The single tube sparging test stand described in Section 5.1 was used for these tests.

8.1.2 Simulant

The kaolin/bentonite simulant described in Section 5.2 was used in these tests.

8.1.3 Methods Used

This research was conducted to determine the ZOI boundary at various sparger air-flow rates and various sparger nozzle depths. The ZOI boundary was located by detecting PIT tags immersed in and moving with the simulant.

PIT tags (model 1411ST PIT tags, Biomark, Inc., Boise, ID.) are small radio frequency identification tags. Each tag is a read-only tag that is programmed to transmit a unique code (at 134.2 kHz) when activated by a PIT tag transceiver/reader. PIT tags are integrated circuits with an antenna that is encapsulated in glass. The term passive refers to the fact that there is no battery on the tag. The tag is powered through the activation of a handheld or stationary transceiver/reader that generates an electromagnetic signal used to momentarily activate the tag. When activated by the reader, the tag transmits a unique digital code back to the reader where the code is displayed and/or stored. The tag only transmits its unique code when the tag is present in the transceiver's electromagnetic activation field. PIT tags are cylindrical in shape. The PIT tags we used were 12 mm long and 2.1 mm in circumference and had a mass of 90 mg.

Approximately 6000 tags were placed in the simulant by randomly spreading them on the surface of the simulant. They were vigorously mixed into the simulant by manually moving a portable sparger tube around the perimeter of the tank while simultaneously sparging using the test sparger tube.

Pit tags were located using three custom-made antennas, each 4 cm in diameter and 25.5 cm long and specially designed to operate inside of a length of 5.08 cm PVC pipe. The antennas had a detection range of approximately 8 to 10 cm (see Figure 8.1). The red area indicates the reception range when a PIT tag axis is perpendicular to the axis of the antenna while the blue area indicates the reception range when the PIT tag axis is aligned parallel to the long axis of the antenna. The effect of the specific shape of the antenna range on the effective range for each antenna was not significant for these tests.

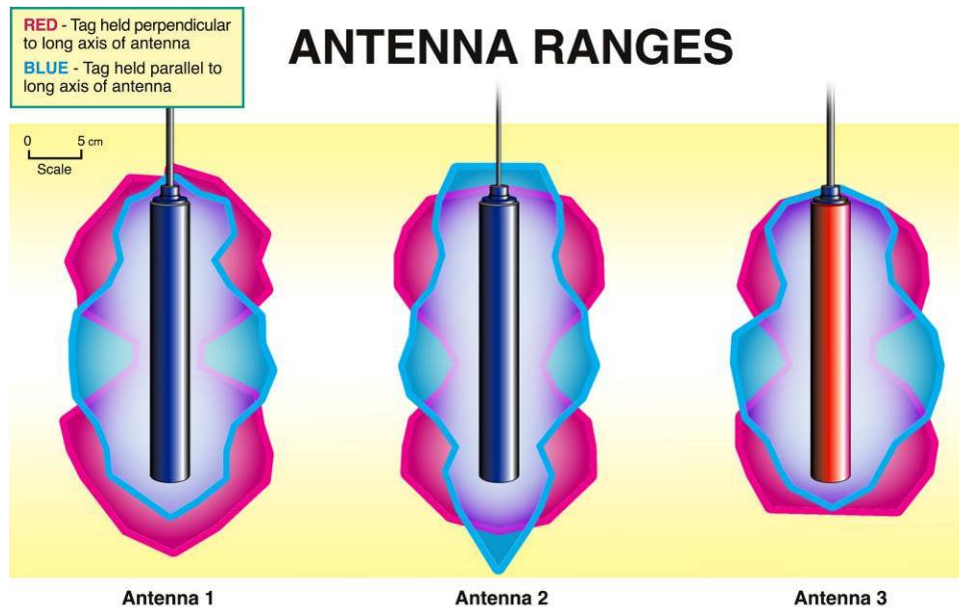


Figure 8.1. Approximate Antenna Ranges of Three Custom Antennas Used to Identify PIT Tags

Polyvinyl chloride (PVC) pipes were used as wells for the antennas to travel inside. These antenna wells were placed at various locations within the simulant to determine whether there was movement of tags within the reception range of the antennas.

Initially, antennas were moved up and down inside the antenna wells manually by using a system of ropes and pulleys. The depth location of the antennas inside the wells was noted by examining a measuring tape that was fastened to the antenna cable at a known point. Later, a specialized system (see Figure 8.2) was developed for moving the antennas up and down within the pipes. This system also relayed the depth location of the antenna within the pipe, making the measuring tapes and rope and pulley systems obsolete.

The automated antennas were driven by small electric motors that were wired for remote operation. The motors were connected to an encoder (US Digital, Model A2-S-B-M), which counted the number of clicks when the antenna moved up or down on its corrugated track. The encoders were wired into a computer. Multiple encoders were spliced into one Category 5 cable using three-way conductor jacks (US Digital, Model CON-MD6-3J). A2 software (US Digital) was used to convert the number of clicks into a distance in centimeters.

Then antenna cables were connected to Destron-Fearing FS2001F PIT-tag readers. These readers recorded the code of individual PIT tags as they were interrogated by the antenna. The reader could record the tag identifications in memory or route them to a computer.

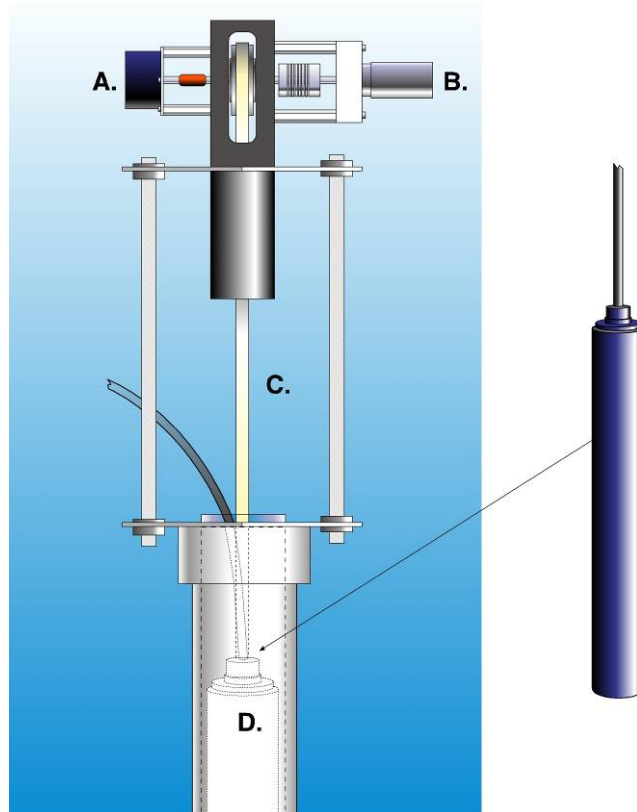


Figure 8.2. An Automated System for Moving PIT Tag Antennas Inside of Antenna Wells. A small motor (B) is used to move antennas (D) up and down inside of a PVC pipe. Antennas are attached to a flexible track (C). The location of the antenna can be determined by the encoder (A).

Real-time information was transferred from the PIT tag readers to computers in a control room. Each reader was connected to a RocketPort universal serial bus (USB) hub via serial cable (Comtrol, Maple Grove, MN). The USB serial hub was linked to a computer using an Icron USB Ranger 110 (Icron, Burnaby, BC, Canada). The USB Ranger consisted of two units. One unit was connected to the USB serial hub while the other unit was connected to the computer. The two USB Rangers were connected by Category 5 network cable (~ 75 m).

Minimon software (PTAGIS, Portland, OR) was used to log the occurrence of PIT tags. This software recorded the date, time, and antenna by which the PIT tag was located. Two computers were used for this process. At most, each observer monitored two antennas on a single computer.

The antenna wells were placed into the simulant, perpendicular to the surface. Antennas were attached to a walkway that ran across the center of the tank. The location of each antenna was measured to determine the distance and direction from the center of the tank. As the tests progressed, antennas were moved to different locations to narrow down the border of the ZOI. This was done by lifting the antenna wells straight out of the simulant and then placing them in a new location, which was then measured and recorded.

To set the zero position for the antennas (zero was by definition the surface of the simulant), the antennas were moved to a position where the lower tip was at or above the top of the simulant. A tag was placed on the end of a pole and positioned along the antenna pipe at the surface of the simulant. The antenna was then slowly lowered down until the tag was detected. After a tag was first detected, the elevation of the antenna was slowly raised until the tag could no longer be detected. Then the antenna was lowered until the tag was heard again. The elevation of the tag was fine tuned by raising and lowering the antenna. After the surface of the simulant was located, the encoder software was reset to zero, the location of test tags could begin, and all tag locations were referenced from the surface of the simulant. The same procedure for finding the surface of the simulant was used for finding test tags.

When a tag was located, the height, time, and tag ID were recorded on a data sheet, and the antenna was moved down until another tag was detected or until the beacon tag was heard. The beacon tag was a tag taped to the outside of the antenna well at the lower end of the antenna-driving range so that the observer would not attempt to drive the antenna past the bottom of the well and in doing so break the track on which the antenna rode.

This process resulted in one “pass” of the detection area. To determine movement, several passes were made. All tags were located by moving the antenna down, not up, so once the bottom beacon tag was heard, the antenna was driven all the way up to the surface, and the process of locating tags was resumed. If a tag was observed at the same elevation on subsequent passes, it was determined that the simulant at that elevation was not moving. If a tag was observed at a different elevation (by more than about 13 cm) or no longer observed at all, or if a new tag was observed where there was none on the previous pass, the simulant at that elevation was determined to be moving.

During the test, a graph of the test tank was created on a dry erase board in the control room with tank radius on the x-axis and tank height on the y-axis. When a tag was found to be moving, a green mark was placed on the graph in the appropriate location. When a tag was found to be not moving, a red mark was placed on the graph. This gave the test engineer a visual display to aid in making decisions about where more data needed to be collected. A test was usually completed when the boundary between moving and non-moving tags was located. The graph would show at least one radial location with all moving tags, one with all non-moving tags, and one with a mix of moving and non-moving tags.

Occasionally no tags could be located when an antenna well was positioned in a new location. When this occurred, it was not known if the simulant was moving or not. When this happened, the test engineer would choose either to move the antenna well to a new location or to “seed” tags at predetermined locations within the reception range of the antenna. To accomplish this, a seeding pole was constructed. The seeding pole was made from two 3.05-m-long, 3.8-cm-diameter lengths of PVC pipe that were connected using couplers. A binder clip was attached to the lower end of the pipe. A nylon cord was tied onto the binder clip and threaded through a series of screw eyes turned into the pipe beginning just above the binder clip wire. The pipes were then marked every 15.24 cm.

To seed a PIT tag, it was placed in the binder clip, and the seeding pipe was slid along the antenna well to the predetermined depth. To achieve the proper depth, either the seed pipe markings were used, or the antenna was positioned at the desired depth within the well and the seed released when a positive read was confirmed. To release the tag, the nylon cord was pulled to open the clip, and the seed pipe was given a ½ turn to allow the tag to release.

8.2 Results and Discussion

Previously unreported subsurface ZOI boundary test data for tests carried out using the PIT Tag technique, and predating the UVP based tests discussed previously, are included below.

Eight test runs were carried out at two sparger nozzle depths (nominally 66 inches and 118 inches) and at nominal nozzle air flow rates of 5, 12, 20, and 30 ACFM. Data were acquired in multiple quadrants around the sparge tube (typically between 2 and 4 quadrants) for each run.

Figure 8.3 through Figure 8.7 show the results for six test runs. Note that the uncertainty in the lateral position of each data point is estimated to be ± 4 inches based on the antenna patterns and orientation of the PIT tag axes discussed previously.

Based on these data, the minimum and maximum ZOI steady-state subsurface boundary position was estimated. The boundary was assumed to be in the region where both red and green tags are evident (green data points represent moving PIT tags and red data points represent stationary PIT tags). It was assumed that the boundary was vertical throughout the extent of the mixed red and green zone. The boundary radii estimates are shown in Figure 8.8. No estimates are shown for 20 ACFM. Data are sparse for that flow rate and the antenna did not appear to have been positioned adequately to define the boundary region. Results for the 118-in. sparger nozzle depth can be roughly compared to the results for 5 and 15 ACFM flow rates shown in Figure 8.3 (based on the UVP data). The PIT Tag test results suggest that the ZOI boundary radius is about 5 inches greater than that suggested by the results in Figure 8.3 for approximately the same depths below the liquid surface. However, these larger ZOI radii are in good agreement with the results of the surface tracer technique discussed in Section 6.0 and shown in Figure 8.8 for comparison.

In general, the data for some of the PIT Tag test runs suggest that the ZOI boundary is following the tank wall in the sloping section. However, it appears that the ZOI boundary in that region would have been defined if these tests had been extended to probe the region closer to the sparger tube at depths close to that of the nozzle. Overall, the PIT Tag technique holds considerable promise for defining subsurface flow/no flow boundaries.

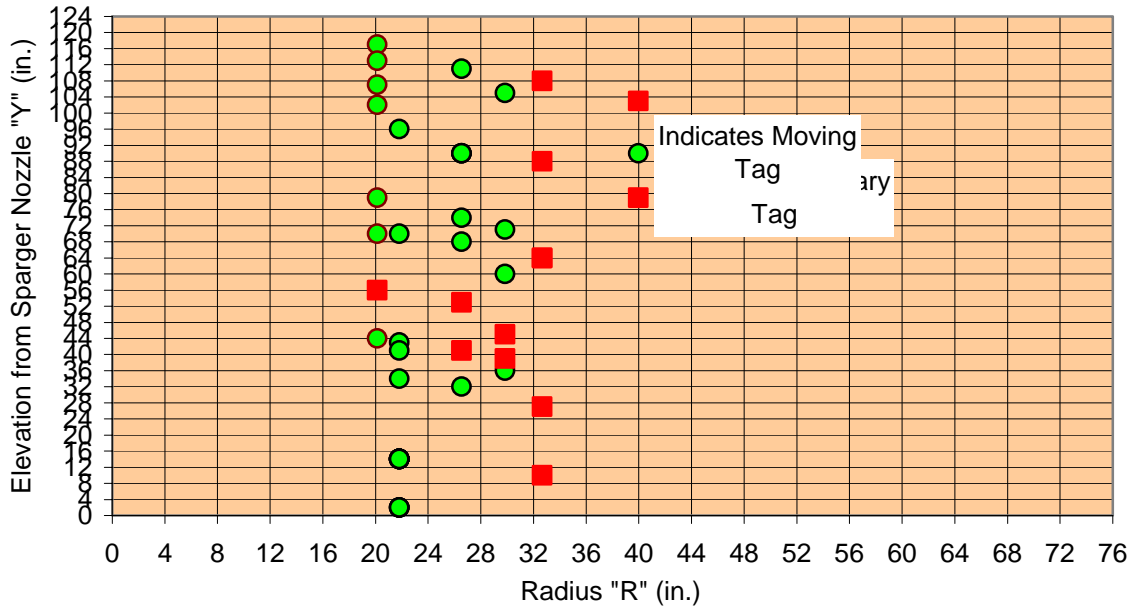


Figure 8.3. PIT Tag Data at 5 ACFM Nominal Air Flow and 117-in. Nozzle Submergence

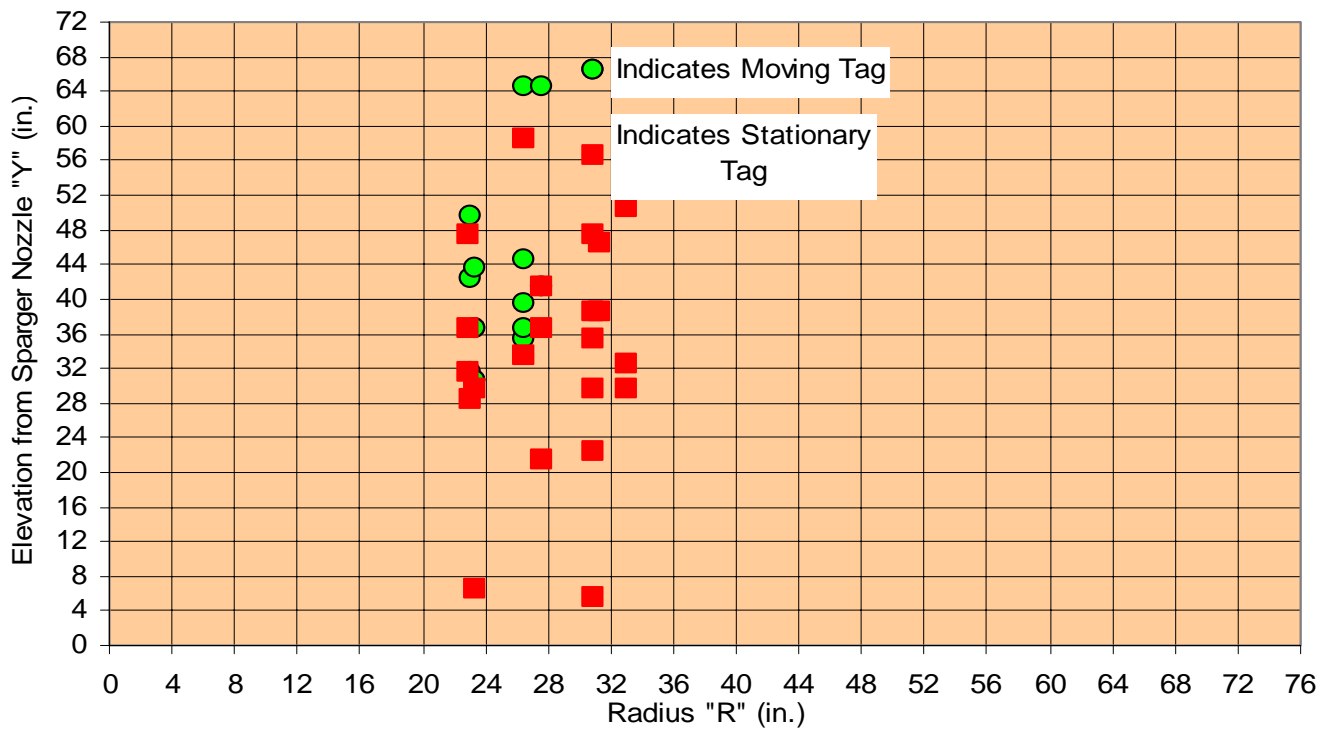


Figure 8.4. PIT Tag Data at 5 ACFM Nominal Air Flow and 66.5-in. Nozzle Submergence

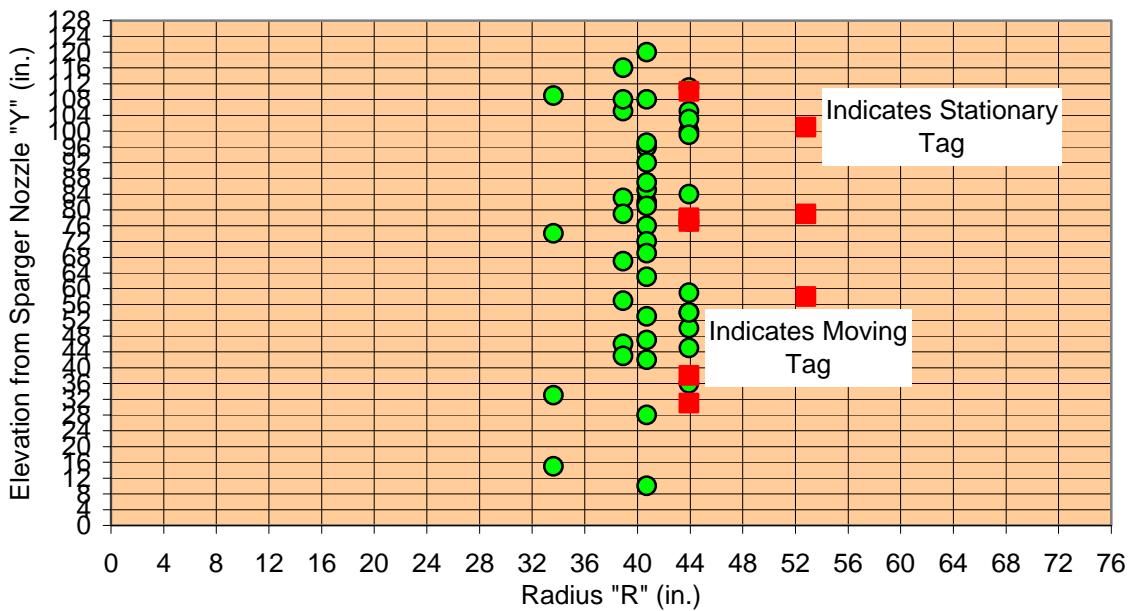
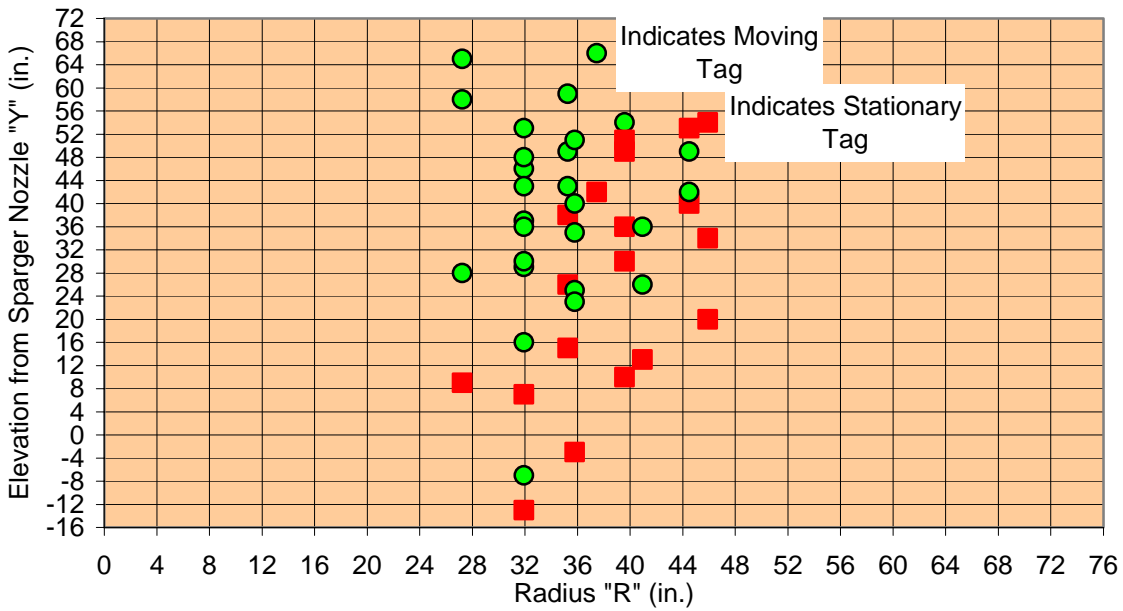


Figure 8.5. PIT Tag Data at 12 ACFM Nominal Air Flow and 66-in. (Upper) and 118-in. (Lower) Nozzle Submergence

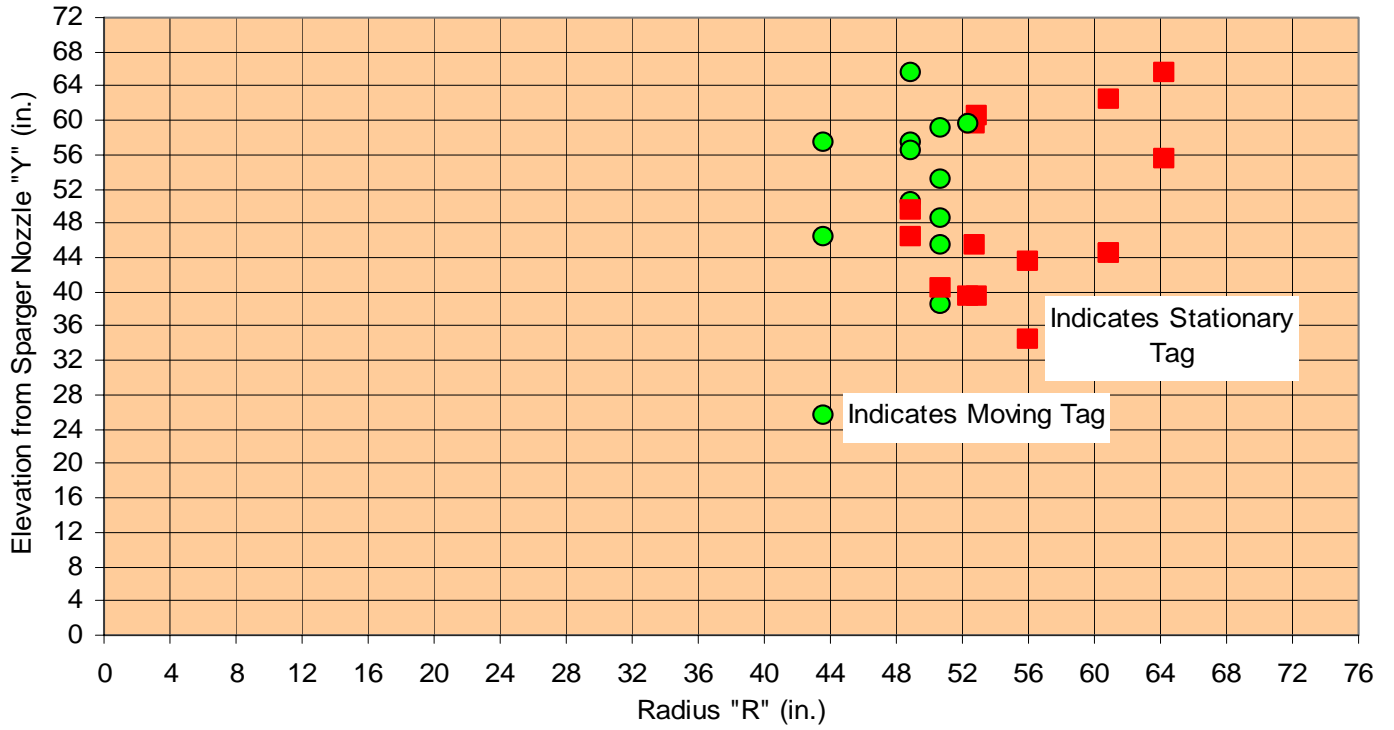


Figure 8.6. PIT Tag Data at 30 ACFM Nominal Air Flow and 66.5-in. Nozzle Submergence

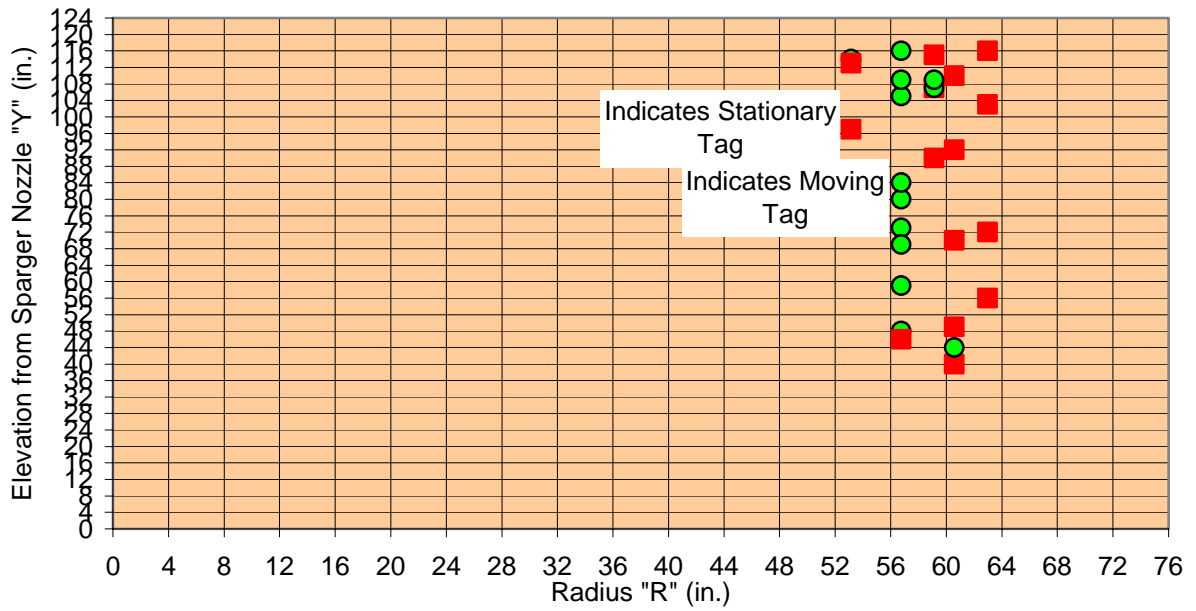


Figure 8.7. PIT Tag Data at 30 ACFM Nominal Air Flow and 117-in. Nozzle Submergence

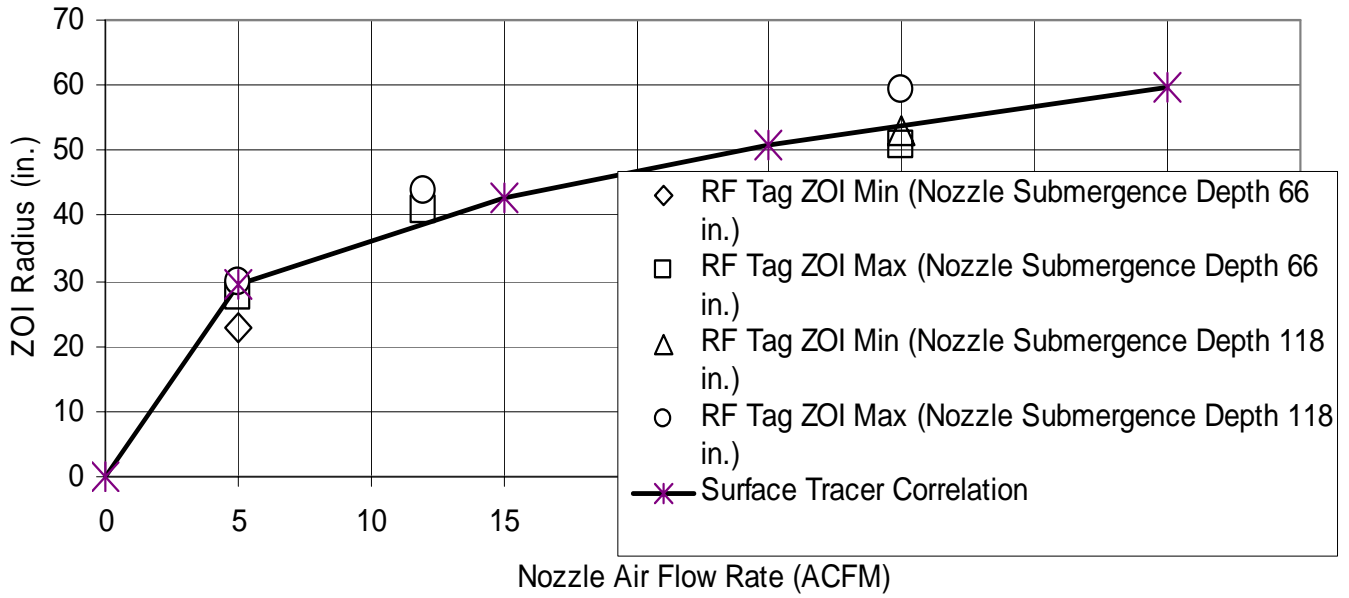


Figure 8.8. ZOI Boundary Summary from PIT Tag Data Various Air-Flow Rates and Nozzle Submersion Depths

9.0 ROB Subsurface Measurements Using An Ultrasonic Probe

The purpose of these tests was to determine the size and shape of the submerged ROB at various air-flow rates. Ultrasonic amplitude measurements were used to identify submerged locations that contain a large fraction of bubbles. This section describes these tests and results.

9.1 Materials and Methods

9.1.1 Apparatus

The single tube sparging test stand described in Section 4.1 was used for these tests.

9.1.2 Simulant

The kaolin/bentonite simulant described in Section 4.2 was used in these tests.

9.1.3 Methods Used

Ultrasound in the frequency range from 0.5 MHz to 10 MHz has the capability to penetrate dense slurries and opaque fluids. This property has been used to interrogate dense opaque slurries to characterize physical and rheological properties, including slurry concentration, speed of sound, and density (Workman et al. 1999; Greenwood et al. 1998). When frequency content is evaluated, ultrasound can also be used to determine changes in particle size distribution (Bamberger, Kytomaa, and Greenwood 1998). These techniques have been further developed to provide real-time *in situ* interrogation of slurry mixing in tanks using immersion transducers and non-invasive characterization of fluids and slurries by placing the transducers on the outside of the pipeline spool piece (Bamberger and Greenwood 2004a, b).

9.1.3.1 Characterizing Slurries

Slurry properties for characterizing mixing include mixture density (ρ_m), mass fraction (C_m) or volume fraction (C_v), particle size (d) and the bulk density of the solid (ρ_p). The mass of the slurry (M_m) is equal to the mass of fluid (M_f) plus the mass of the particulate (M_p). The volume of the slurry (V_m) is equal to the volume of fluid (V_f) plus the volume of the particulate (V_p). The mass fraction of the slurry is determined by the ratio

$$C_m = M_p / (M_p + M_f) = \rho_p (\rho_m - \rho_f) / [\rho_m (\rho_p - \rho_f)] \quad (9.1)$$

where ρ_f is the fluid density. The corresponding volume fraction relationship is

$$C_v = C_m / [C_m + S(1 - C_m)] \quad (9.2)$$

where S is the solids relative density (ρ_p / ρ_f). The volume fraction is proportional to the number of particles per unit volume (n). Suppose there are N particles in the total volume (V_T), and each particle occupies a given volume (V_p). The volume fraction is given by

$$C_v = N V_p / V_T = n V_p \quad (9.3)$$

9.1.3.2 Attenuation-Based Measurement of Concentration

When ultrasound passes through a slurry, the signal strength is reduced by the interaction of the ultrasound with the particles in the slurry. This ultrasonic signal attenuation can be analyzed to provide real-time *in situ* measurement of slurry concentration and particle size distribution (Bamberger, Greenwood, and Kytomaa 1998). A simple application of this technique using a single transmitter-receiver pair was demonstrated to track concentration in a vessel during mixing. Before deploying the sensor, the sensor attenuation versus volume fraction response was calibrated using known slurry concentrations to permit interpretation of the on-line attenuation measurements (Greenwood et al. 1993). The attenuation of ultrasound is defined as

$$\alpha = (-1/L) \ln (P/P_0) \quad (9.4)$$

where P_0 is the initial pressure, and P is the pressure after traveling a distance, L . Pressure is proportional to the voltage measured by the transducer and can be written

$$\alpha = (-1/L) \ln (V/V_0) \quad (9.5)$$

or at a given frequency (f), data show that $\ln(V/V_0)$ depends linearly upon the volume fraction (C_v) and that attenuation (α) is proportional to the frequency and to the volume fraction.

$$\alpha = c C_v f \quad (9.6)$$

9.1.3.3 Equipment

To characterize the submerged ROB, transducers that were characterized during the mixing study (Bamberger and Greenwood 2004b) were combined with a computer-controlled ultrasonic pulser and data acquisition system (DAS) (Bamberger, Greenwood, and Witwer 2001) to provide real-time, *in situ* interrogation during sparger operation.

Sensor

The ultrasonic sensor consisted of two parallel and coaxial transducers (a transmitter and receiver separated by 10.2 cm) and is shown in Figure 9.1. The sensor was suspended in the slurry with the transducer faces parallel with the vertical axis so that the fluid could rise between the transducers without depositing on the transducer face. The 2.54-cm-diameter transducers have a center frequency of 2.25 MHz and a bandwidth of 60% at 6 dB. The transmitter functioned by sending a swept frequency pulse (0.1 to 3 MHz) through the slurry to the receiver. A peak detector captured the amplitude of the received signal.

This measurement technique was used to characterize the slurry in the cone-bottom tank as a function of radial position where the radius r is a function of x —perpendicular to the tank bridge—and y —parallel to the tank bridge—and z elevation above the sparge tube outlet (zero datum). The sensor was suspended

in the tank on a rod. A traversing table was used to determine the x and y locations, and a marked rod was used to determine the z locations.



Figure 9.1. Ultrasonic Sensor

Computer Controlled Data Acquisition System

The ultrasonic sensor was operated and controlled by a personal computer (PC) with a single ultrasonic testing (UT) data acquisition card that is a custom Pacific Northwest National Laboratory (PNNL) design. This control architecture, shown in Figure 9.2, contains an ultrasonic pulser, receiver, a high-speed, high-resolution digitizer, and a multiplexer. The board was controlled with PNNL custom software that an operator uses via a graphical user interface (GUI). All raw and processed data were displayed in real time and were archived on hard disk.

The pulser generates a radio frequency (RF) sinusoidal toneburst with the center frequency and number of cycles set by the operator. The center frequency selected was 2.25 MHz, and the number of cycles in the toneburst ranged from 10 to 15. The ultrasonic receiver provided a gain ranging from 0 to 40 dB that was set by the operator or automatically by using the automatic gain control feature. The digitizer has 12 bits of resolution (1 part in 4096) with a sampling rate up to 40 MHz. The maximum sampling rate of 40 MHz means that a sample is obtained every 25 nanoseconds. The custom-written software consists of five modules: 1) instrument setup, 2) data acquisition and display, 3) parameter measurement, 4) data storage, and 5) density determination. The software, written in "C," operates on a DOS-based platform on a PC and is documented in Bamberger and Greenwood (2001). Averaging is used to factor out random noise. The system finds the peak amplitude and the time of flight for each raw signal, averages the value of each one for the chosen number of signals, and calculates the standard deviation. The maximum and minimum values of the peak are also determined.

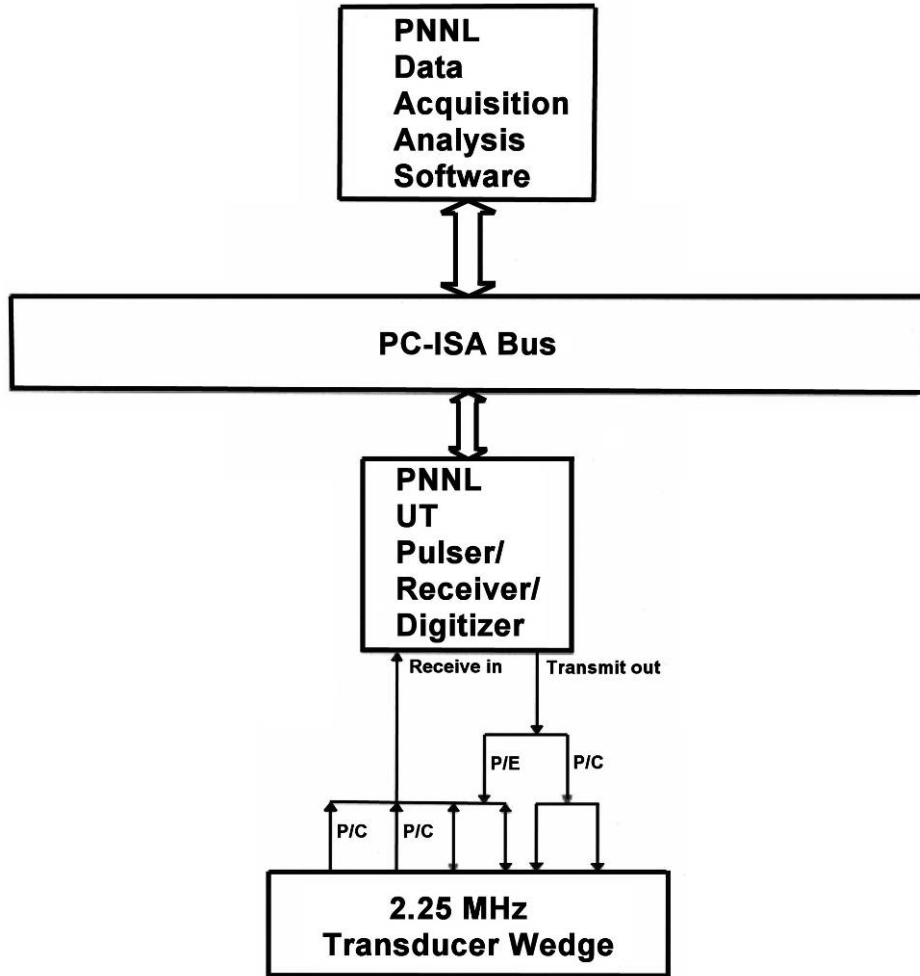


Figure 9.2. Sensor Control System Architecture

For these measurements, the instrument setup consisted of setting parameters for the pulser (frequency and number of cycles), receiver (gain), and digitizer (sample rate and sample delay), either manually or by invoking the automatic gain-control feature. The peak amplitude of the signal waveform, as shown in Figure 9.3, was found by examining the peak-to-peak amplitude within the amplitude measurement gate and selecting the largest value.

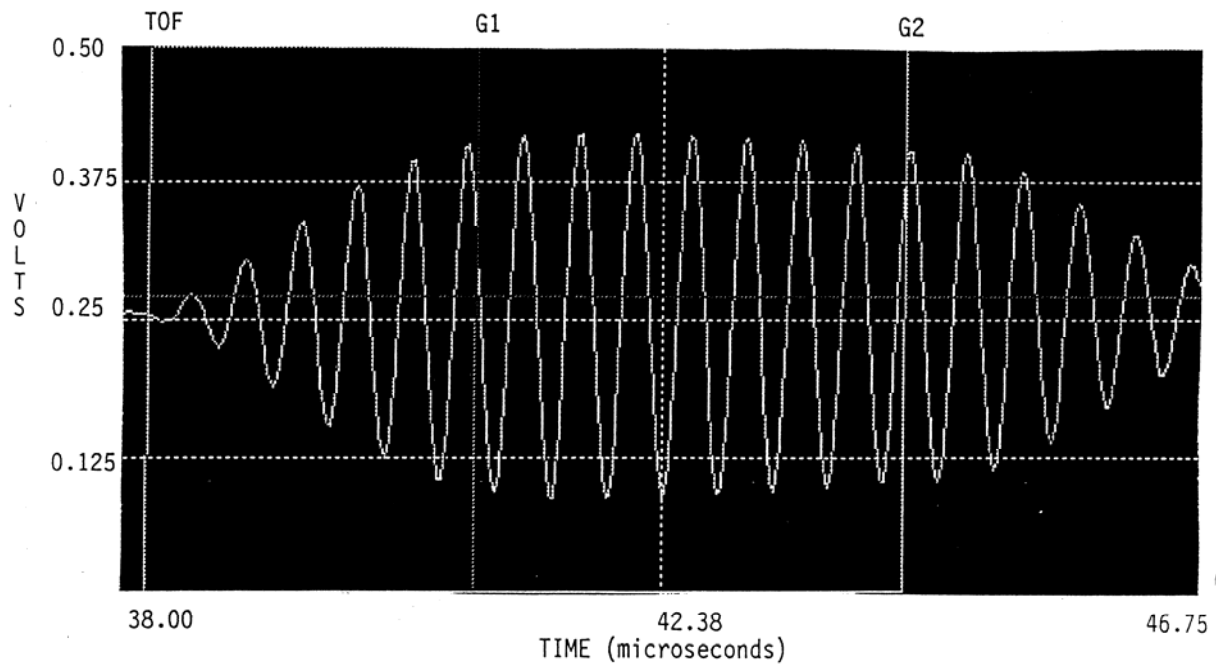


Figure 9.3. Toneburst Signal Appearing on the Computer Monitor

Making a Measurement

To make a measurement, the sensor was inserted into the slurry at the desired location. The signal capture routine was operated for 1 to 2 min. After the signal capture was stopped, the data file was saved using a file name that related to the test conditions as listed in Table 9.1. The ultrasonic data file record included position: x and z coordinates, elevation, and gain. The y coordinate value was constant at 3.625 inches east throughout the measurements.

The ultrasonic probe extended from the mast so that the mast would not affect the measurement. During testing, two lengths of extension were used. The conversion from location indicator to x coordinate for each test is shown in Table 9.2.

Table 9.1. Data File Naming Convention

File Name Format: NEXXDYY				
N	E	XX	D	YY
Nominal Sparger Flow Rate	Elevation Above Sparge Tube. Letter Designator	Probe Locator Designation XX	Probe Direction	Amplifier Gain Setting
ACFM	in.	in.	Letter Indicator	dB
5	A = 100	24 through 66	G: pointed toward tank center	0 to 40
12	B = 83	-	R: reversed, pointed towards tank wall	-
30	C = 66	-	-	-
-	D = 36	-	-	-
-	E = 18	-	-	-
-	F = 0	-	-	-
-	G = -12	-	-	-
-	H = -6	-	-	-
-	I = -3	-	-	-

Table 9.2. X-Coordinate Conversion

Test Date	Probe Direction	X coordinate (in.)	Probe Direction	X coordinate (in.)
2004-03-01	G	x = XX-13.5	R	x = XX+13.5
2004-03-02	G	x = XX-13.5	R	x = XX+13.5
2004-03-03	G	x = XX-20.0	R	x = XX+20.0

9.2 Results and Discussion

Air is a very strong attenuator of ultrasound. To demonstrate the effect of air upon ultrasonic signal, the sensor was placed in a container of water. Using an ~ ¼-in.-diameter hose, air bubbles were blown in the water beneath the sensor. As the bubbles rose through the sampling volume—the space between the transducers—the ultrasonic signal, obtained at a sampling rate of 1.74 ± 0.03 measurements per second, was attenuated significantly, and at times showed an amplitude of zero. The sampling volume was a cylinder with diameter of 2.54 cm and length of 10.2 cm. This capability to change from full-strength signal to zero in the presence of bubbles was used to determine the locations in the slurry where bubbles were present.

One data set is discussed before analyzing the data to show the different types of observations that can be obtained from these amplitude data. This data set is shown in Figure 9.4.

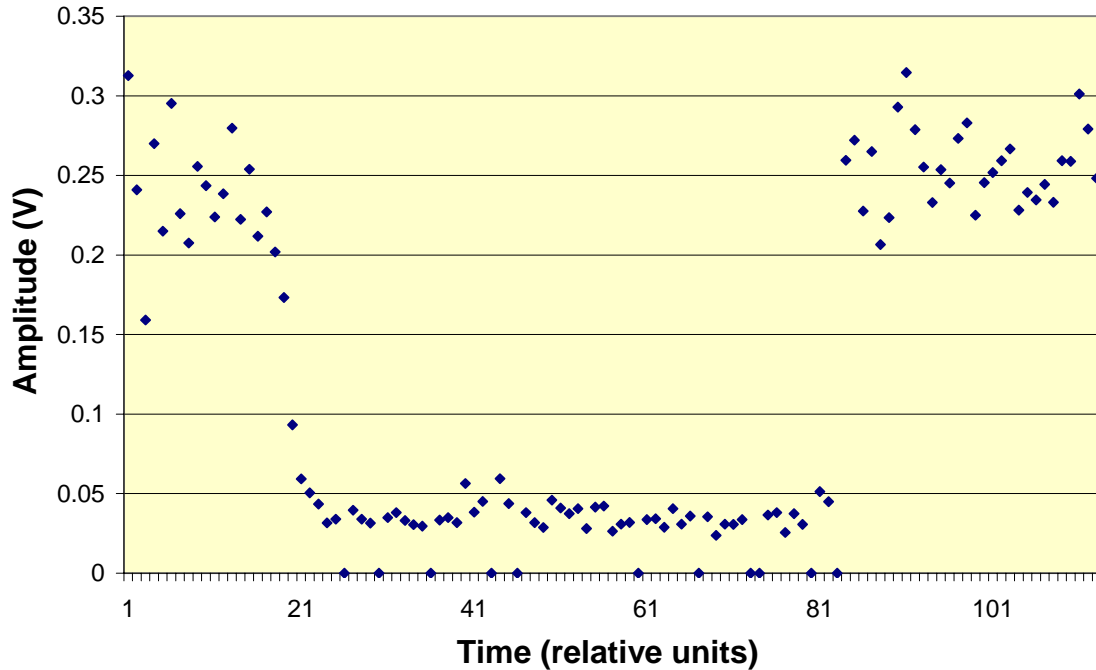


Figure 9.4. Sample Data Set

This data set shows four distinct types of data:

- Type 1) amplitude of zero Volts of duration 1(9 occurrences)
- Type 2) amplitude of zero Volts of duration >1 (1 occurrence of two zeros occurring in sequence observed at point ~75 on the x axis)
- Type 3) a series of data points of quite low amplitude (at ~ 0.04 V amplitude) showing either many small bubbles that do not fully obscure the sample volume or a significantly more attenuative solids fraction
- Type 4) fluid of average bulk properties (in the range of amplitude 0.25 V).

The data sets do not exhibit all of these distinct types of behavior. The majority show Type 4 behavior, the presence of no cases of reduced amplitude signifying no sparger air flow at that sampling location.

9.2.1 Data Sets

The ultrasonic attenuation sensor was operated in the cone-bottom tank on three consecutive days. A summary of the data taken is listed in Table 9.3. The extent of measurements is plotted in Figure 9.5 through Figure 9.9 with each symbol showing a measurement location. The majority of data were taken in the central region of the tank parallel to the line from the center (C) to B3 as marked in Figure 5.6. The Y coordinate was located 3.625 in. to the east of the line between C and B3. By rotating the probe 180 deg so that the sensor faced out rather than in, some data points were taken near the tank wall. No measurements were taken in the gap between these regions.

Table 9.3. Submerged ROB Measurement Positions

Date	Nominal Flow Rate (ACFM)	Z position Elevation with Respect to Sparger Tube Outlet (in.)	X Position Range (South) (in.)	Y-Position (East) (in.)
2004-03-01	0	66, 83, 100	11	3.625
	12	66, 83, 100	8.5 to 63.5	3.625
2004-03-02	12	-12, -6, 0, 18, 36	9.5 to 55.5	3.625
	30	-12, -6, -3, 0, 18, 36, 66, 83, 100	9.5 to 63.5	3.625
2004-03-03	30	-12, -6, -3, 0, 18, 36, 66, 83, 100	3 to 69	3.625
2004-03-03	5	-12, -6, -3, 0, 18, 36, 66, 83, 100	3 to 69	3.625

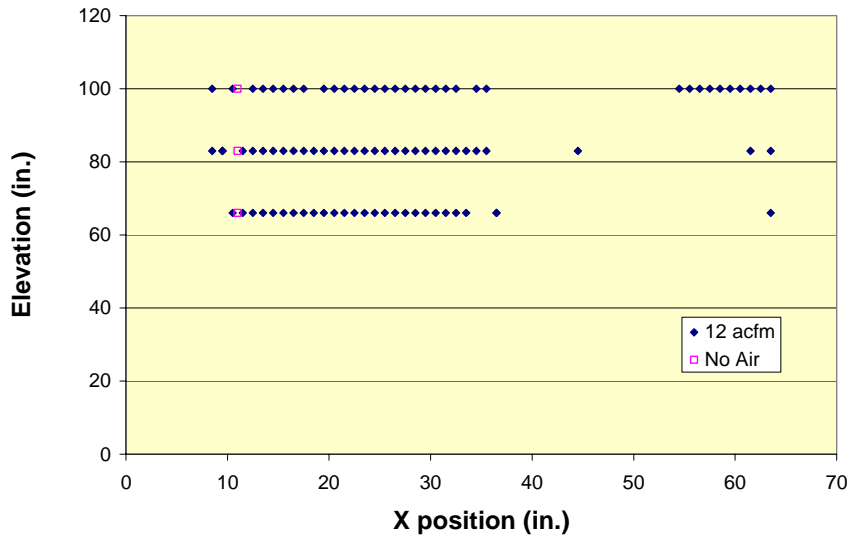


Figure 9.5. Sensor Locations Evaluated 2004-03-01 at Nominal 12 ACFM

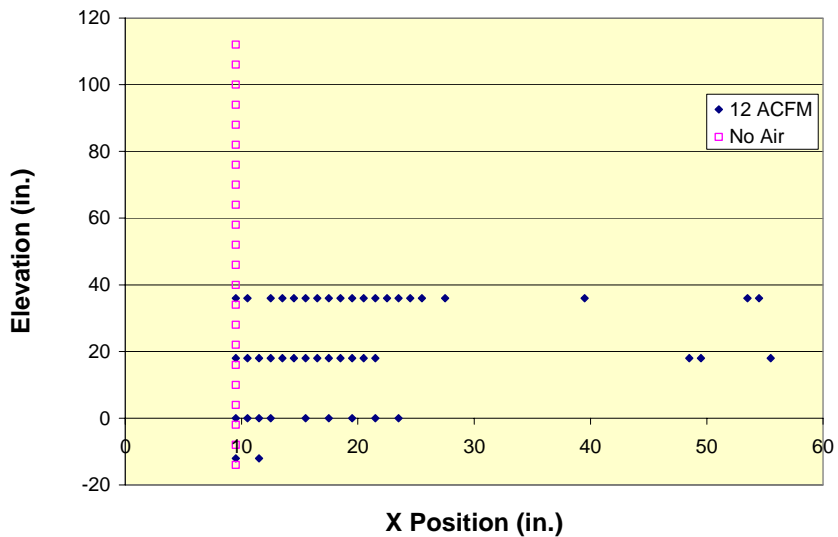


Figure 9.6. Sensor Locations Evaluated 2004-03-02 at Nominal 12 ACFM

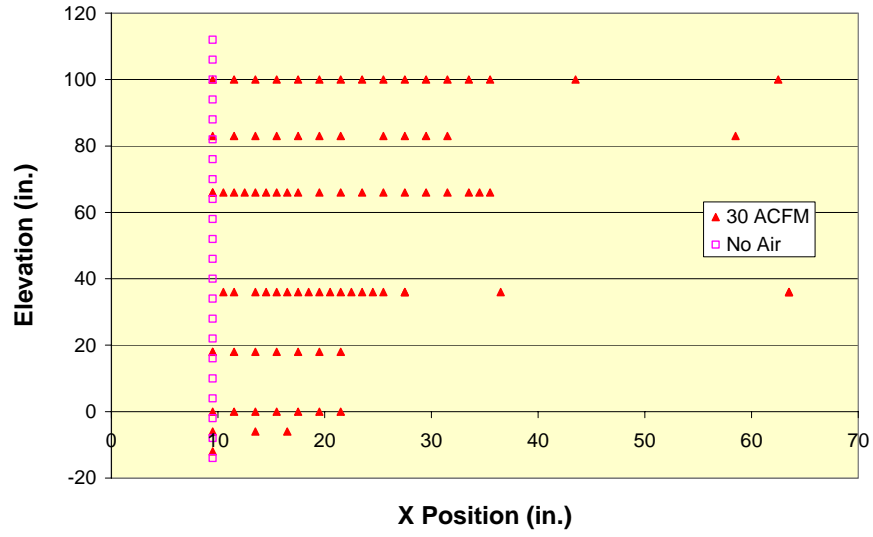


Figure 9.7. Sensor Locations Evaluated 2004-03-02 at Nominal 30 ACFM

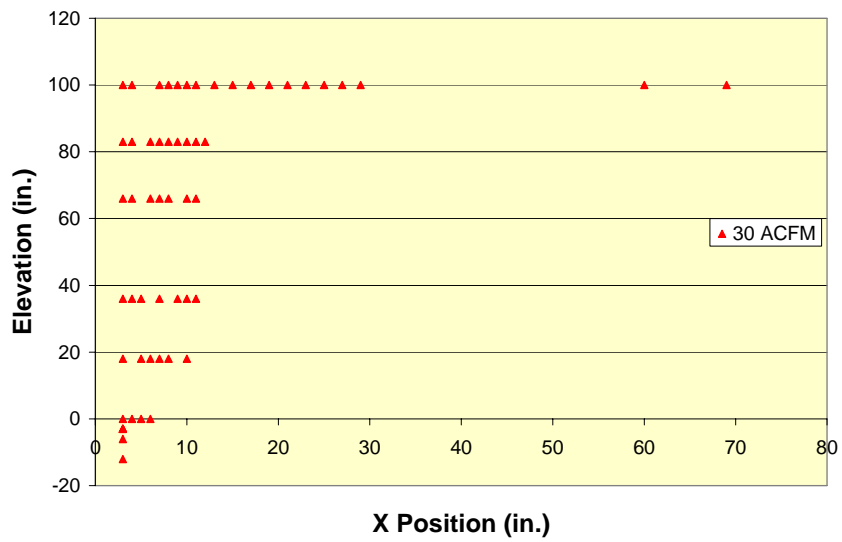


Figure 9.8. Sensor Locations Evaluated 2004-03-03 at Nominal 30 ACFM

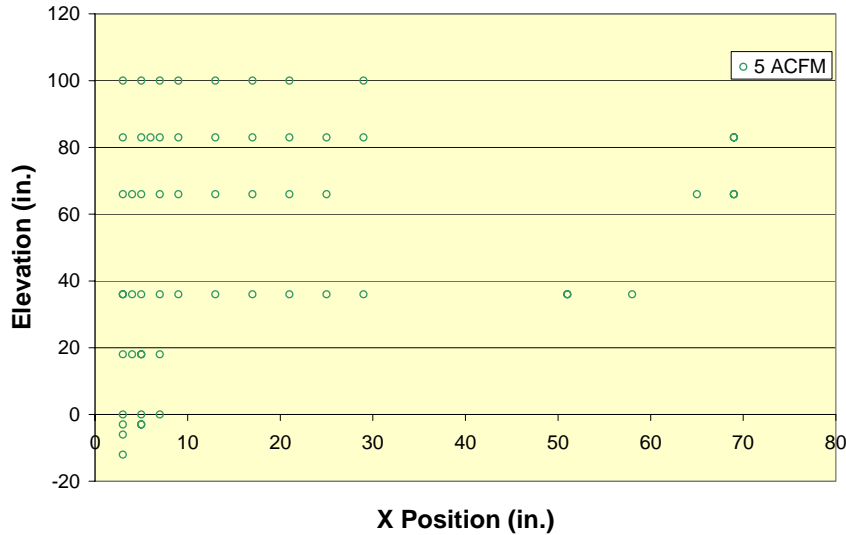


Figure 9.9. Sensor Locations Evaluated 2004-03-03 at Nominal 5 ACFM

9.2.2 Measurements at Nominal 30 ACFM

Data at a nominal 30 ACFM sparger air flow were taken over a period of two days using probes with two different extension lengths. Some of the data locations overlapped. The probe with the longer extension was able to measure within 3 in. of the sparger tube. The data are plotted in three ways: 1) showing occurrences of all amplitude values <0.2 of the maximum amplitude, 2) showing occurrences of all amplitude values <0.01 of the maximum amplitude value (essentially zero signal penetration through the probe), and 3) showing the “duration” of the zero value signal. In this third case, no signal was observed for up to 18 sequential measurement cycles, so the duration was 18. The ultrasonic interrogation rate was 1.76 ± 0.02 measurements per sec, so a duration of 18 is a bubble or series of bubbles that attenuate the signal for 10 sec.

9.2.2.1 Amplitudes <0.2 V Max

The selection of tallying all data with an amplitude <0.2 of maximum voltage was chosen because when the signal strength is reduced to only 20% of the original value, the presence of air or bubbles is the expected cause. The data showing the number of occurrences of reduced amplitude per location is plotted in Figure 9.10 and show data taken at 6 elevations at or above the sparge tube outlet: 0, 18, 36, 66, 83, and 100 in, and 2 elevations below the sparge tube outlet: -6, and -12 in. The data for the first day of testing, when a shorter probe extension was used, is plotted beneath the data obtained on day two when a longer probe extension was used. The zero data are color coded with purple shown as no incidences of reduced amplitude observed and red with ≥ 64 zeros observed. Locations where amplitude counts that differ from data obtained with the voltage level threshold set as <0.01 V max are shown outlined in black. The data in Figure 9.10 show that the majority of the bubbles rose near the sparge tube with sporadic bubbles observed as far out as 34 in. from the sparge tube.

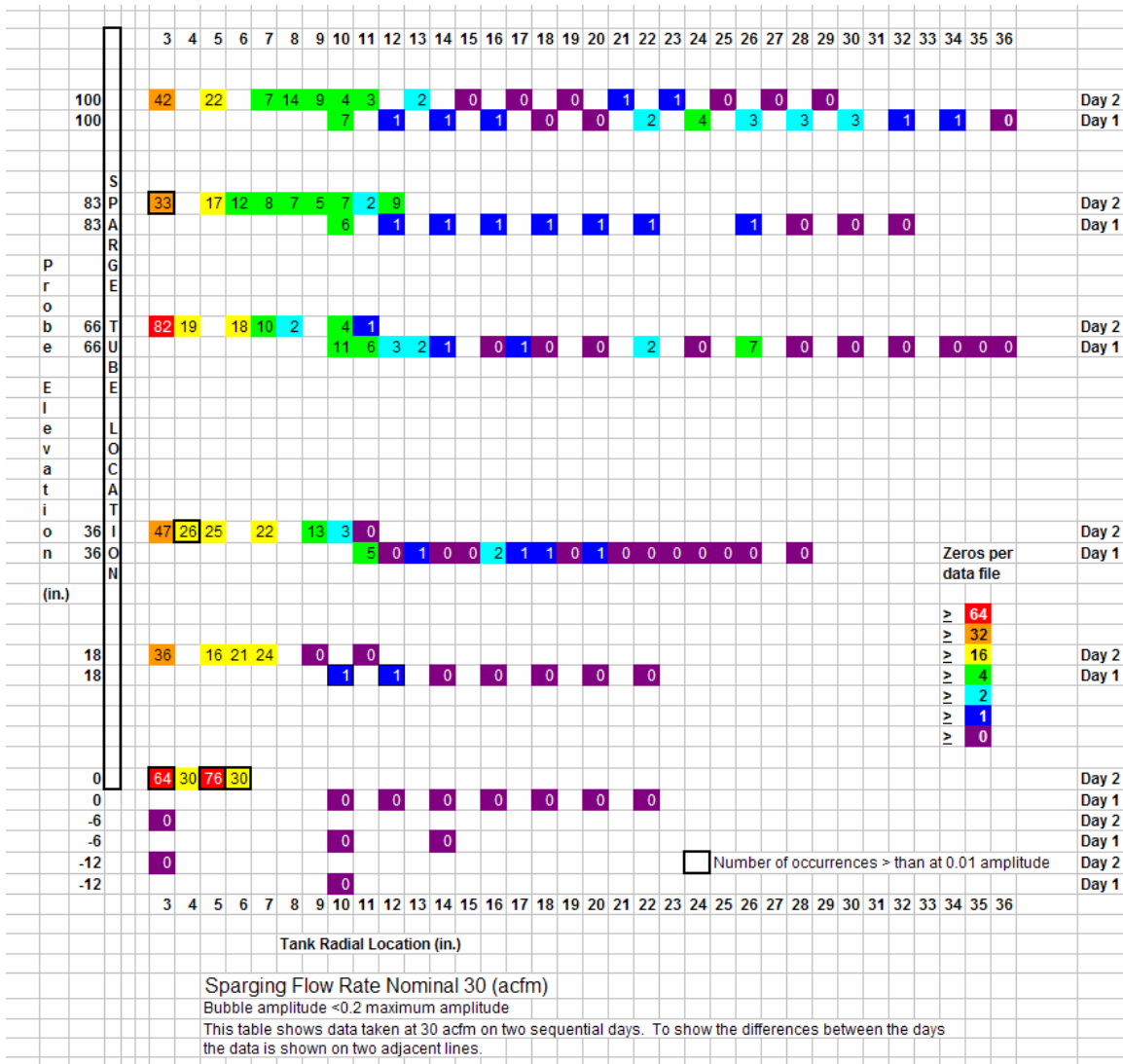


Figure 9.10. Plot of 30 ACFM Locations with Amplitude <0.2 V Max for Two Sequential Days of Testing

9.2.2.2 Amplitudes <0.01 V max

These data shown in Figure 9.11 are very similar to that shown in Figure 9.10. At the zero elevation, and near the sparge tube, some zero counts have decreased.

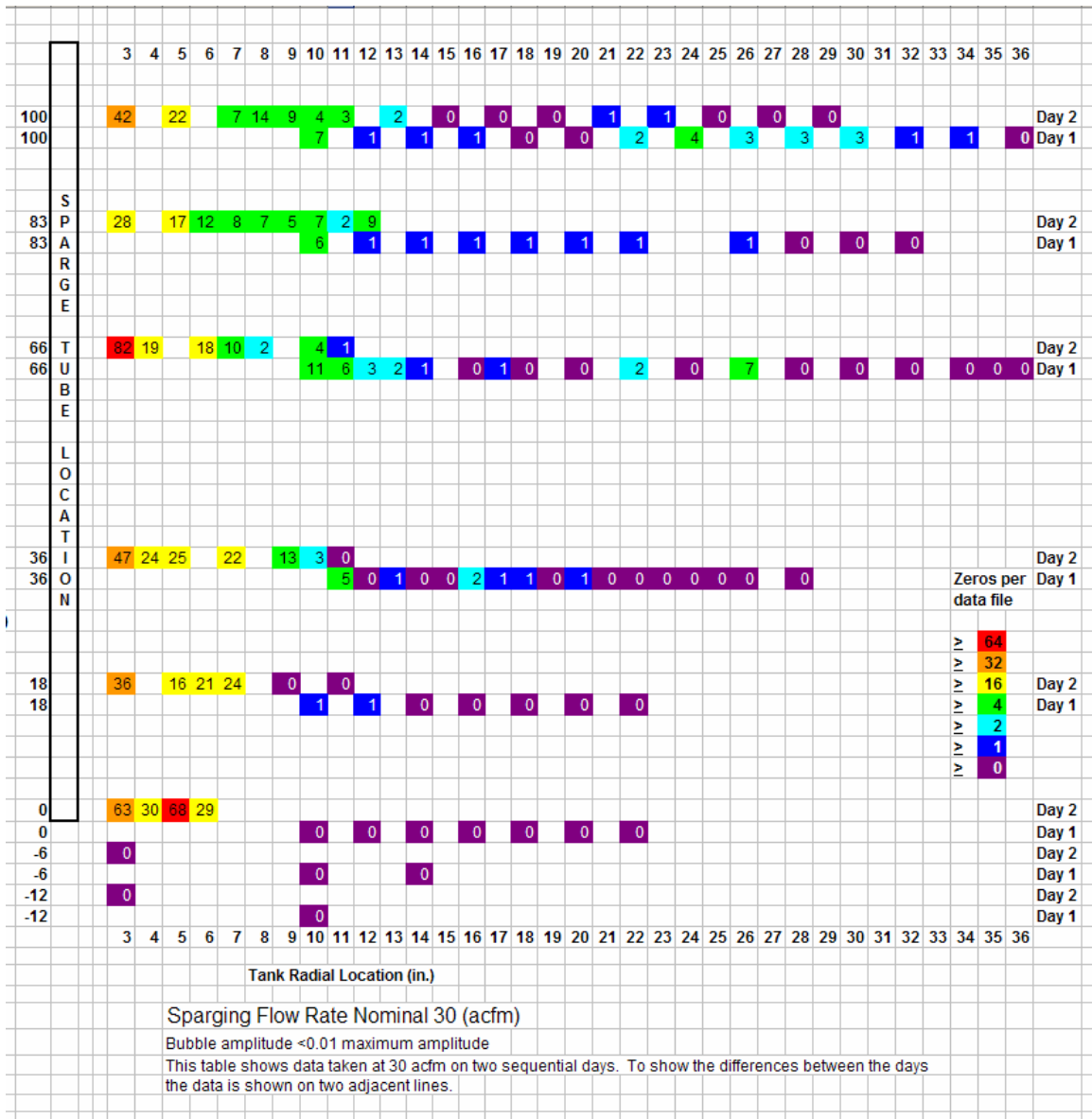


Figure 9.11. Plot of 30 ACFM Locations with Amplitude <0.01 V Max for Two Sequential Days of Testing

9.2.2.3 Duration of Zero Voltage Measurements

To visualize the duration of the zero voltage measurements, the data in Figure 9.12 was replotted to show the duration (shown as the number of consecutive zero observations) of each zero measurement. These sequences could be viewed as 1) either a very large bubble, or 2) a series of sequential bubbles moving faster than the sample measurement time of 1.76 measurements per second. The number of occurrences of each duration bubble is shown by the number inside the color coded box. The box color signifies the length of the sequential zero; the columns are outlined when some of the durations were not observed. For example, on Day 2 at a sparger elevation of 18 in. at a radial location of 3 in., 11 occurrences of duration 1, 6 occurrences of duration 2, 3 occurrences of duration 3, and 1 occurrence

of duration 4 were observed during the measurement. In the figure, from 1 to 18 sequential zero readings were observed. The sequential zeros form the shape of an expanding cone with radius ranging from 6 in. at the exit of the sparge tube and expanding to 12 in. at a level of 83 in. above the sparge tube.

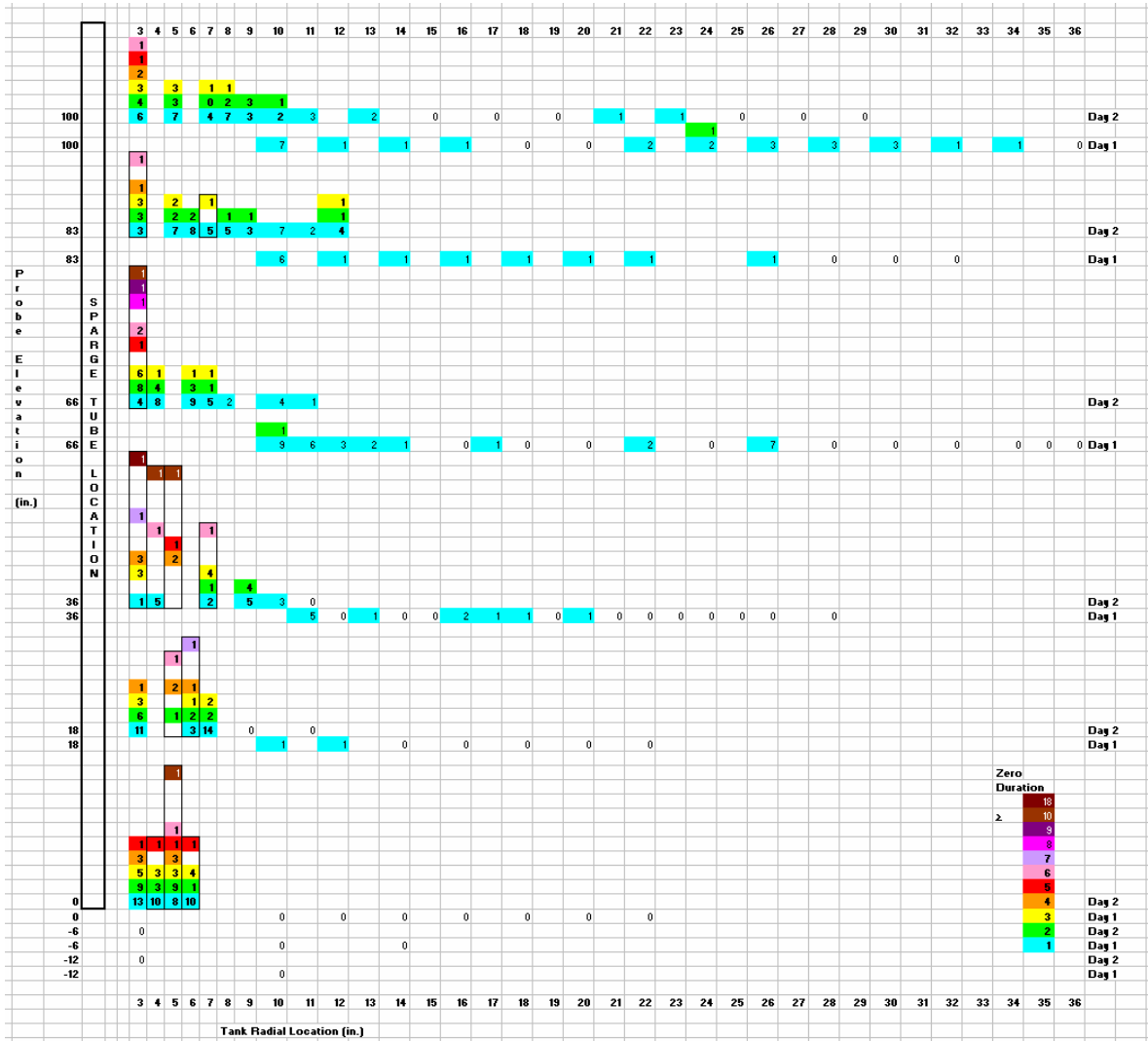


Figure 9.12. Plot of Bubble Duration at 30 ACFM for Locations with Amplitude <0.01 V max for Two Sequential Days of Testing

9.2.3 30 ACFM Data Synopsis

The data obtained at a nominal 30 ACFM show 1) a central core of bubbles observed to a radius of ~ 8 in. In this area the bubble duration is greater than one measurement cycle and multiple occurrences of zero amplitude are observed in this core region. Single bubbles are observed more sporadically out to radii that expand with increasing elevation above the sparge tube outlet. The sequential zeros form the shape of an expanding cone with radius ranging from 6 in. at the exit of the sparge tube and expanding to 12 in. at a level of 83 in. above the sparge tube.

9.2.4 Measurements at Nominal 12 ACFM

Measurements taken at a nominal 12 ACFM sparger air flow were taken over a period of two days using probes with the shorter extension. The radii interrogated started at 9 in. from the sparge tube. Some of the data locations overlapped. The data is plotted in two ways: 1) showing occurrences of all amplitude values <0.01 of the maximum amplitude value (essentially zero signal penetration through the probe), and 3) showing the “duration” of the zero value signal. The ultrasonic interrogation rate was 1.76 ± 0.02 measurements per sec.

9.2.4.1 Amplitudes <0.01 V Max

The 12 ACFM data showing locations of zero amplitude signals are plotted in Figure 9.13 and show data taken at 6 elevations at or above the sparge tube outlet: 0, 18, 36, 66, 83, and 100 in, and 1 elevation below the sparge tube outlet: -12 in. The reduced amplitude data at each location is color coded with purple shown as no zeros observed and red with ≥ 64 zeros observed. The data plotted in Figure 9.13 show that only a few bubbles rose in the range of 10 to 14 in. from the sparge tube. No measurements were made closer than 9 in. Squares with no number indicate that no measurements were made at that location. The number of bubbles observed at a nominal sparger flow rate of 12 ACFM is much reduced from that observed at a nominal sparger flow rate of 30 ACFM.

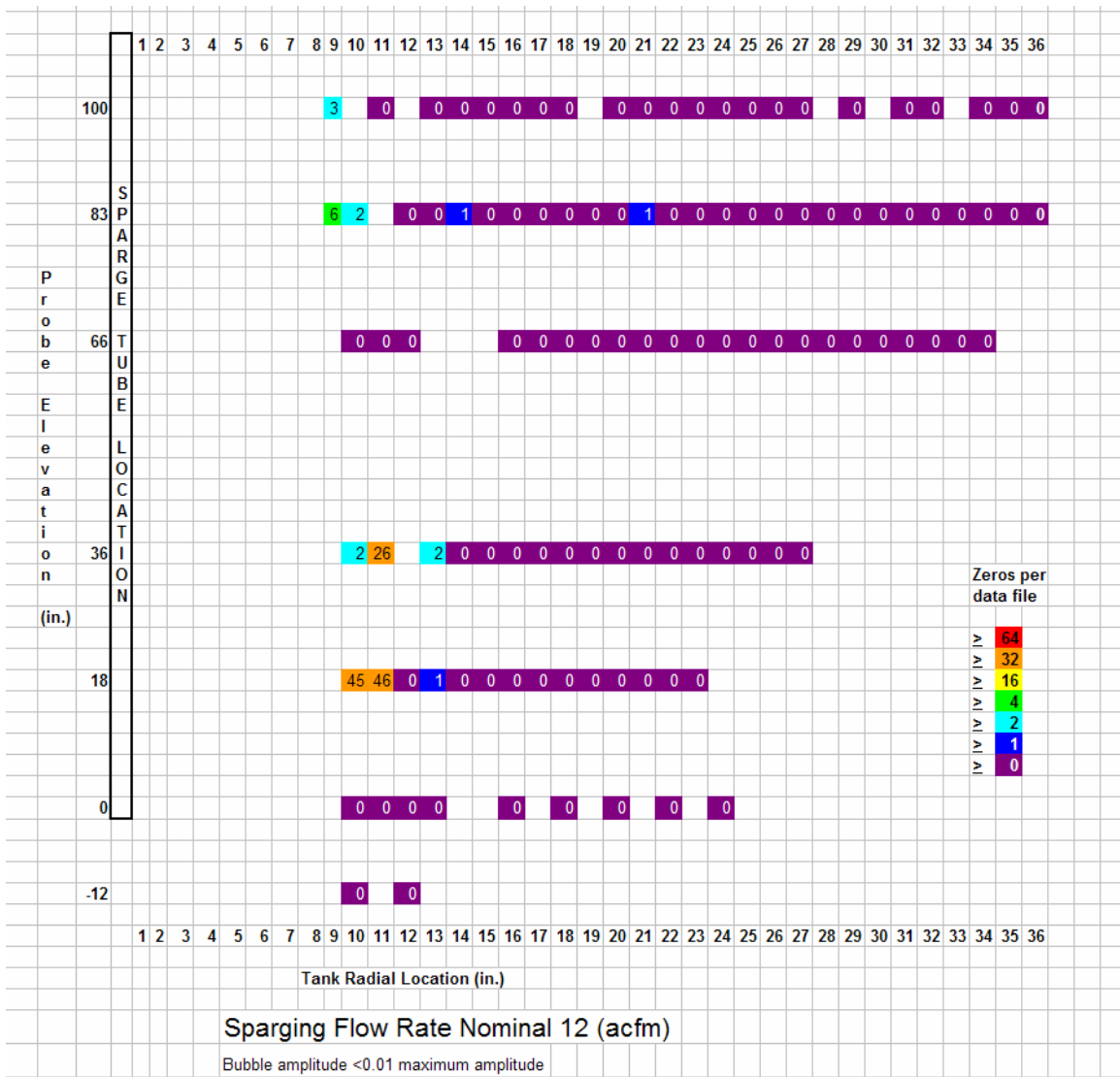


Figure 9.13. Plot of 12 ACFM Locations with Amplitude <0.01 V Max

9.2.4.2 Duration of Zero Voltage Measurements

To visualize the duration of the zero voltage measurements, the data in Figure 9.13 was replotted to show the duration (shown as the number of consecutive zeros) of each zero measurement (see Figure 9.14). This could be viewed as 1) either a very large bubble, or 2) a series of sequential bubbles moving faster than the sample measurement time of 1.76 measurements per second. The number of occurrences of each duration bubble is shown by the number inside the color coded box. The box color signifies the length of the sequential zero; the columns are outlined when some of the durations were not observed. At this flow rate, from 1 to 4 sequential zero readings were observed. The sequential zeros were observed at a radius of 9 to 13 in. at an elevation from 18 to 36 in. above the sparge tube. As the bubbles rise, the radius diminishes slightly with sporadic bubbles being observed in the range from 14 to 21 in.

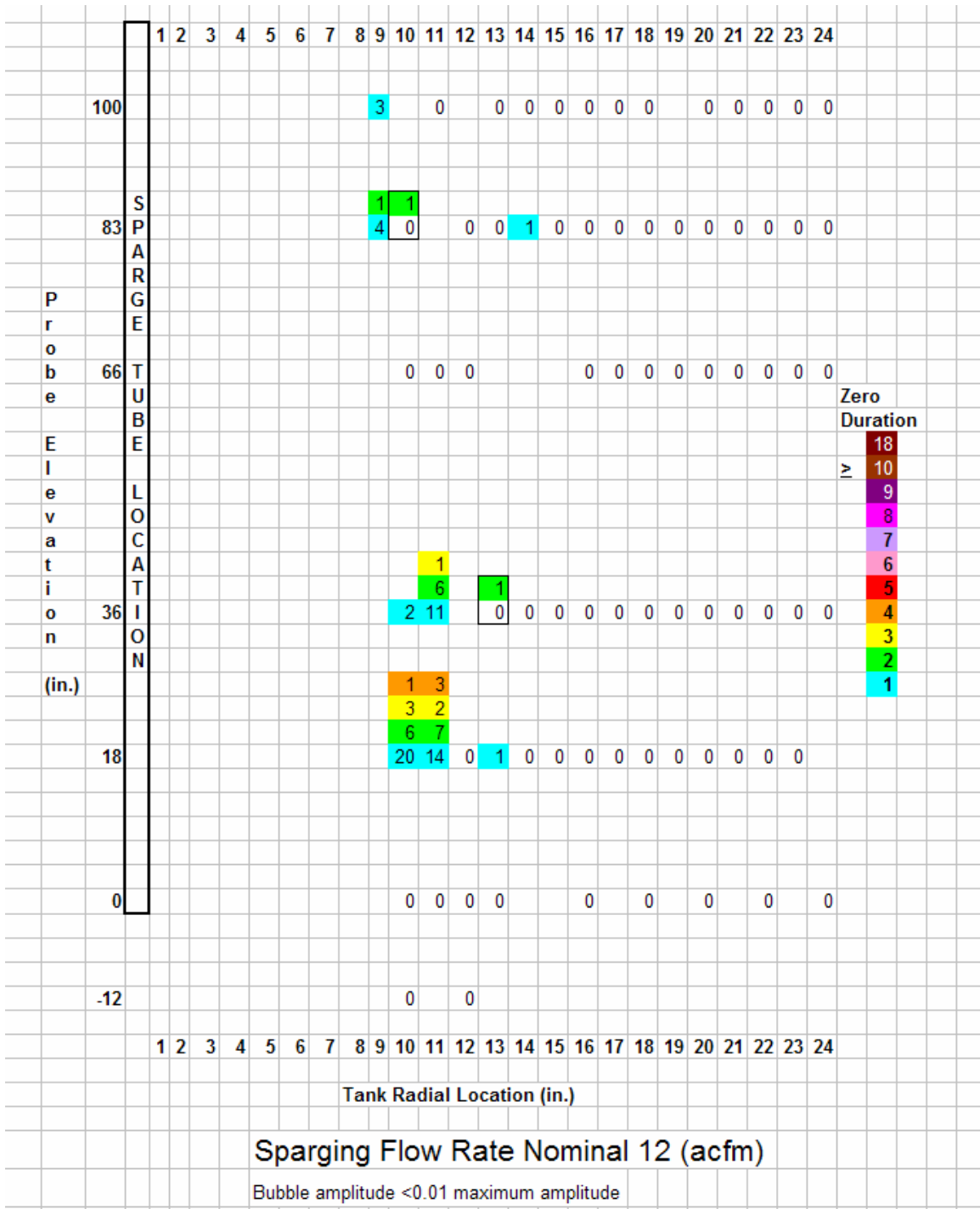


Figure 9.14. Plot of Bubble Duration at 12 ACFM for Locations with Amplitude <0.01 V Max

9.2.5 Measurements at Nominal 5 ACFM

Measurements were taken at a nominal 5 ACFM sparger air flow using the probes with the longer extension. The radii interrogated started at 3 in. from the sparge tube. Some of the data locations

overlapped. Not very many bubbles were interrogated ultrasonically at this low flow rate, so the data is only plotted showing occurrences of all amplitude values <0.01 of the maximum amplitude value (essentially zero signal penetration through the probe). The ultrasonic interrogation rate was 1.76 ± 0.02 measurements per sec.

9.2.5.1 Amplitudes <0.01 V Max

The 5 ACFM data showing locations of reduced signal amplitude are plotted in Figure 9.15 and shows data taken at 6 elevations at or above the sparge tube outlet: 0, 18, 36, 66, 83, and 100 in, and 3 elevations below the sparge tube outlet: -3, -6 and -12 in. The zero data at each location is color coded with purple shown as no zeros observed. Air was observed only at three locations. Squares with no number indicate that no measurements were made at that location. Because of the lack of locations with observed reduced amplitude, no duration data were plotted. Bubbles were observed visually at the top of the tank during these measurements; however, either their path was somewhere other than the ultrasonic probe, or their size was not large enough to reduce the signal to less than 0.2 of the maximum observed voltage observed at each location.

9.3 Summary of Ultrasonic Subsurface Observations

The ultrasonic sensor was able to identify 1) the presence and 2) duration of signal amplitude reduction that can be attributed to the presence of air or bubbles within the sensor transducers. Because the sensor was moved from location to location throughout the measurement process, one is not able to track the rise of an individual bubble through the slurry. Each of the measurements is considered to be distinct from other measurements. However, over the 1 to 2 min measurement period 100 to 200 data points were obtained at each location and that enabled observations of multiple occurrences of low signal amplitude attributable to bubbles. To permit some comparison between the three flow rates, the outer region of single and multiple duration low amplitude events are plotted in Figure 9.16. This plot takes key regions from the previous figures and shows them on a single plot. The trace shows the limited extent of the 5 ACFM flow, the broader range of the 12 ACFM flow rate and the two regions, inner core and outer bound for the 30 ACFM flow rate. The data points indicate that the bubbles may not rise straight up, but may curve in towards the tank center. At 30 ACFM sporadic bubbles were observed to rise outward toward the tank walls.

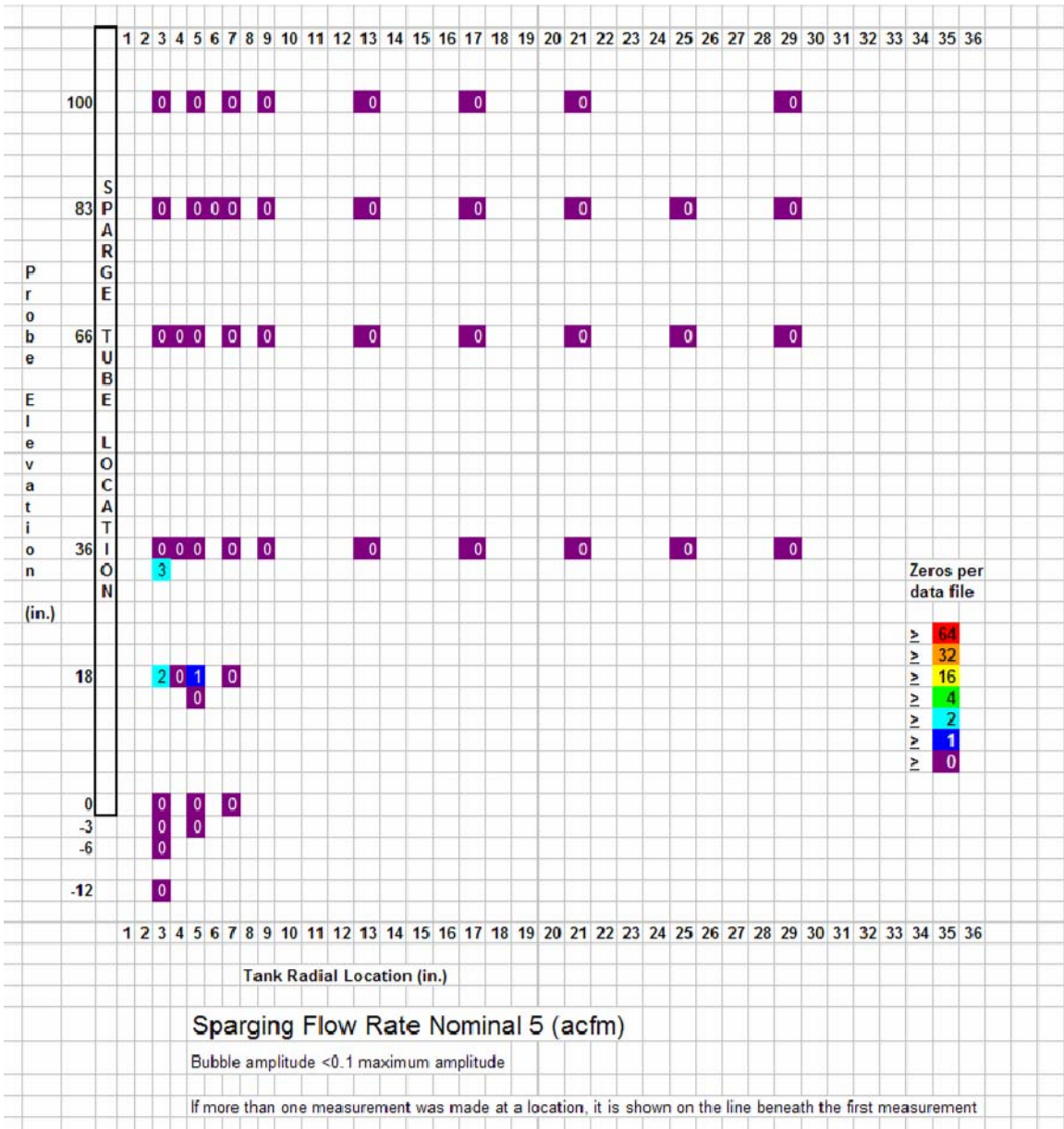


Figure 9.15. Plot of 5 ACFM Locations with Amplitude <math>< 0.01</math> V max Equal to those Observed at <math>< 0.2</math> V Max

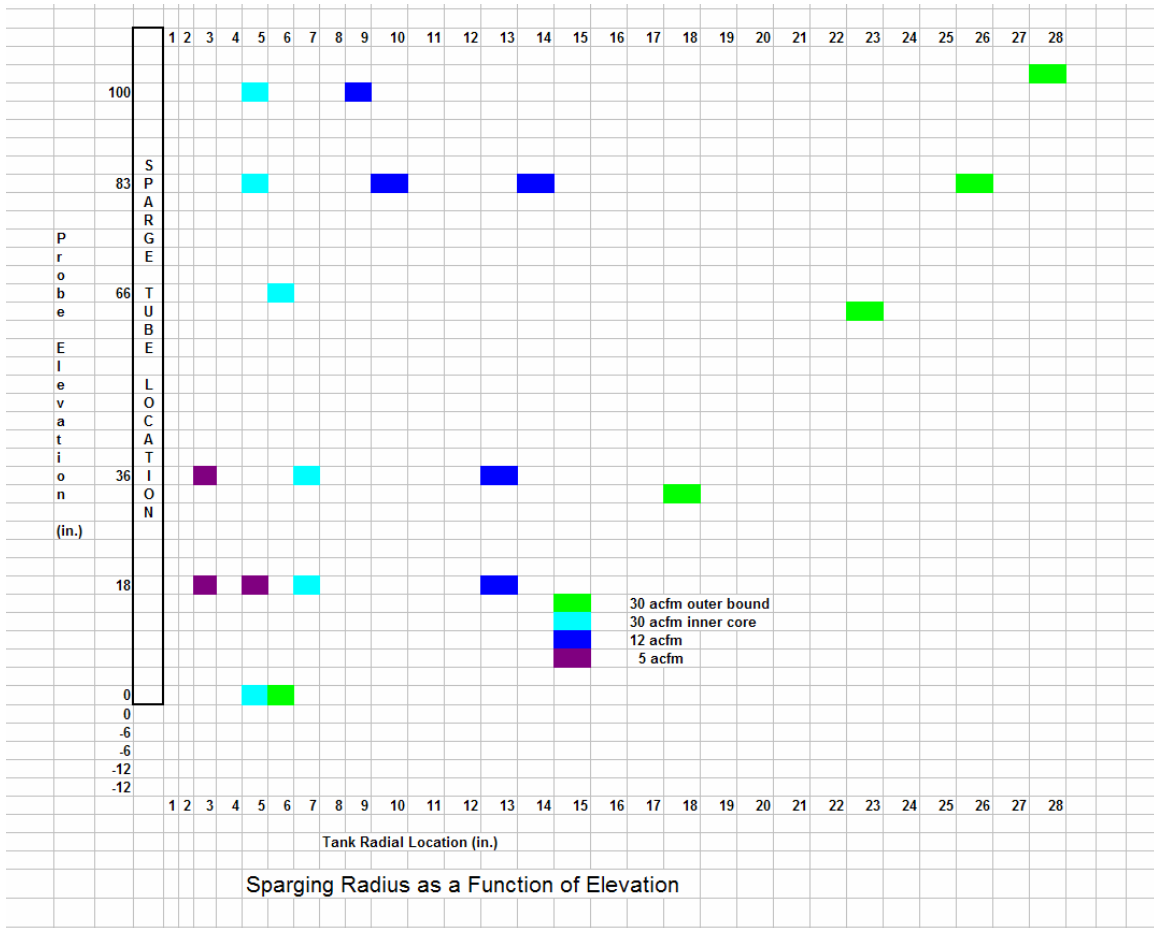


Figure 9.16. Plot of Sparging Bubble Radius as a Function of Elevation for the Three Sparger Flow Rates of 5, 12, and 30 ACFM

10.0 ROB and ZOI Circulation Time

The objective of these tests was to determine the slurry circulation time and provide a plot of circulation time through a single cycle of a clump of fluid as a function of air-flow rate. Experiments were conducted at air-flow rates of 5 and $40 \pm 10\%$ ACFM. A chemical tracer detection system(s) was used to monitor the concentration of the tracer. The dye tracer was injected in the ROB near the bottom of the sparge tube. The chemical tracer detectors were placed at locations suitable for determining the circulation time.

10.1 Materials and Methods

10.1.1 Apparatus

The single tube sparging test stand described in Section 5.1 was used for these tests.

10.1.2 Simulant

The kaolin/bentonite simulant described in Section 5.2 was used in these tests.

10.1.3 Methods Used

These tests were carried out with a single sparger nozzle 120 inches below the liquid surface and 24 inches above the tank bottom. Test runs were made at sparger air-flow rates of 15 and 40 ACFM (nominal).

A video recording camera was positioned overlooking the tank surface. The dye tracer part of the test was performed by positioning dye via an injection tube at about $\frac{1}{2}$ inch radially from the sparger nozzle and about 3 inches above the nozzle. The tank was quiescent during this procedure. Video recording was started, and the valve upstream of the sparger nozzle was opened.

The electrolyte tracer tests were carried out with the sparger operating and steady-state ZOI verified. The subsurface chloride ion specific electrodes (ISEs) were propositioned as follows:

15 ACFM

ISE A 60 inches below surface; 24 inches from sparger tube

ISE B 116 inches below surface; 18 inches from sparger tube

40 ACFM

ISE A 60 inches below surface; 32 inches from sparger tube

ISE B 116 inches below surface; 18 inches from sparger tube

The electrolyte tracer (sodium chloride water solution) was added to the slurry surface at a distance of 24 inches from the sparger nozzle for the 15 ACFM test and 32 inches for the 40 ACFM test. These tracer addition and measurement positions are shown in Figure 10.1.

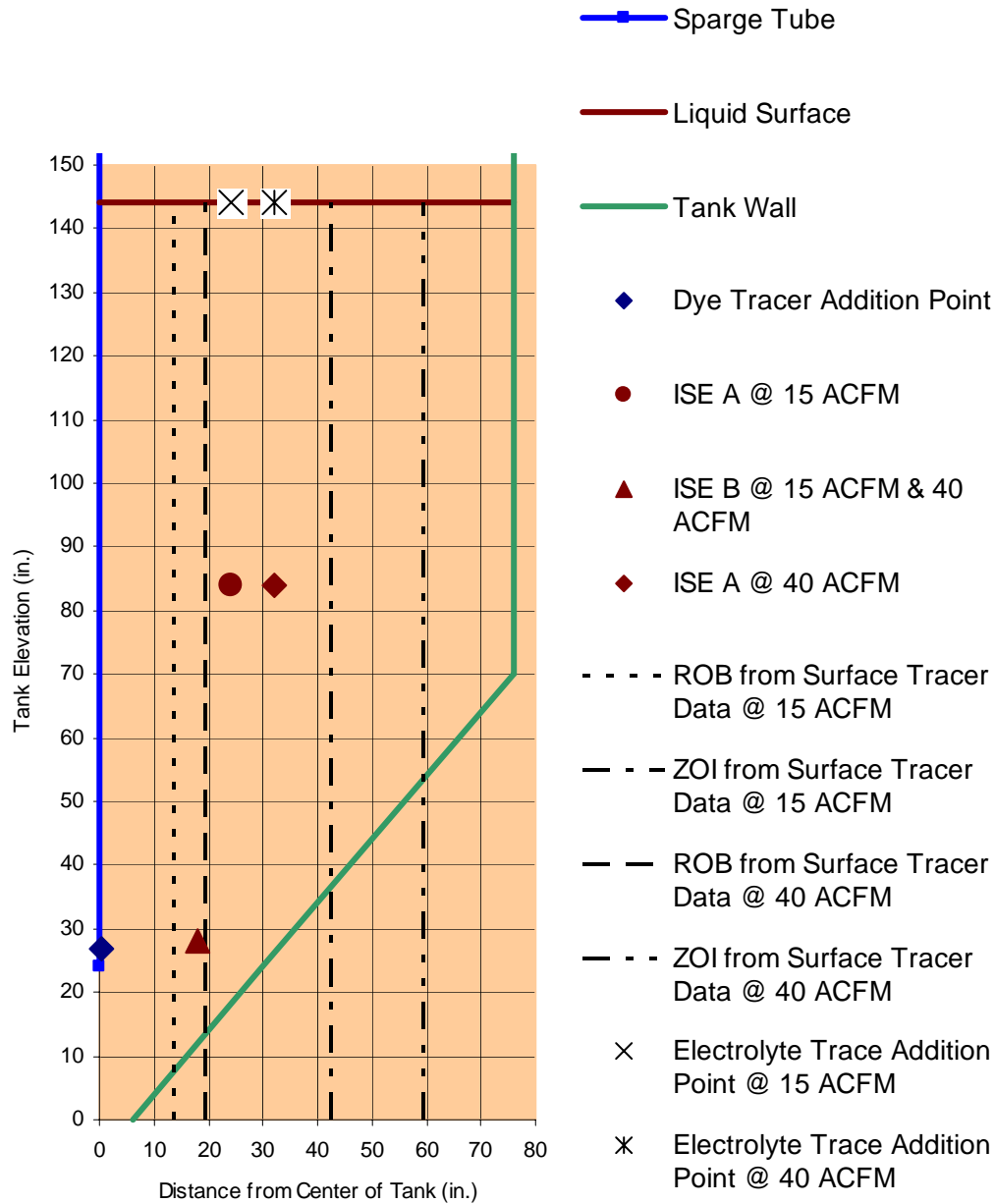


Figure 10.1. Schematic of Significant Locations for Sparging Tracer Test

The electrical potential (representing the relative concentration of the chloride ion) for each ISE was measured and recorded every 30 seconds.

10.2 Results and Discussion

The purpose of this test was to estimate the circulation time that a parcel of fluid circulated through the sparging flow patterns. This flow pattern can be broken into four major portions: 1) upflow due to the bubbles in the ROB, 2) radial outward flow on the surface region in the transition from the ROB to ZOI, 3) downward flow in the ZOI, and 4) transition of ZOI back to the ROB. Circulation times for each of these sections can be estimated by the combination of optical tracer and electrolyte tracer tests. However,

the mechanics of mixing and transport in the sparging system must be understood in the microscale level to interpret the results.

In these tests, an impulse of tracer was injected into the system. For these viscous, non-Newtonian systems, molecular diffusion is typically small and can be neglected compared to convective processes. Spatial and dynamic differences in velocity in the system will create varying paths between two points in the system. These paths will have varying velocities and degrees of micromixing. This results in different tracer molecules having varying residence times in the system that results in the output from the system having a characteristic distribution (i.e., a residence time distribution). These concepts are shown graphically in Figure 10.2.

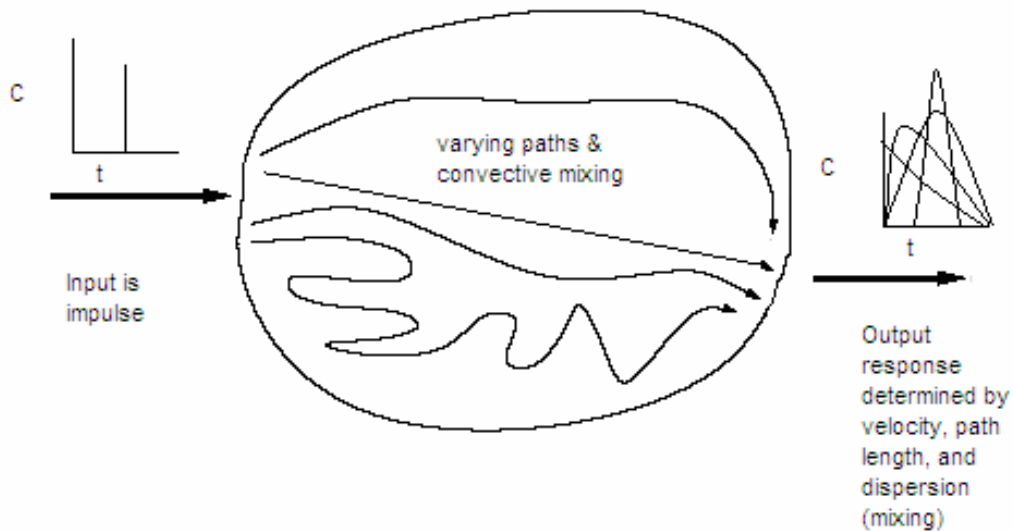


Figure 10.2. Tracer Testing Concepts

For circulation time calculations, calculations are performed based upon a specific path length between tracer addition and observation points. For this reason, the times at which the tracer is first observable will likely follow the shortest path between addition and observation points and will be used for average fluid velocities in each region. The peak on the residence time distribution corresponds to the average time that a fluid parcel reaches a particular point. For this reason, these times will be used to estimate the circulation times of a parcel of fluid when varying path lengths are accounted

The dye tracer part of the test was performed by positioning dye via an injection tube at about ½ inch radially from the sparger nozzle and about 3 inches above the nozzle. The tank was quiescent during dye injection. Examination of the video tapes indicates that the dye reaches the liquid surface within two seconds of the sparger air flow having been started—the dye arrives at the surface with the first and second bubbles to reach the surface. Because of the aggressive splashing caused by the bursting bubbles, the dye was observed to reach the ZOI boundary at the liquid surface within about 60 seconds at 15 ACFM (boundary at about 52 inches). For 40 ACFM, the dye arrived at the tank wall (radius 76 inches) within about 60 seconds.

The electrolyte tracer results (see Figure 10.3 through Figure 10.6) also suggest a cellular ZOI structure with significant inflow in regions close to the sparger tube. It appears possible that the relatively long time for the electrolyte tracer to reach the probes, when compared to the vertical velocity profile data discussed previously, indicates that the probes were in locations beneath the robust inflow and recirculation regions. Most of the tracer would have been entrained by recirculation cells around the probes.

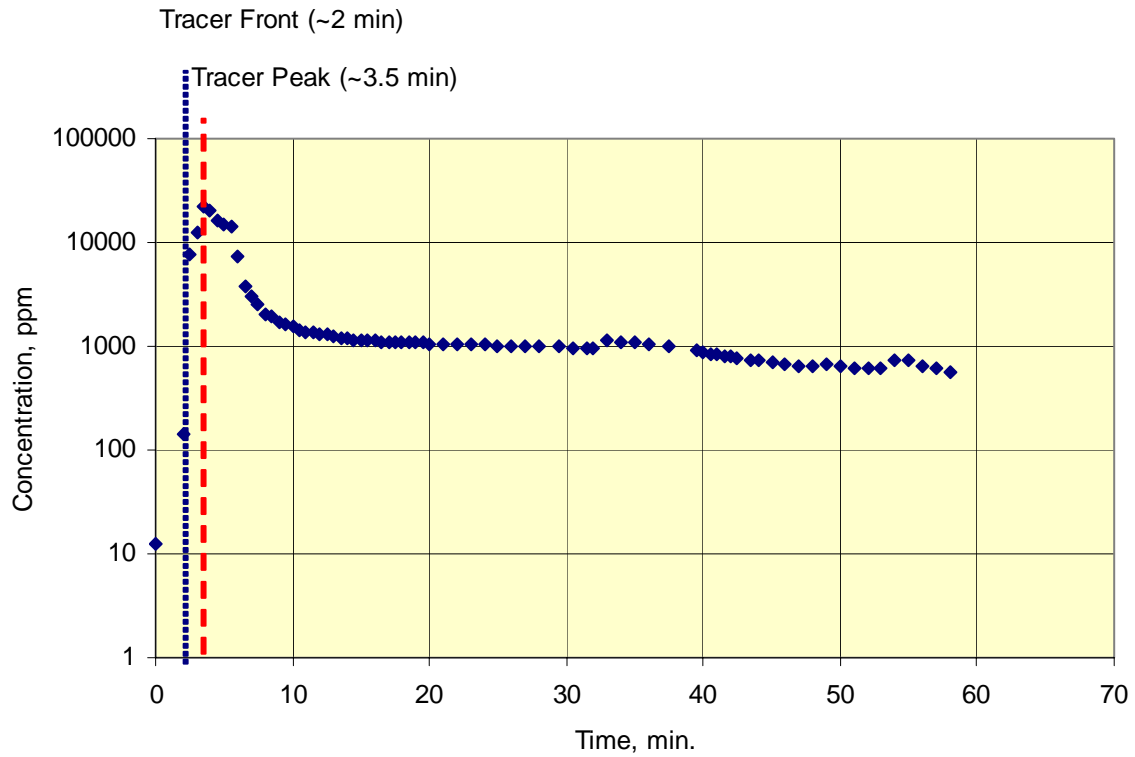


Figure 10.3. Circulation Time Test Results for ISE A at 15 ACFM

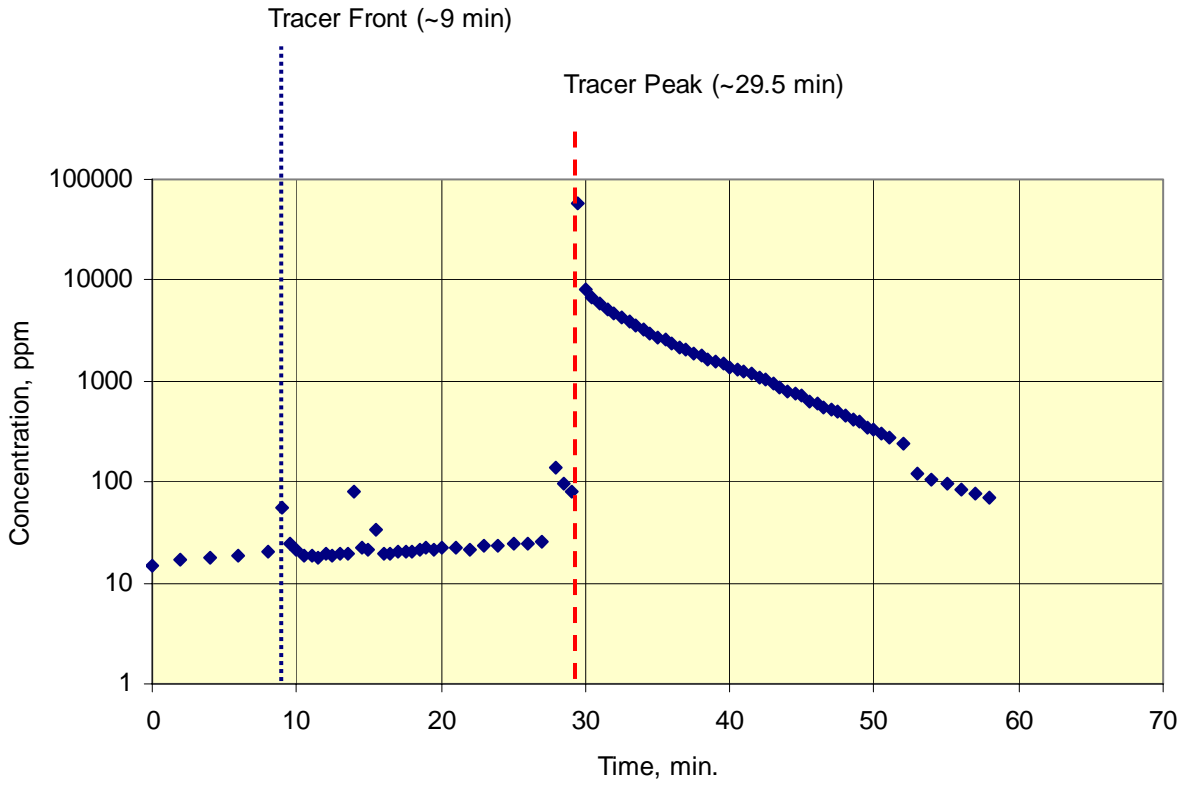


Figure 10.4. Circulation Time Test Results for ISE B at 15 ACFM

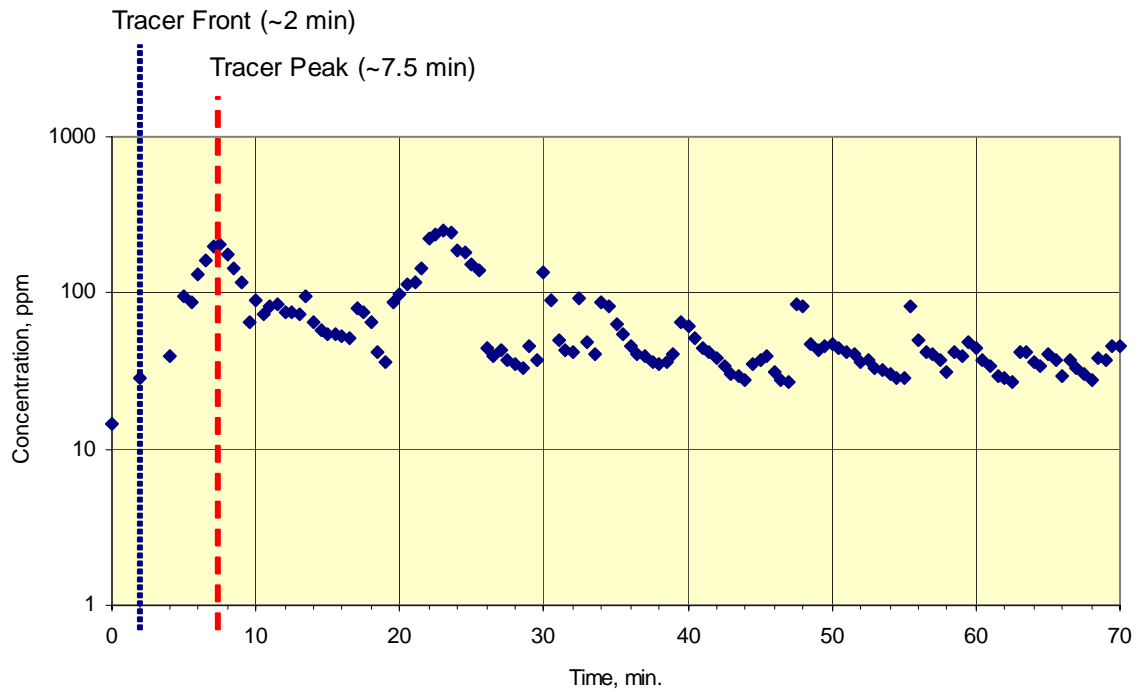


Figure 10.5. Circulation Time Test Results for ISE A at 40 ACFM

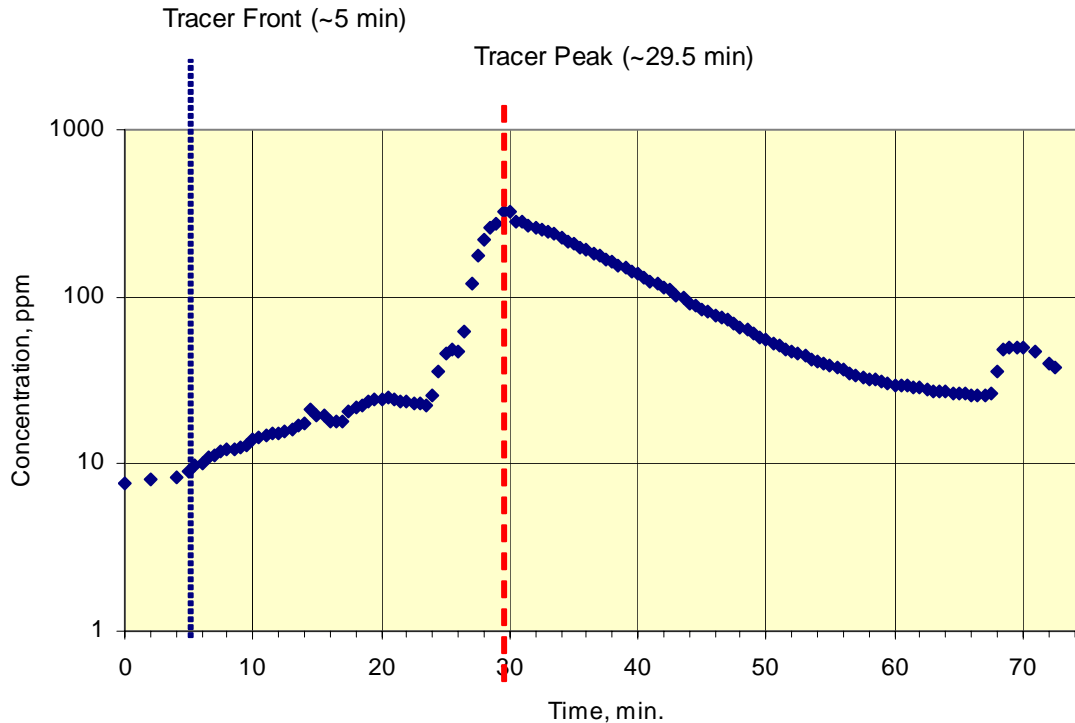


Figure 10.6. Circulation Time Test Results for ISE B at 40 ACFM

From these data, the circulation times and distances for each segment in the circulation path are compiled in Table 10.1 and Table 10.2. Each of the segment times and distances are summed to estimate a total circulation time and velocity for the 15 ACFM and 40 ACFM air-flow rates. These data indicate that the minimum circulation time for the 15 ACFM and 40 ACFM air-flow rates are 12 minutes and 8 minutes, respectively. The average circulation time for the ROB and ROB to ZOI segments were not measured because of the method used (visual indication with optical dye). However, these circulation times were much smaller than the ZOI circulation times. For this reason, the average circulation times can be estimated by neglecting these times. These data indicate that the average circulation time for the 15 ACFM and 40 ACFM air-flow rates are 33 minutes and 37 minutes, respectively.

Table 10.1. Minimum Circulation Time Calculations at 15 ACFM/40 ACFM

Circulation Path Segment	Distance (in)	Circulation Time (mm:ss)	Estimated Velocity (mm/sec)
Sparge Tube Nozzle to Surface (ROB)	117/117	0:02/0:02	1400/1400
Surface to ZOI Boundary (ROB to ZOI)	52/76	1:00/1:00	22/32
ZOI Surface to ZOI midpoint (ZOI)	60/60	2:00/2:00	13/13
ZOI midpoint to Sparge Tube Nozzle (ZOI to ROB)	56.3/57.7	9:00/5:00	2.6/4.9
Total	285.3/310.7	12:02/8:02	10/16

Table 10.2. Average Circulation Time Calculations at 15 ACFM/40 ACFM

Circulation Path Segment	Distance (in)	Circulation Time (mm:ss)	Estimated Velocity (mm/sec)
Sparge Tube Nozzle to Surface (ROB)	117/117	NM/NM	NM/NM
Surface to ZOI Boundary (ROB to ZOI)	52/76	NM/NM	NM/NM
ZOI Surface to ZOI midpoint (ZOI)	60/60	3:30/7:30	7.3/3.4
ZOI midpoint to Sparge Tube Nozzle (ZOI to ROB)	56.3/57.7	29:30/29:30	0.8/0.8
Total	285.3/310.7	~ 33:00 ^(a) /~37:00 ^(a)	3.7 ^(a) /3.6 ^(a)
NM – not measured			
(a) Total values calculated neglecting ROB circulation times.			

11.0 Aerosol Generation

This test was conducted to evaluate the mass of aerosol emitted into the tank head space under various sparging conditions. The intended approach was to conduct measurements using three measurement techniques: size fractionated point sampling, total aerosol exhausted through tank ductwork, and measurement of the mass of settling particles. Only the size fractionated sampling technique achieved valid results. This technique used size selective samplers to collect aerosol particles in the headspace above the tank at three size classifications: total suspended particulates, PM10, and PM2.5. Total suspended particulates (TSP) are any particles suspended in the air, PM10 includes all particles less than 10 micrometers in aerodynamic diameter, and PM2.5 includes all particles less than 2.5 micrometers in aerodynamic diameter. Aerodynamic diameter defines a particle with aerodynamic properties the same as a sphere of water of that diameter. This technique uses impaction plates to remove all particles larger than the desired particle size before they are collected on the sample filter. It should be noted that the TSP measurements measure particles actually suspended in the air and not all particles that are airborne. Particles larger than approximately 50 micrometers could have been airborne in the tank headspace, but would fall back to the liquid surface too fast for the sampler to collect the particles (Seinfeld and Pandis 1998). These larger particles are not considered to be suspended in air. The samples were collected on filters. The filters were weighed before and after sample collection to determine the aerosol mass collected. A mass concentration measurement for each size classification was then determined. The filters were kept in a temperature/humidity-controlled chamber for 24 hours before analysis (20 °C, 40% RH), so some drying of the aerosol collected on the filters occurred. The mass collected on these filters was later measured by the analytical laboratory: Air Metrics, Eugene, Oregon

11.1 Materials and Methods

11.1.1 Apparatus

The multiple tube sparging test stand described in Section 5.1 was used for these tests. A plastic tarp was installed covering the top of the tank, and a 12-inch exhaust duct was running out of the tank. This was intended to seal the tank headspace from outside air while providing an exhaust for the air injected during sparging. This configuration was considered to be an adequate representation of the tanks that will be used at the WTP for the purpose of modeling the mass of aerosol emitted as a result of sparging. Tests were conducted at three sparging flow rates. Nominally, target rates were $\frac{1}{3}$, 1, and $\frac{7}{5}$ times the design^(a) sparging flow rate of 200 cubic feet per minute.

11.1.2 Simulant

The kaolin/bentonite simulant described in Section 5.2 was used in these tests.

(a) The design sparging air flow rate was provided by BNI and is based on the scaling relationships developed in this document. This tank and sparging configuration does not represent an actual tank in the waste treatment plant.

11.1.3 Methods Used

11.1.3.1 Size Selective Sampling

Size selective sample inlets were installed above the surface of the liquid at three heights (14, 78, and 99 inches above the static liquid surface). At each sample height, three different size fraction samples were collected using MiniVol™ aerosol samplers (Air Metrics, Eugene, Oregon) with three different inlets. Sampler configuration consisted of the size selective inlet and filter holder located inside of the tank at the desired location. The sample pumps and controllers were located outside of the tank and connected to the sample heads with tubing. Each sample location had a sampling device attached to it. This minimized the amount of equipment inside of the tank, thus reducing obstruction of aerosol movement within the tank headspace. The MiniVol's internal sampler timers were synchronized to start and stop simultaneously. For the first test, the sample duration was one hour. For the second and third tests, at the higher sparging rates, the sample duration was 30 minutes. Sparging was started before initiating sampling. Approximately 20 minutes was allowed between the start of sparging and the beginning of aerosol sampling to allow for equilibration of aerosol concentration within the tank headspace. The volume of the headspace was estimated to be 1800 cubic feet. Therefore, at the lowest sparging rate, one volume change took approximately 24 minutes, and at the highest sparging rate, one volume change took approximately 6 minutes.

At the conclusion of each sampling period, sparging was stopped, and the sampler inlets and filter holders were removed. In a clean working area, filters were removed from their filter holders and placed into individual sealed storage containers. New filters were loaded into the sampling heads, the sample inlets were cleaned, and the next test was started.

11.1.3.2 Duct Sampling

Exhaust duct measurements of air flow were attempted to determine if duct sampling for aerosol would be viable. No measurable air flow within the exhaust ductwork was detected during any of the tests. The lower threshold velocity for the instrument used (thermocouple selector indicator hot wire anemometer) was 0.1 meters per second, which corresponds to a volumetric flow rate of 15 CFM. The results of these tests indicate that there was no significant exhaust through the exhaust ductwork, and the tank air was being exhausted through gaps in the tarp.

11.1.3.3 Splatter Measurements

In an effort to evaluate the amount of clay that settled back into the liquid after becoming airborne, a splatter sampler was installed over the liquid surface. A 9-inch-high can with a pre-weighed filter was suspended 18 inches above the surface of the liquid during the initial aerosol test ($\frac{1}{3}$ full flow). There was such a large amount of splatter of large non-aerosol drops a few minutes after the start of sparging that the can filled completely with liquid. While this technique did not prove useful for the aerosol measurements, it did provide further qualitative evidence that a large amount of the material that becomes airborne was too large to be considered suspended in air. This measurement technique may prove useful in the future with a few modifications.

11.2 Results and Discussion

A summary of the test results is outlined in Table 11.1. Examination of the results revealed some distinct trends. The results indicated a positive correlation between sparging flow rates and mass concentrations for each of the three size fractions (Figure 11.1, Figure 11.4). There was also a decrease in aerosol concentration at increasing heights above the surface of the liquid for the TSP and PM10 size fractions (Figure 11.1, Figure 11.2 and Figure 11.3). However, for the $\frac{1}{3}$ full flow sparging test, there was little change in the vertical concentrations of PM2.5. In general, the results make sense. Higher aerosol concentrations are located near the liquid surface and at higher sparging air-flow rates. The particle size distribution of emitted aerosol appears to be a function of sparging air-flow rate. During the $\frac{1}{3}$ full flow test, the PM10 and TSP concentrations were not significantly different from each other at the three sampling heights. At the higher sparging rates, there was a significant difference between the TSP and PM10 concentrations at sample location 1.

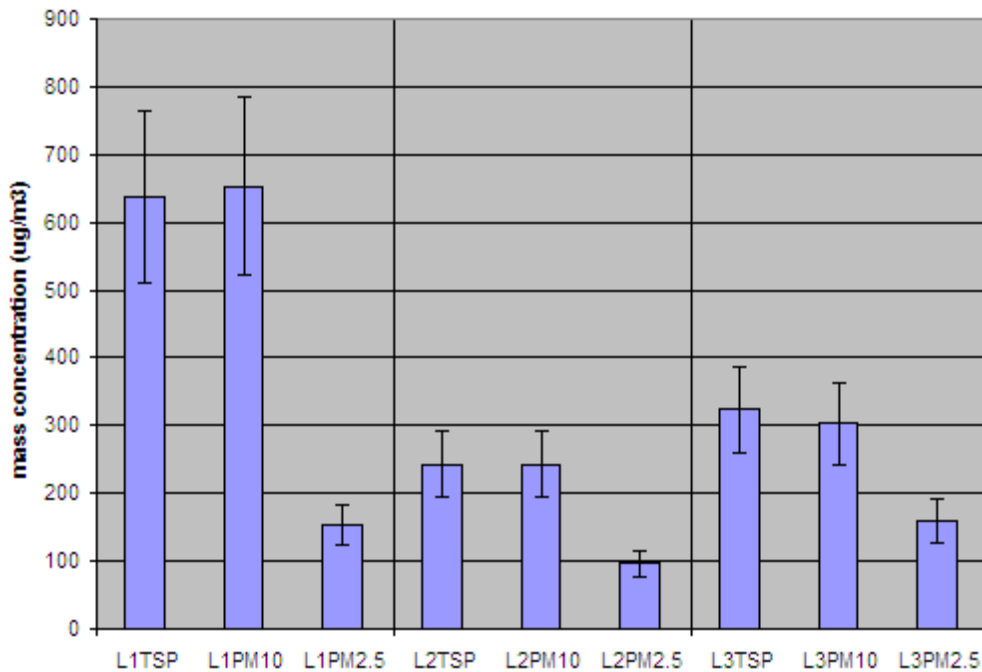


Figure 11.1. Distribution of Aerosol Mass Concentrations ($\pm 20\%$) at each Sample Height for each Size Fraction During the $\frac{1}{3}$ Full Flow Test

Table 11.1. Summary of Results for Aerosol Testing in the Headspace of a Tank Under Sparging Conditions

Sample Name	Test #	Size Fraction	Location	Height Above Liquid (in)	Average Sparging Flow at Nozzle (acfm)	Sample Period (min)	Sample Flow Rate (L/min)	Aerosol Mass Collected on Filter (milligram)	Air Volume Sampled (m ³)	Aerosol Mass Concentration (microgram/m ³)
L1TSP	1	TSP	1	14	65.3	60	5	0.191	0.3	637
L1PM10	1	PM10	1	14	65.3	60	5	0.196	0.3	653
L1PM2.5	1	PM2.5	1	14	65.3	60	5	0.046	0.3	153
L2TSP	1	TSP	2	78	65.3	60	5	0.073	0.3	243
L2PM10	1	PM10	2	78	65.3	60	5	0.073	0.3	243
L2PM2.5	1	PM2.5	2	78	65.3	60	5	0.029	0.3	97
L3TSP	1	TSP	3	99	65.3	60	5	0.097	0.3	323
L3PM10	1	PM10	3	99	65.3	60	5	0.091	0.3	303
L3PM2.5	1	PM2.5	3	99	65.3	60	5	0.048	0.3	160
L1TSP	2	TSP	1	14	203	30	5	0.503	0.15	3353
L1PM10	2	PM10	1	14	203	30	5	0.262	0.15	1747
L1PM2.5	2	PM2.5	1	14	203	30	5	0.069	0.15	460
L2TSP	2	TSP	2	78	203	30	5	0.091	0.15	607
L2PM10	2	PM10	2	78	203	30	5	0.083	0.15	553
L2PM2.5	2	PM2.5	2	78	203	30	5	0.049	0.15	327
L3TSP	2	TSP	3	99	203	30	5	0.195	0.15	1300
L3PM10	2	PM10	3	99	203	30	5	0.059	0.15	393
L3PM2.5	2	PM2.5	3	99	203	30	5	0.045	0.15	300
L1TSP	3	TSP	1	14	315	30	5	0.847	0.15	5647
L1PM10	3	PM10	1	14	315	30	5	0.532	0.15	3547
L1PM2.5	3	PM2.5	1	14	315	30	5	0.131	0.15	873
L2TSP	3	TSP	2	78	315	30	5	0.25	0.15	1667
L2PM10	3	PM10	2	78	315	30	5	0.214	0.15	1427
L2PM2.5	3	PM2.5	2	78	315	30	5	0.121	0.15	807
L3TSP	3	TSP	3	99	315	30	5	0.087	0.15	580
L3PM10	3	PM10	3	99	315	30	5	0.108	0.15	720
L3PM2.5	3	PM2.5	3	99	315	30	5	0.056	0.15	373
336 Background		TSP	NA	NA	NA	30	5	-0.005	0.15	-33
Field Blank		TSP	NA	NA	NA	NA	NA	-0.002	NA	NA
Field Blank		TSP	NA	NA	NA	NA	NA	-0.004	NA	NA

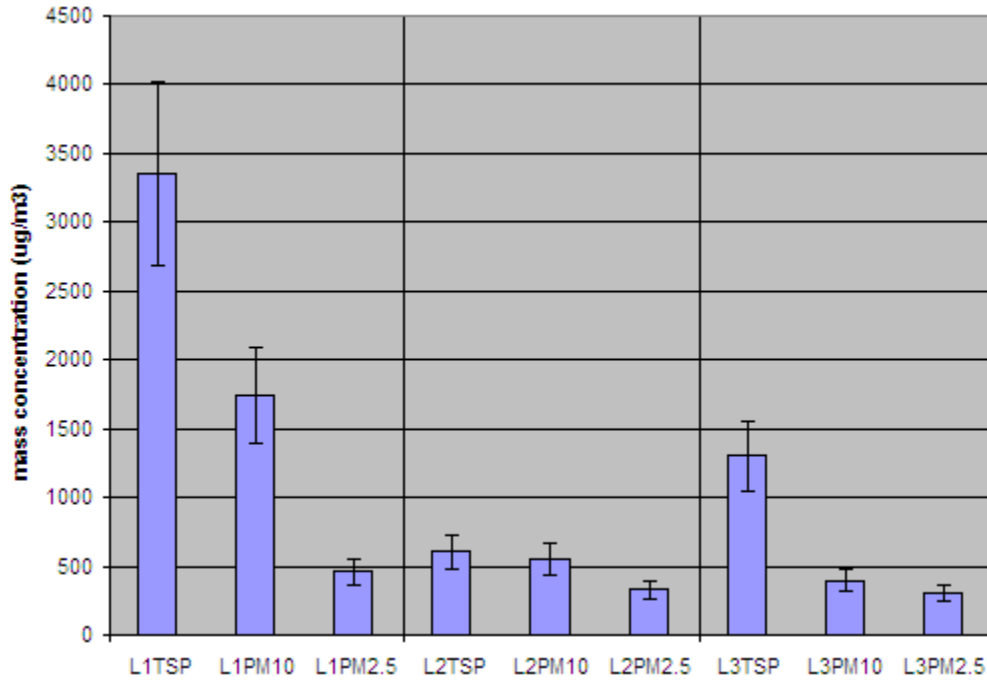


Figure 11.2. Distribution of Aerosol Mass Concentrations ($\pm 20\%$) at Each Sample Height for each Size Fraction During the Full Flow Test

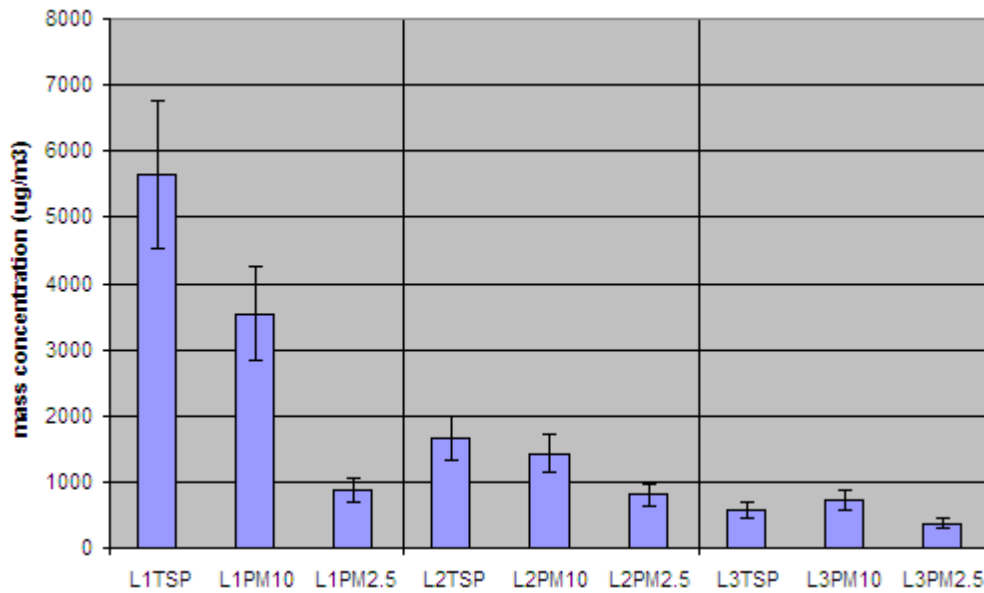


Figure 11.3. Distribution of Aerosol Mass Concentrations ($\pm 20\%$) at each Sample Height for each Size Fraction During the $7/5$ Times Full Flow Test

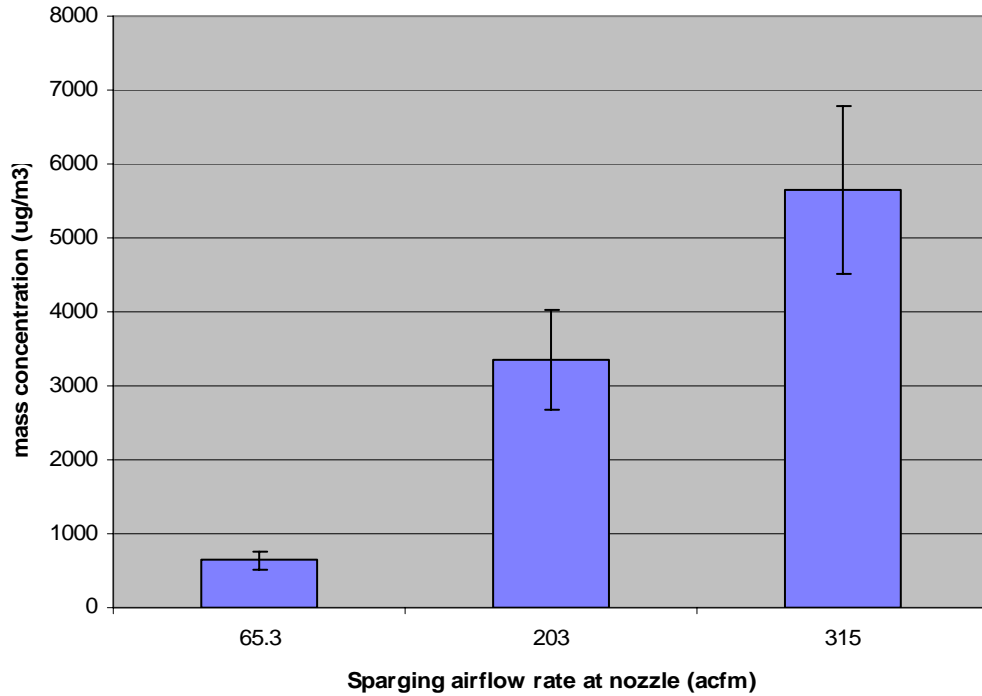


Figure 11.4. Distribution of Total Suspended Particulate Mass Concentrations ($\pm 20\%$) at Sampling Location 1 (14 inches above liquid surface) for each of the Three Tests

11.2.1 Experimental Accuracy

Three fundamental measurements were used to determine the aerosol mass concentration; aerosol mass collected, mean air-flow rate through the sampler, and the elapsed time for the sample collection period. The accuracy of the test results is critical in determining if observed differences in aerosol mass concentration are real or merely differences within the range of accuracy. The accuracy of the measurement of aerosol mass collected on each filter was better than $\pm 10\%$ (as provided by the analytical laboratory: Air Metrics, Eugene, Oregon). The sample duration was assumed to be accurate to ± 5 seconds, or less than 0.3% error. The flow rate of each sampler was calibrated before the test with a National Institute for Standards and Technology (NIST) traceable critical orifice calibration device. Each sampler was set to sample at 5 L/min. The calibrations showed that this setting for each instrument was well within 10% of the actual flow rate. Using a conservative approach of assuming the total error to be the sum of the errors, the overall accuracy of the aerosol mass concentration measurements is $\pm 20\%$.

12.0 Gas Retention and Release Behavior

The objective of these tests was to provide data on the gas-release characteristics of a non-Newtonian fluid when agitated by a sparging system. The purpose of this task was to deliver a set of plots that show gas holdup levels as a function of time after sparging is initiated and initial gas holdup.

12.1 Materials and Methods

12.1.1 Apparatus

Two tanks located in the 336 building were used for the multitube sparger tests. The main tank was the CBT described in Section 5.1. The other tank, which is slightly larger than the CBT, has an elliptical bottom and is called the supernatant tank (SNT). The SNT tank has an inside diameter of 153 inches. The SNT tank had four PJMs installed during the multitube sparger tests. As discussed in Section 12.1.3, all the multitube gas-release tests were conducted in the CBT, and the SNT was used only to fully mix hydrogen peroxide added to the simulant to generate gas before and to degas after the sparger operation.

Air-flow rates to nine spargers were individually measured by Dwyer VFC-122 manometers with ranges of 1 to 10 ± 0.5 , 3 to 25 ± 1.0 , and 4 to 50 ± 3.5 CFM. The air pressure of each of nine sparger air flows was measured by an Ashcroft air pressure gauge with the range of 0 to 30 ± 1.5 psi. The temperature of these sparger air flows was obtained by Omega Type J thermometers with a range of 0 to 100 ± 1.1 °C. The simulant temperature was measured by a Type K ungrounded thermocouple with a range of 0 to 500 ± 2.2 °C or $\pm 0.75\%$, whichever is greater. The CBT weight was measured by three 0 to 100 k-lb load cells, one under each of the tank's support legs.

The simulant surface level was measured in two ways, with a conventional measuring tape and with Gems 201002-UCL-200 ultrasonic probes with a range of 0 to 120 inches. Because the ultrasonic level sensor readings were observed to drift and shift at times, the hand-level measurements were used for gas volume calculations. As discussed later, ultrasonic sensor readings show the qualitative transient gas-release behavior trends in gas release during the sparger operation adjusted with the hand-level measurements. The gas-volume calculations by the ultrasonic readings are also provided in this report for information only.

A subset of the instrumentation data used for the multitube sparging testing was input, displayed, and saved in a PC-based data acquisition system (DAS). This DAS is the same one used on previous large-scale PJM testing in the 336 building but was modified for the smaller number of parameters. Data processed by the DAS were CBT tank weight, CBT tank temperature, and simulant surface levels measured by the ultrasonic level probes. The DAS is based on a Dell Optiplex GX270MT PC running DasyLAB 7.000.03 data-acquisition software under Windows XP. Analog-to-digital conversion is accomplished by a measurement computing PCI-DAS6402/16 card. The card was set for all channels to a 0 to 5-V input range. Signal conversion was accomplished by industry-standard 5B modules that converted all the input signals to a standard 0 to 5 V for all channels. The 5B modules were mounted on a measurement computing International Standards Organization (ISO) RACK 16 terminal board. Power for the 5B modules was obtained from a separate 5-VDC power supply. Power for the level probes was obtained from 24-V DC power supplies. All data signals were sampled at 64 Hz and had a running

average of ½ second applied. Data were displayed on the DAS PC monitor as digital meters or strip charts as appropriate. Data were saved to the hard disk in ASCII files at rates appropriate to the particular test.

The tank weight was sensed by three 100,000-lb-range BLH Z-Blok load cells, summed in a summing-junction box, and processed by a Hardy HI2151/20/WC weigh computer powered by 120 VAC. The weigh computer output a 4 to 20-mA analog signal proportional to 0 to 300,000 lb. This signal was converted to 0 to 5 V by a 5B-32-02 module. Signal scaling was 0 to 300,000 lb \propto 4 to 20 mA, which is \propto 1 to 5 V.

The temperature signal was input to the DAS as a Type K thermocouple signal, which was converted to 0 to 5 V by a 5B-47K-05 module. Signal scaling was 0 to 500°C \propto 0 to 5 V.

The 10 simulant surface levels were initially sensed by graphical exposure modeling system (GEMS) UCL-200 ultrasonic level probes. Alternatively, two other types of level probes were tried, a K-TEK SureShot 30 and an Optech Sentinel 3100 laser level probe. Up to eight ultrasonic level probes were actually used for the multitube sparger tests. All level probes were powered by 24 VDC from the DAS power supplies and output 4 to 20-mA signals that were converted by 5B-32-02 modules. Scaling was 0 to 48 inches \propto 4 to 20 mA with sensor datum 48 inches from the tank rim. Because only relative changes in level were required for sparging testing, absolute references were not required.

12.1.2 Simulant

The kaolin/bentonite simulant described in Section 5.2 was used in these tests.

12.1.3 Methods Used

Fifteen multitube sparger gas-release tests were conducted. Ten tests were with gas generation, and the rest were without gas added. These tests were performed in the CBT using nine ¾-inch-diameter spargers arranged as shown in Figure 5.6 (see also the reference North). Spargers A1 through A4 are placed 66 inches from the tank center, spargers B1 through B4 are placed 48 inches from the center, and sparger C was placed at the tank center, as indicated in this figure. Locations of eight ultrasonic surface probes (1 to 4 and 7 to 10) are also shown in the figure. Figure 5.7 shows the depths of the sparger tubes in a profile view. The nozzles of spargers A1 through A4 were located at 100.3 inches below the tank rim, those of spargers B1 through B4 were 120.0 inches below the tank rim, while that of sparger C is 160.6 inches below the tank rim. Spargers were spaced so that each one's ZOI overlapped with the ROB of the others, as illustrated in Figure 6.3.

Sparger air-flow rates were targeted at 100% and 33% of the full air flows at the sparger tube submerged nozzles. For the full sparger air flow (204 ACFM), the intended air flows to each of nine spargers, A1 to A4, B1 to B4, and C were targeted at 17.5, 32.4, and 4.6 ACFM, respectively. For the 33% flow rate condition, approximately 1/3 of these air-flow rates were targeted for each sparger. Because the simulant depth in the test vessel is less than full-scale, the change in hydrostatic pressure from the bottom to the top is lower so that the test full flow rate corresponds to about 2/3 of the full-scale flow rate at the surface.

In situ gas generation was simulated in these tests by oxygen generated through the decomposition of hydrogen peroxide. The hydrogen peroxide was added to the simulant in the SNT and mixed with four PJMs. The peroxide-laden simulant was then pumped into the CBT and allowed to stand until all or most of the hydrogen peroxide had decomposed. This provided the initial retained gas volume to conduct the multitube sparger gas-release tests. The initial CBT weight (before SNT transfer and peroxide addition) was the target weight used for returning the peroxide-laden simulant to the CBT. The unavoidable slight differences in weight (on the order of 100 lb) were included in calculating simulant volume for gas release.

After the simulant surface level reached a steady level in the CBT, sparging began at a preset air-flow rate and continued until the surface level again became steady, indicating that essentially all releasable gas had left the simulant. To remove gas not released by sparging, the simulant was again pumped over to the SNT, where it was thoroughly degassed by PJM mixing, including multiple PJM overblows. The simulant was then transferred back to the CBT for a final surface-level reading, again targeted to match the initial pre-test CBT weight.

For each multitube sparger test, the simulant had been at rest in the CBT after a previous multitube sparger test. Thus it was in the CBT without any disturbance at least overnight at the beginning of each gas-release test.

To measure simulant rheology, samples were taken in SNT before the hydrogen peroxide was added, and an additional sample was taken in the CBT after degassing by PJMs at the end of the test. To further confirm the residual gas content at the end of the sparger test, the sample taken in the CBT was also analyzed for simulant density.

The following experimental steps were executed during every sparging test with few exceptions:

- Step 1. The simulant surface level and the CBT weight were measured. The surface level was measured using ultrasonic surface-level probes (see Figure 5.6 for level probe placement) and a hand-measurement with a measuring tape. The hand measurements of surface level were conducted at a single location in the CBT for the first nine tests and 10 locations for the last six tests. The simulant surface level was continuously measured by ultrasonic surface-level probes, together with CBT weight, and was recorded to DAS throughout the test duration, except when the simulant was not in the CBT.
- Step 2. Air flow to the nine spargers was adjusted to a pre-assigned flow rate. Then the air flows to the spargers were stopped.
- Step 3. The simulant was transferred from the CBT to the SNT.
- Step 4. The simulant surface level and weight in the SNT and the CBT were recorded. Simulant samples were taken from the SNT after it was mixed by pulse jet mixing.
- Step 5. A pre-determined mass of hydrogen peroxide was added to the simulant in the SNT to produce the required initial gas fraction. The simulant recirculation pump in the tank was operating during hydrogen peroxide addition. Afterward, the simulant was fully mixed by operating the PJMs.

- Step 6. The simulant containing the added hydrogen peroxide was transferred back from the SNT to the CBT, attempting to match the initial pre-test weight measured under Step 1. The simulant volume calculations were adjusted for small differences in actual weight, assuming a simulant density of 1.17 g/mL.
- Step 7. The simulant surface level and the total CBT weight were measured.
- Step 8. The simulant surface level was then measured over time by a measuring tape at one or ten locations and up to eight ultrasonic surface-level probes until the simulant surface level was no longer rising, indicating that most of the hydrogen peroxide had decomposed.
- Step 9. At that point, air flows were supplied to the nine spargers at the pre-adjusted flow rates to start the gas-release test. During sparger operation, the simulant surface fluctuations prevented manual measurements and the simulant surface level was monitored only by the ultrasonic probes.
- Step 10. When the simulant surface level was no longer decreasing, indicating most of the releasable gas was removed, the air flows to the spargers were stopped to terminate the sparger gas-release test.
- Step 11. The simulant surface level was measured manually at one or ten locations. As stated above, the DAS was continuously recording the simulant surface levels (by ultrasonic surface probes) and tank weight, as long as the simulant was in the CBT.
- Step 12. The simulant was transferred from the CBT to the SNT.
- Step 13. The simulant in the SNT was degassed with PJM mixing and many (10 to 20) overblows.
- Step 14. The degassed simulant was transferred from the SNT back to the CBT, attempting to match the initial pre-test weight measured under Step 1.
- Step 15. The simulant surface level was measured manually at one or ten locations and also by the ultrasonic level probes.
- Step 16. A simulant sample was taken from the CBT and analyzed for rheology and density.
- Step 17. The DAS system continuously measured and recorded the simulant surface level (with the ultrasonic surface probes) and tank weight. The system was stopped to end the multitube sparger test.

It took between 10 and 18 hours to complete these 17 steps for each test.

12.2 Results and Discussion

Fifteen multitube sparger tests were conducted with and without gas generated by hydrogen peroxide decomposition. Ten tests were performed with initial gas volume ranges from 0.7 vol% (June 16 test) to 2.4 vol% (June 11 test). Five tests were conducted without gas generation to determine whether sparging by itself introduced any long-term holdup.

Figure 12.1 is a photograph of the southeast quadrant of the CBT showing spargers A4, B3, B4, and C inserted in the simulant. The tank wall with a vinyl sheet cover is shown on the right. Spargers B3 and C are shown in the lower center and far left of the photograph, while spargers A4 and B4 are shown on the far right and top. The locations of these four spargers are shown in Figure 5.6. This photograph was taken before the test conducted on July 8, 2004, showing the quiescent simulant surface. The initial gas content of this test was 1.3 vol%. The elapsed time is shown in the lower left corner, indicating that it was 1 minute and 58.06 seconds after the videotaping started. The videotaping usually started 5 to 10 minutes before the sparger started.

Figure 12.2 shows the simulant surface during sparging in the same July 8, 2004, test with the total air-flow rate of 170.9 ACFM through nine spargers. Four of the nine spargers, A4, B3, B4, and C, were injecting 15.2, 27.1, 26.8, and 3.6 ACFM of air, respectively. The figure clearly indicates the vigorous simulant movement, with clear ROBs, around each sparger, producing strong simulant mixing on the surface and releasing most of the gas originally stored in the simulant. At the end of the sparging, the remaining gas content in the simulant was 0.0 vol%. Although it is not clear in this photograph, large ZOIs are also created around the ROBs.



Figure 12.1. Simulant Surface Before Sparger Operation on July 8, 2004



Figure 12.2. Simulant Surface During Sparger Operation with 171 ACFM Air Flow on July 8, 2004

Figure 12.2 shows the simulant surface during sparging in the same July 8, 2004, test with the total air-flow rate of 170.9 ACFM through nine spargers. Four of the nine spargers, A4, B3, B4, and C, were injecting 15.2, 27.1, 26.8, and 3.6 ACFM of air, respectively. The figure clearly indicates the vigorous simulant movement, with clear ROBs, around each sparger, producing strong simulant mixing on the surface and releasing most of the gas originally stored in the simulant. At the end of the sparging, the remaining gas content in the simulant was 0.0 vol%. Although it is not clear in this photograph, large ZOIs are also created around the ROBs.

Figure 12.3 and Figure 12.4 show the simulant surface before and during sparger operation on June 11, 2004, when the air-flow rate was 68.2 ACFM, approximately $\frac{1}{3}$ of full flow. The simulant with 322-Pa Bingham yield stress had the initial gas content of 2.4 vol%. These figures show spargers B3 and A4, while sparger B4 is under the metal bar that held an ultrasonic surface-level probe, shown on the far right of the photograph. The ROBs are much smaller with the lower air flow, and the simulant surface mixing was much less vigorous than those of the full flow July 8, 2004, test. At the end of this sparging test, the simulant still had 0.7 vol% of the gas.

During sparging, the simulant surface was highly disturbed, making hand measurements of the surface level impossible. However, the ultrasonic surface-level probes were able to follow the fluctuating surface levels as gas was released. Figure 12.5 shows the simulant surface-elevation changes with time measured by the ultrasonic surface-level probes during the sparger operation for eight full air-flow tests, including the test case shown in Figure 12.1 and Figure 12.2. The sparger air-flow rates for all eight cases were 202 to ~206 ACFM, except the July 7 and July 8 tests, which have air-flow rates of 171.3 and 170.9

ACFM, respectively. The initial gas content in the simulant for these eight cases was 0.8 to 2.0 vol%. These conditions are summarized in Table 12.1. The test ID number in this table corresponds to the test date in a yymmdd format.



Figure 12.3. Simulant Surface Before Sparger Operation on June 11, 2004



Figure 12.4. Simulant Surface During Sparger Operation on June 11, 2004 with 68 ACFM Air Flow

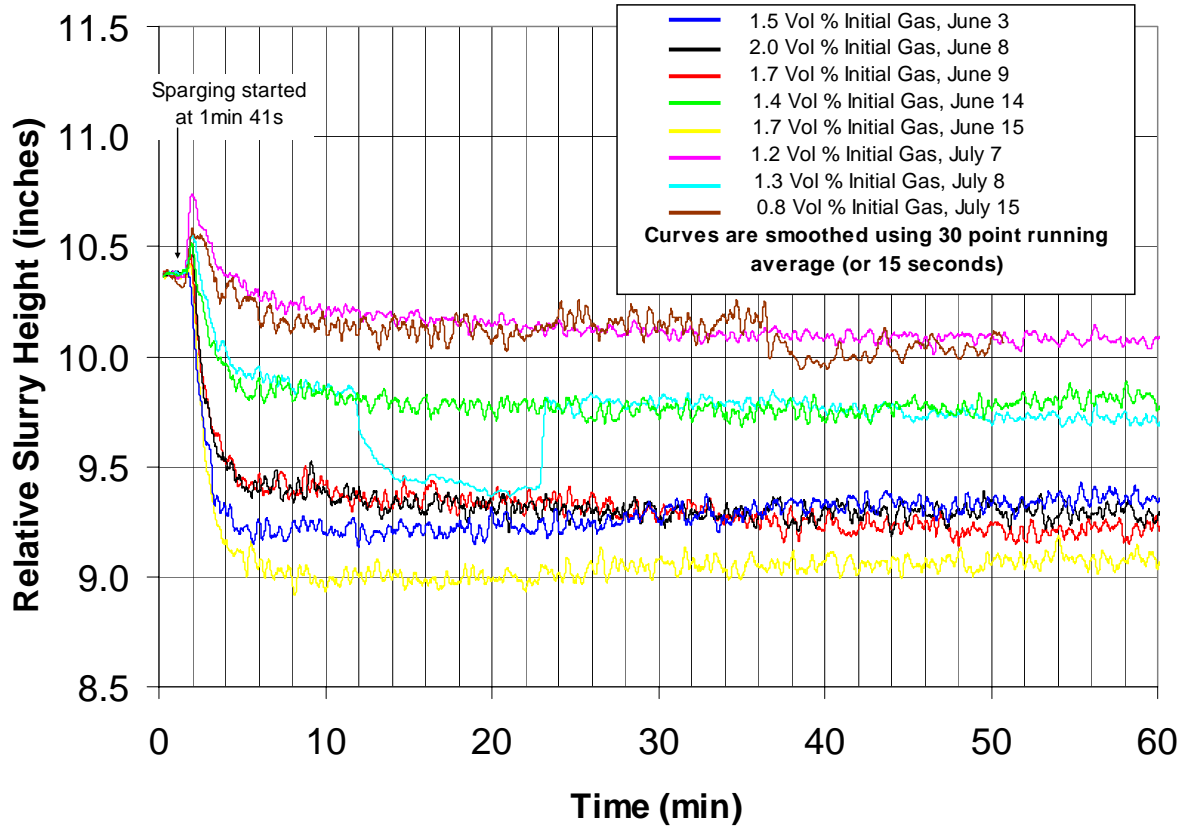


Figure 12.5. Relative Ultrasonic Level Probe Readings While Sparging at Full Air Flow

Table 12.1. Multitube Sparger Test Conditions

Test ID	Air-Flow Rate (ACFM)	Average Bingham Plastic Slurry Shear Stress (Pa)	Initial Gas Volume Estimated by Hand Surface Measurements (vol%)
040603	204.2	28	1.5
040608	202.1	29	2.0
040609	202.6	30	1.7
040707	171.3	355	1.2
040708	170.9	37	1.3
040715	206.3	40	0.8
040614	203.3	32	1.4
040615	206.0	32	1.7
040611	68.2	32	2.4
040616	57.8	34	0.7
040713 ^(a)	338.1	37	0.3 ^(a)
040622 ^(a)	207.1	33	0.0 ^(a)
040706 ^(a)	175.1	-	0.1 ^(a)
040618 ^(a)	68.7	333	0.2 ^(a)
040712 ^(a)	56.7	377	0.1 ^(a)

(a) These were no-gas experiments with no added hydrogen peroxide; thus initial gas volume fractions should be zero.

In Figure 12.5, for comparative purposes, the initial surface levels and sparging start times were assigned to approximately 10.4 inches and 2 minutes, respectively, for all eight tests. This figure clearly shows the sudden level rise (a lifting of the slurry by air injected by the spargers) “dragon ear” at sparger startup, indicating short-term sparger holdup. This short-term holdup was rapidly eliminated after the sparger was shut down. During sparging, the simulant surface levels for all eight tests show an initial rapid reduction in the first few minutes, indicating a quick release of gas accumulated within the simulant. After the initial rapid reduction, the simulant surface levels gradually decrease, asymptotically approaching the final surface levels because of loss of gas.

The sparger test conducted on July 8 (Test ID 040708) had 1.3 vol% gas in the simulant before sparging. In this case, the sparger was stopped after 10 minutes and then restarted 11 minutes later (light blue line in Figure 12.5). This surface-elevation change also shows rapid disappearance of short-term holdup right after the first sparger shut down, and its reappearance when sparging resumed.

Manual surface-level measurements could be taken only at the beginning and end of the tests while the spargers were off. As stated above, in the July 8 test (Test ID 040708), spargers were shut down for about 1111 minutes after the initial 10-minute operation. During this brief shutdown period, manual surface-level measurements were taken to obtain short-term gas-release data, as will be discussed later. After restarting the spargers, the surface level went up to what it had been just before sparging was interrupted, then continued its gradual descent to the end of sparger operation.

Figure 12.6 shows the transient surface elevation measured by the ultrasound level probes for the $\frac{1}{3}$ full flow sparger tests conducted June 11, 2004 (Test ID 040611) and

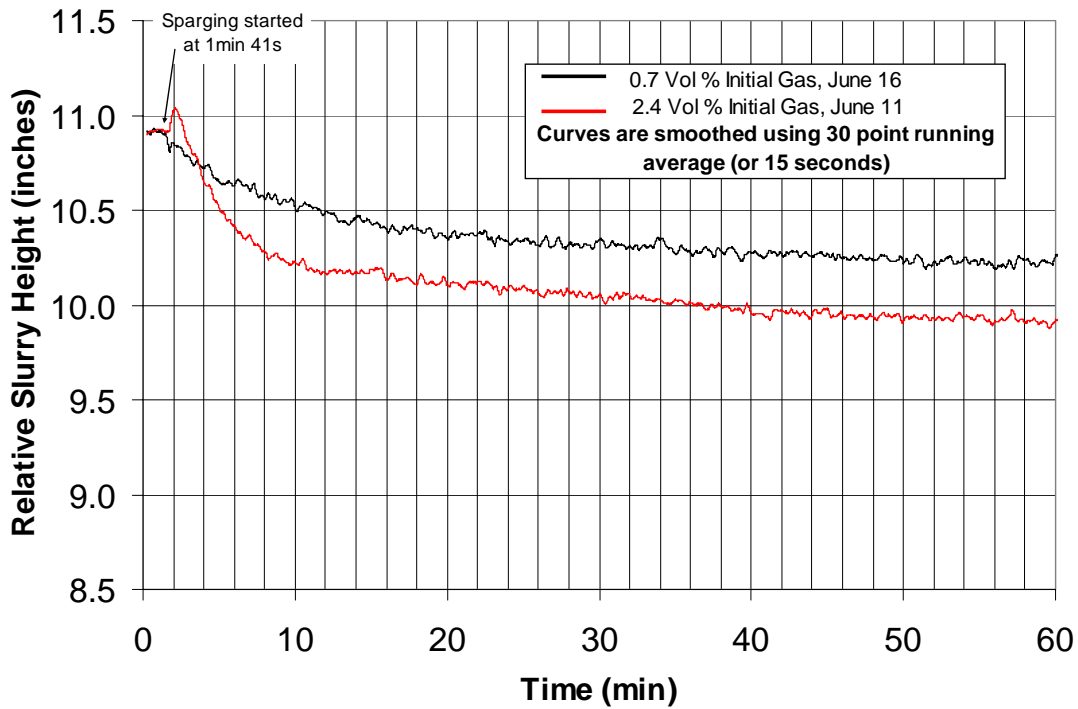


Figure 12.6. Relative Ultrasonic Level Probe Readings While Sparging at $\frac{1}{3}$ the Full Air Flows

June 16, 2004 (Test ID 040616). The initial gas content of these test cases is 2.4 and 0.7 vol%, respectively. The trend in surface-elevation changes is similar to full flow sparger cases (see Figure 12.5), except that the initial rapid reduction of the surface level in these two cases is much slower than in the full-flow cases.

The volume of retained gas in the simulant was determined from the change in simulant volume calculated from a multiplication of the change in surface level and a volume-to-height ratio. The volume-to-height correlation was obtained by recording changes in CBT weight during stepwise water additions where the corresponding water surface level and water temperature were also recorded. The equivalent water volume was calculated from the mass and density of water at the measured temperature (i.e., from tables in *Perry's Chemical Engineers' Handbook* [Perry and Green 1977] or equivalent source).

The computation of gas volumes from changes in surface level requires a “zero gas” reference level from which changes are measured. The “zero gas” surface level was recorded in the CBT after PJM degassing steps at the end of the test sequence, representing a simulant condition before gas generation. This no-gas assumption was made for the following reasons:

- The simulant sample was collected at the end of the test (see Step 16 in Section 12.1.3). Comparing the density measurements of the as-received simulant and of the same simulant degassed by stirring and 1:1 dilution by water revealed that there was no gas left within the accuracy of the density measurements. Because the diluted simulant is estimated to have only about 1 Pa of the shear strength, compared with the undiluted simulant with about 60 Pa shear strength, degassing by this method is expected to be essentially complete. Thus it is reasonable to assume that the undiluted simulant has minimal gas content.
- The simulant density increased slightly due to sparging-induced water evaporation over the multitube sparger testing period in June and July. This implies that there is no gas buildup from one test to the next and that PJM overblows effectively removed most, if not all, of the gas in the simulant.
- The gas volume fractions in the simulant calculated by hand measurements of the simulant surface levels are generally smaller after PJM overblows at the end of the sparger test than at the beginning of the test before the hydrogen peroxide was added. Thus the simulant at the end of the test had the least amount of gas throughout the test sequence.

The simulant volume was corrected for small differences in weight between tank-to-tank transfers assuming a degassed simulant density of 1.17 g/mL. The pre- and post-sparging gas volume fractions were calculated as follows:

$$\text{Initial gas\%} = 100 * (L.2 - (L.1 + L.1c.2)) * DV.cyl / V.2 \quad (12.1)$$

$$\text{Unreleased gas\%} = 100 * (L.3 - (L.1 + L.1c.3)) * DV.cyl / V.3 \quad (12.2)$$

- where
- L.1 = simulant surface level in the CBT after degassing in the SNT
 - L.2 = level just before sparging when gas retention is at maximum
 - L.3 = level when sparging was terminated
 - V.2 and V.3 = simulant volumes calculated from L.2 and L.3
 - DV.cyl = volume change per inch of level change
 - L.1c.2 = (CBT weight [just before sparging] –last CBT weight (after PJM degas))/766.3 lb/in.
 - L.1c.3 = (CBT weight [just after sparging] –last CBT weight (after PJM degas))/766.3 lb/in.

The 766.3 lb/in of the simulant height in the CBT is based on 1.17 g/cm³ simulant density and dimensions of the cylindrical portion of the CBT.

The gas volumes determined from manual measurements are believed to be the only valid source of quantitative estimates of the retained gas volumes because the ultrasound level probes exhibited drift and shifts in simulant surface-level readings at times. Nonetheless, the elevation changes shown in Figure 12.5 reveal a very similar trend for all eight test cases, validating their use, at least in a qualitative evaluation of the transient surface-level changes during the sparging. These surface-level readings of the ultrasound probes were converted to gas volume fractions based on the gas volume fractions derived from pre- and post-sparging manual level measurements with Equations (12.1) and (12.2). The conversion is a linear correlation of gas volume fraction to simulant level where the average static surface level from the ultrasound sensors just before sparging corresponds to the associated gas volume fraction derived from the manual level measurements. Likewise, the post-sparging average static level from the ultrasound sensors corresponds to the post-sparging gas volume fraction determined from the manual level measurements.

An example of the gas-release behavior of full-flow sparging tests is shown in Figure 12.7, depicting the gas volume fraction versus time, based on the ultrasound surface-level probe readings for the multi-tube sparger test conducted on July 8, 2004 (Test ID 040708). One can also view this figure as a non-dimensional gas volume plot by regarding the initial gas volume fraction (in this case 1.3 vol%) as 100%, and the 0% gas volume (after the PJM overblows at the end of the test) as 0%. The simulant surface-elevation change of this test case was previously shown in Figure 12.1, Figure 12.2, and Figure 12.5 (see July 8 light blue line). This test began with 1.3 vol% retained gas. The initial spike in gas volume fraction is the “dragon ear” caused by the sudden injection of the large sparger bubbles, as discussed previously.

The manual surface-level measurements could be taken only when the spargers were not operating, i.e., before and after the tests. For this particular test, spargers were shut down for about 11 minutes after the initial 10-minute operation to allow a manual surface-level measurement, as stated above. The rapid drop (over about 3 minutes) in gas volume fraction of about 0.5 vol% when the spargers were shut down closely matches the sudden rise when they restarted and again the rapid drop at the end of additional 50-minute sparging. This represents the transient short-term holdup of the sparger bubble column. The hand measurements during this brief shutdown period indicated that, at that time, spargers had released all but about 0.1 vol% of the gas in the simulant within the uncertainty of about ± 0.5 vol%. The gas fraction corresponding to changes in ultrasonic level readings after the initial 10-minute sparging is about -0.1 vol%, as compared to the 0.1 vol% estimate from the hand measurements. Thus, it also confirms that the ultrasound readings may be usable for at least a qualitative evaluation of gas release. After restarting the spargers, the gas volume fraction fell roughly to -0.22 vol% over the remaining 50 minutes of sparging,

based on the ultrasound surface-level readings. However, this small decrease may have been the result of ultrasound sensor drift. The hand measurements at the end of the sparging indicate that the remaining gas volume was 0.0 vol%. The hand measurements indicate that gas release was rapid after sparging began and that essentially all releasable gas was removed within the first 10 minutes of sparger operation for this case. After the PJM overblows at the end of the test sequence, the gas volume fraction was zero as verified by laboratory density measurements of simulant samples.

The conclusion that almost all gas was released during the first 10 minutes of sparging was also supported by Figure 12.7. During the 11-minute break after the initial rapid gas volume drop, the surface level was still slowly decreasing, possibly because of the continuing release of the initial hydrogen peroxide-generated gas and the short-term sparger holdup. However, the surface level (minus the initial rapid drop) during this period without sparger operation fits reasonably well to the time-varying gas volume curve with the sparger operation as if there was no interruption of the sparger operation. This implies that the sparger was no longer the dominant mechanism for releasing the gas, indicating that there was essentially no releasable gas left after the 10-minute sparging.

As stated above, Figure 12.7 can also be viewed as a non-dimensionalized gas-volume plot by considering initial 1.3 vol% as 100% gas. In this case, 0.2, 0.1, and 0 gas vol% correspond to 15, 8, and 0%, thus 85, 92, and 100% of gas releases, respectively. The ultrasound reading indicates that 108% and 115% of the gas were released during the first 10 minutes and by the end of the sparger operation, while the hand measurements indicate that 92 and 100% of the gas was released during these times.

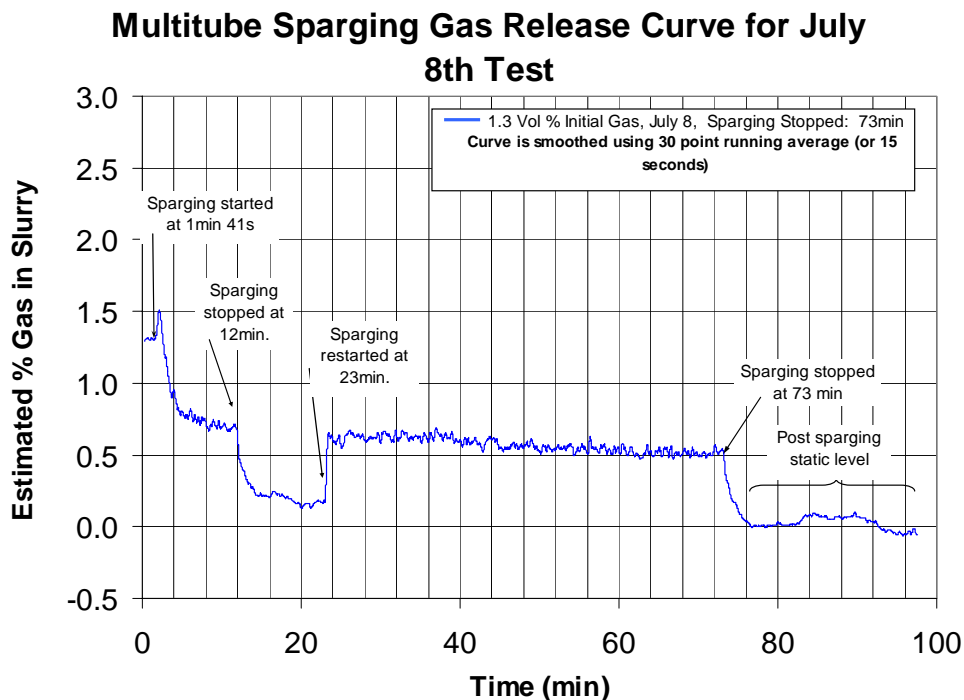


Figure 12.7. Estimated Gas Release for Test Conducted on July 8, 2004

All of the other full-flow tests follow the general behavior of the July 8 test, except for the pause for manual level measurement, as shown in Figure 12.8. The initial portion of the gas release is shown in a

plot of the first 30 minutes of sparging in Figure 12.9. These figures show that the gas volume fraction in each full-flow test drops rapidly and reaches an approximately steady value after about 10 minutes, indicating that most of the releasable gas has left the simulant. All eight tests are in a range of -0.1 vol% to + 0.4 vol% gas at the end of sparger operation within the overall uncertainty of about ± 0.5 vol%.

Figure 12.10 shows the corresponding results for the $\frac{1}{3}$ full sparger air-flow tests (June 11 and 16, 2004). Figure 12.3 and Figure 12.4 also show the surface level trends for the June 11 test. For these smaller air-flow cases, the gas release is slower than that of the full air-flow cases, but they still show the effective removal of the gas by sparging. As stated previously, Figure 12.8 through Figure 12.10 can be viewed as the non-dimensional gas volume fraction by assigning the initial gas volume just before the sparging as 100%.

The long-term portion of the gas release shows no observable long-term holdup trends because of sparging. This is further confirmed by measuring the simulant density of samples, as discussed above.

Five no-gas tests (see the bottom five test cases shown in Table 12.1) showed that

- ultrasound readings fluctuated without specific trends
- sparging reduced the gas volume from the initial gas volume by 0 to 0.3 vol% by ultrasound readings, and 0.1 to 0.6 vol% by the manual measurements.

Because most of these no-gas tests ended with less gas in the simulant, more gas was removed by sparging than gas injected by sparging. This observation also supports the conclusion that there is no long-term gas hold-up within the error of the measurement methods because of a repeated sparger operation.

The results of all sparger tests, including those with zero gas generation and $\frac{1}{3}$ full-scale air flows, are given in Table 12.2. Tests are listed by test identification number with the zero-gas generation tests grouped at the bottom. Tests are further sorted by sparger air-flow rate in the second column. The yield stress (Bingham rheology model), measured from post-test simulant samples, is given in the third column. The yield stress increased from about 28 to 40 Pa over the testing period of June to July 2004, probably from water loss due to evaporation. The pre-sparging, post-sparging, and post-degassing gas volume fractions are listed in the remainder of the table. The three columns headed “DAS Surface Level Measurements” are shown for information only and to illustrate the relationship between sparging duration and gas content. These values were not used to determine gas releases. The last three columns, headed “Hand Surface Level Measurements” are the more valid representation of the observed gas-release behavior. The values shown are referenced to the post-test surface level as the zero-retained gas state, as discussed above.

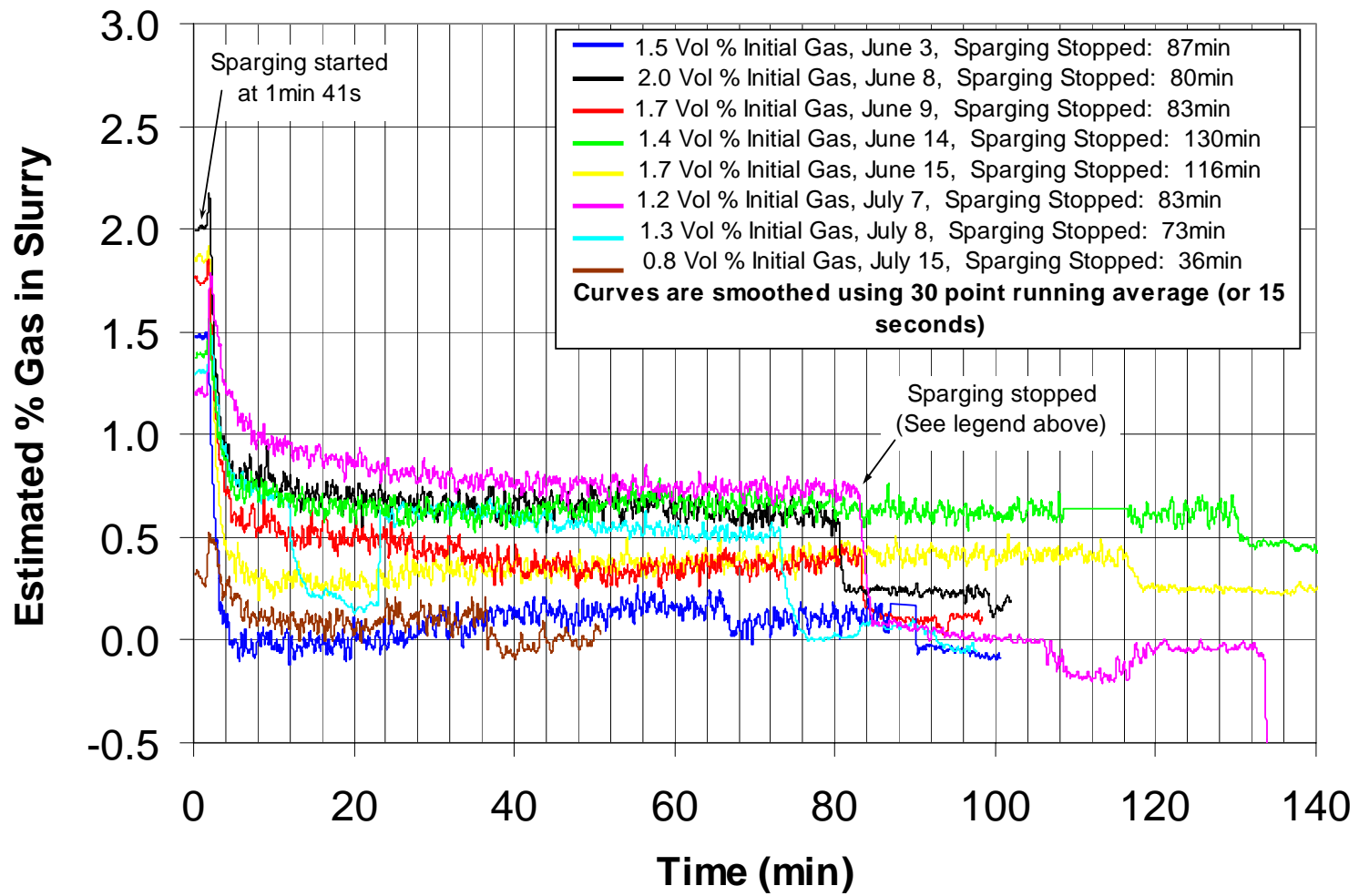


Figure 12.8. Estimated Gas Release While Sparging at Full Air Flow

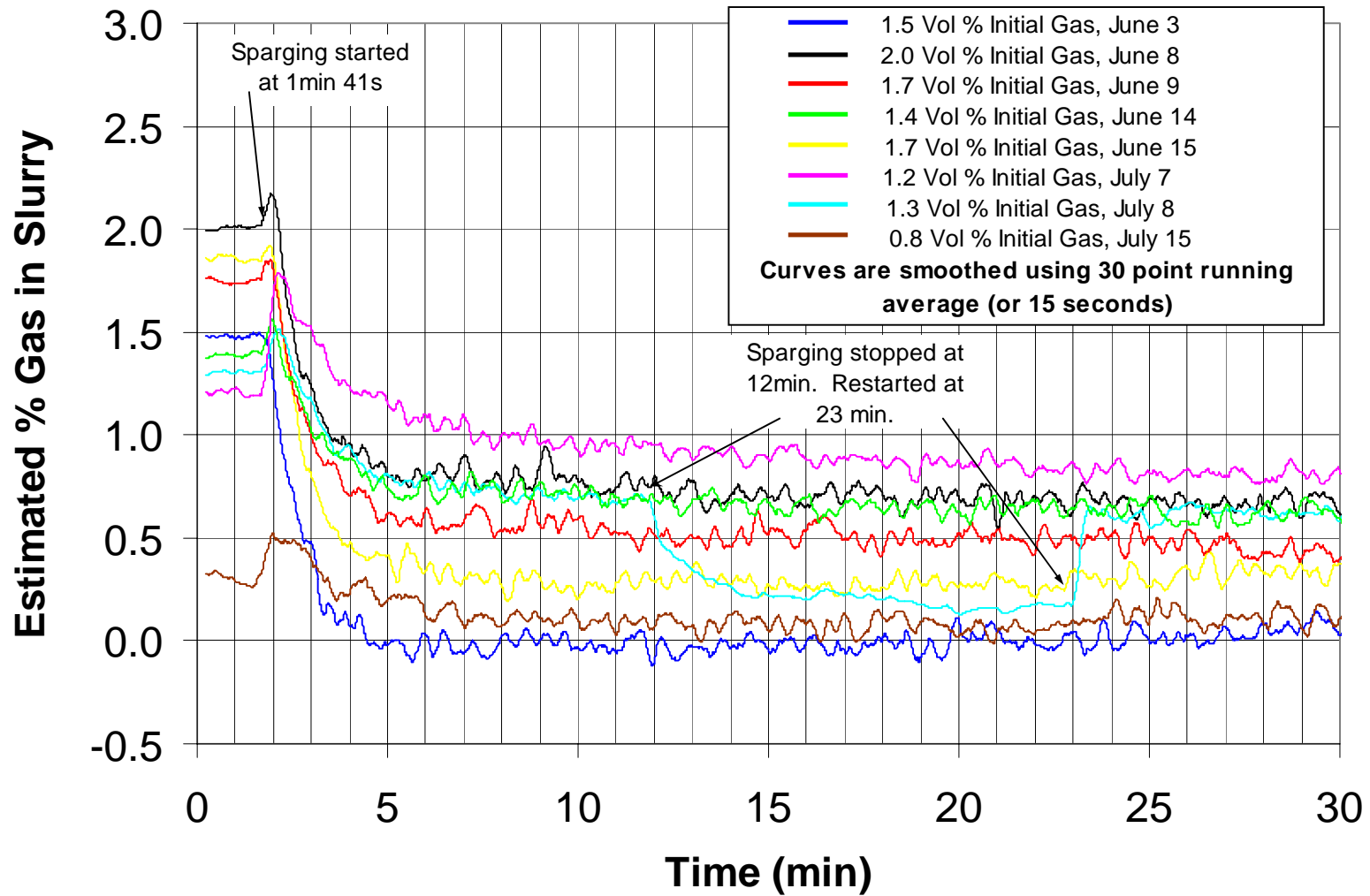


Figure 12.9. Estimated Gas Release While Sparging at Full Air Flow for the First 30 Minutes

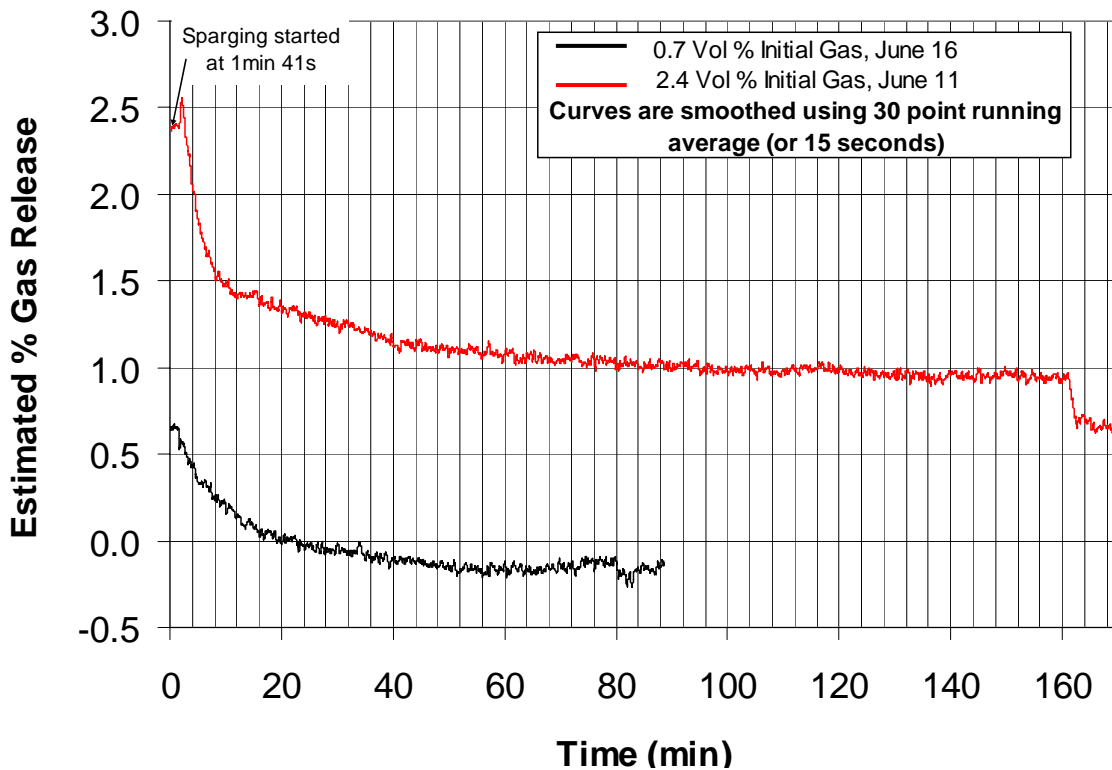


Figure 12.10. Estimated Gas Release While Sparging at $\frac{1}{3}$ of the Full Air Flow

There are some uncertainties and potential errors in these analyses:

- Variability of surface-level measurements with a measuring tape from person to person. It was estimated to be ± 0.2 inch (or ± 0.2 vol%).
- Some ultrasound level probe readings drifted over time.
- Instantaneous jumps in ultrasound level readings are occasionally observed from individual probes as well as all probes at once.

However, with these uncertainties on the measurements and calculations, all of the tests indicate that the multitube sparging is very effective, removing a majority of the gas very rapidly, and most of the gas was released during the sparging operations. There is no evidence of a long-term sparger gas holdup, based on the simulant surface-level changes and simulant density measurements.

Table 12.2. Summary of Multitube Sparging Test Results with Kaolin-Bentonite Simulant to Investigate Gas Release

Test ID	Air-Flow Rate (ACFM)	Average Bingham Plastic Slurry Yield Stress (Pa) ^(d)	DAS Surface-Level Measurements ^{(a), (b)} (Adjusted using DAS weight averaged over time)			Hand Surface-Level Measurements ^{(a), (c)} (Adjusted using DAS weight averaged over time)		
			% Gas Volume (Initial)	% Unreleased Gas (after Sparging)	% Unreleased Gas (after PJM Degas)	% Gas Volume (Initial)	% Unreleased Gas (after Sparging)	% Unreleased Gas (after PJM Degas)
040603	204.2	28	1.4	0.0	0.0	1.5	-0.1	0.0
040608	202.1	29	2.4	0.7	0.0	2.0	0.2	0.0
040609	202.6	301	2.2	0.7	0.0	1.7	0.1	0.0
040707	171.3	355	0.4	-0.4	0.0	1.2	0.0	0.0
040708	170.9	37	1.1	-0.1 (10 min) -0.2 (1 hr)	0.0	1.3	0.1 (10min) 0.0 (1hr)	0.0
040715	206.3	40	0.9	0.0	0.0	0.8	0.0	0.0
040614	203.3	32	1.8	0.9	0.0	1.4	0.4	0.0
040615	206.0	32	1.7	0.3	0.0	1.7	0.2	0.0
040611	68.2	32	2.3	0.9	0.0	2.4	0.7	0.0
040616	57.8	34	1.1	0.3	0.0	0.7	-0.1	0.0
040713 ^(e)	338.1	37	0.0	-0.1 (10 min) 0.0 (38 min)	0.0	0.3	0.0 (10min) 0.1 (38min)	0.0
040622 ^(e)	207.1	33	0.7	0.6	0.0	0.0	-0.1	0.0
040706 ^(e)	175.1	-	0.3	0.3	0.0	0.1	0.0	0.0
040618 ^(e)	68.7	333	0.5	0.2	0.0	0.2	-0.4	0.0
040712 ^(e)	56.7	3772	0.3	0.0	0.0	0.1	-0.1	0.0

(a) Values calculated with the assumption that % gas volume was zero at the end of the test after degassing the clay with multitube PJM overblows.
(b) Gas volume fractions based on DAS surface-level data calculated in the YYMMDD-% ST Gas.xls spreadsheet specific to each experiment date.
(c) Gas volume fractions based on manual surface-level measurements are calculated in the YYMMDD-% ST Gas-Hand.xls spreadsheet specific to each experiment date.
(d) Two samples for were usually taken. The first sample was taken just before adding hydrogen peroxide, and the second was taken at the end of the day (after PJM degassing). If more than one sample was analyzed, an average was calculated and reported.
(e) Table values below bolded solid line represent the “zero gas” (no peroxide added) experiments.

13.0 Results of Acoustic Pressure Measurements During PJM Overblows in the Large Scale 4-PJM Test Setup

The objective of these tests was to measure and report hydro-acoustic pressure data resulting from PJM overblows for the purpose of providing BNI with information to use during plant design in assessing if PJM overblows contribute to structural damage to a PJM mixing tank and associated internal components and equipment.

Overblows occur when the PJM drive air pressure is maintained for a period long enough for the PJM to be emptied of liquid and air to exit the PJM nozzles. The overblow is the result of the sudden expansion of pressurized air during the initial discharge of air through the PJM nozzle. Continual discharge of air from the PJM nozzle is similar to sparging and was not assessed in these tests.

13.1 Materials and Methods

13.1.1 Apparatus

Testing was performed on February 27, 2004, in the 336 building in the Supernatant Liquid Tank (SNT) configured with four pulse jet mixers (PJMs). This configuration is the same as that described in detail in WTP-RPT-081 (Bontha 2003).

13.1.2 Simulant

The kaolin/bentonite simulant described in Section 5.2 was used for these tests.

13.1.3 Method Used

Hydrophones were used to sense acoustic pressure generated by PJM overblows. Hydrophones are underwater microphones, the standard sensors used to measure underwater acoustic pressure. These hydrophones were mounted from existing apparatus intended to hold velocity probes during the non-Newtonian cavern tests (Figure 13.1). The hydrophones were mounted at the bottom of 20-ft long, 2-in., Sch.-40 PVC pipe masts. Two hydrophones, Bruel & Kjaer (B&K) model 8104 hydrophones, were used to obtain the data and were positioned at several of the designated locations indicated in Figure 13.1.

The hydrophones used were calibrated according to the manufacturer's manual. Data from this activity were documented in LRB: BNW 14500. A B&K hydrophone calibrator—Type 4229—was used and was calibrated by the manufacturer before use, but PNWD did not evaluate the B&K calibration program. The calibrator produces a tone at $251.2 \text{ Hz} \pm 0.1\%$ at 162 dB re 1 μPa .

Additional, significant equipment used included 2 ea. B&K Model 2636 charge amplifiers and a Sony Model PC216AC 16 channel digital audio tape (DAT) recorder. Sound pressure was sensed by the hydrophones, amplified by the charge amplifiers, and recorded on the DAT recorder as a digitized voltage as a function of time. The system signal was scaled at 1 Pascal (PA) per milliVolt (mV).

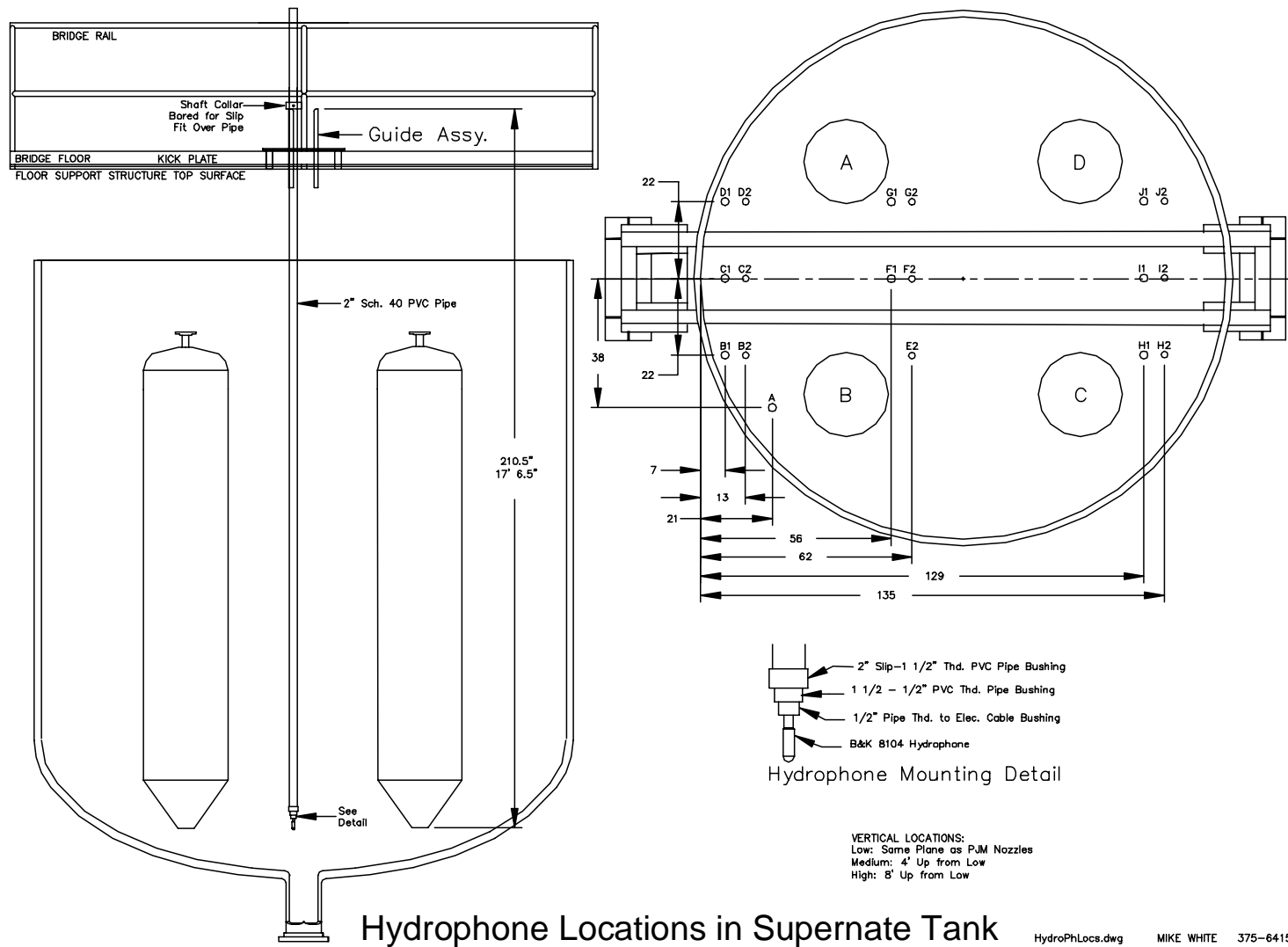


Figure 13.1. Hydrophone Locations and Designation in the Supernatant Tank

The PJM drive cycle, including the application of the drive pressure (preset using a pressure regulator), was controlled by the AEA-supplied PRESCON II controller.

13.1.4 Measurement Locations

The measurement locations were selected based on the location of preexisting velocity probe mounts and input from BNI engineering. The majority of the measurements were made in horizontal planes at tank elevations of 1.1 ft (the plane of the nozzle discharge) and 5.1 ft. The tank zero elevation is the bottom center interior of the tank, and the elevation of the nozzle discharge was 1.1 ft. At locations A and H1, measurements were made only at an elevation of 2.6 ft, 1.5 ft above the horizontal plane of the nozzle discharge. This was to ensure that the hydrophones did not strike the elliptical floor of the tank.

The vertical position of the hydrophone was determined by measuring the distance from the hydrophone sensor to the top of the instrument holder. This distance is referred to as the depth. The tank elevation is referenced to the interior bottom center (zero datum) of the tank. The elevation of the top of the instrument holders was 18.6 ft.

13.1.5 Acoustic Pressure Generation

The acoustic events were generated by setting the Prescon controller parameters to overblow PJM B only. Four different Prescon drive pressures were used: 200, 300, 450, and 500 kPa. At each drive pressure, the drive time was experimentally incremented until the drive time was achieved that resulted in a very small (initialization of) overblow. Subsequently an additional, 1.5 seconds were added to the drive time that resulted in initialization of an overblow. This additional time was added to ensure a significant, consistent period of overblow.

13.1.6 Recorded Data

Two hydrophones, designated HP1 and HP2, were used to record all the measurements. The hydrophones were moved to different elevations and locations to obtain additional measurements within the tank relative to the PJM being operated. Each overblow test generated a new data file. Table 13.1 lists the data files and the corresponding test configuration.

The two channels of data were recorded on DAT tape at 48,000 samples per second, at 8-bit resolution, over a period of 30 seconds, encompassing the time period of each overblow test. In most cases, three overblows were repeated for each set of Prescon parameters, sensor location, and sensor elevation.

13.1.7 Data Processing

Raw data were edited down to cover a time period of 6.5 seconds, containing the significant pressure data of the overblow event. These post-processed data were saved in comma-delimited ASCII format (.csv). Each dataset of each of the csv files consists of three values: time, HP1 pressure, HP2 pressure.

Table 13.1. Data File Names and Corresponding Hydrophone Locations and Associated Prescon Settings

Name of Data File Saved to DAT	Hydrophone No. 1 (HP1)	Hydrophone No. 2 (HP2)	Tank Elev. of Measurement Location (ft)	Depth of Measurement Below Instrument Holder (ft)	Drive Pressure (kPa)	Duration Drive Pressure Applied (sec)
ID23TIME.csv	E2	G1	1.1	17.5	500	13.5
ID24TIME.csv	E2	G1	1.1	17.5	500	13.5
ID25TIME.csv	E2	G1	1.1	17.5	500	13.5
ID28TIME.csv	E2	G1	1.1	17.5	300	18.0
ID29TIME.csv	E2	G1	1.1	17.5	300	18.0
ID30TIME.csv	E2	G1	1.1	17.5	300	18.0
ID32TIME.csv	E2	G1	1.1	17.5	450	14.1
ID33TIME.csv	E2	G1	1.1	17.5	450	14.1
ID38TIME.csv	E2	G1	1.1	17.5	200	22.5
ID39TIME.csv	E2	G1	1.1	17.5	200	22.5
ID40TIME.csv	E2	G1	1.1	17.5	200	22.5
ID41TIME.csv	E2	G1	5.1	13.5	200	22.5
ID42TIME.csv	E2	G1	5.1	13.5	200	22.5
ID43TIME.csv	E2	G1	5.1	13.5	200	22.5
ID44TIME.csv	E2	G1	5.1	13.5	200	18.0
ID45TIME.csv	E2	G1	5.1	13.5	300	18.0
ID46TIME.csv	E2	G1	5.1	13.5	300	18.0
ID47TIME.csv	E2	G1	5.1	13.5	450	14.1
ID48TIME.csv	E2	G1	5.1	13.5	450	14.1
ID49TIME.csv	E2	G1	5.1	13.5	450	14.1
ID50TIME.csv	E2	G1	5.1	13.5	500	13.5
ID51TIME.csv	E2	G1	5.1	13.5	500	13.5
ID52TIME.csv	E2	G1	5.1	13.5	500	13.5
ID53TIME.csv	E2	G1	9.1	9.5	500	13.5
ID54TIME.csv	E2	G1	9.1	9.5	500	13.5
ID55TIME.csv	E2	G1	9.1	9.5	500	13.5
ID56TIME.csv	E2	G1	9.1	9.5	450	14.1
ID57TIME.csv	E2	G1	9.1	9.5	450	14.1
ID59TIME.csv	H1	G1	2.6	16	500	13.5
ID60TIME.csv	H1	G1	2.6	16	500	13.5
ID61TIME.csv	H1	G1	2.6	16	500	13.5

Radial distance from PJM B centerline of measurement locations: E2 = 1.9 ft, G1 = 4.8 ft, H1 = 7.3 ft

13.2 Results and Discussion

The data files listed in Table 13.1 were transmitted to BNI engineering at the completion of testing. The measured pressures as a function of time are presented in Figure 13.2 through Figure 13.6 for five test runs.

During all the overblow tests, no pressures in excess of 13kPa (1.9 PSIG) were recorded. Typical peak pressures ranged from a few to several thousand Pascals. The largest resulting pressure was measured for a PJM drive pressure of 500 kPa at location E2 (1.9 ft from the centerline of PJM B), the nearest location to the PJM discharge from which measurements were taken. No attempt to determine the structural damage potential of these pressures is made herein.

Pressure measurements as a function of time, at a measured radius of 1.9 ft from the PJM centerline (E2), and an elevation of 1.1 ft (discharge nozzle elevation), for a 500 kPa drive pressure are presented in Figure 13.2 through Figure 13.4. This test case produced the highest pressures measured with the hydrophones. The three figures are presented as examples of the repeatability of the pressure measurements.

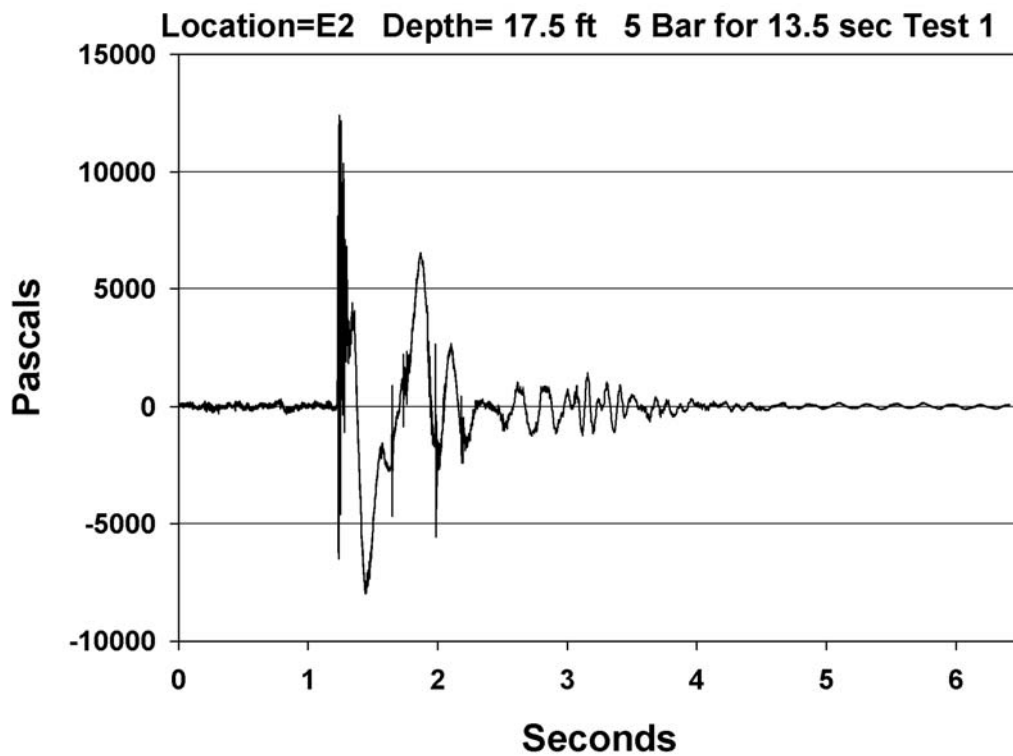


Figure 13.2. Pressure Versus Time for PJM Overblow with 500 kPa (5-bar) Drive Pressure. Hydrophone measurements were taken 1.9 ft from PJM centerline at the elevation of the PJM discharge.

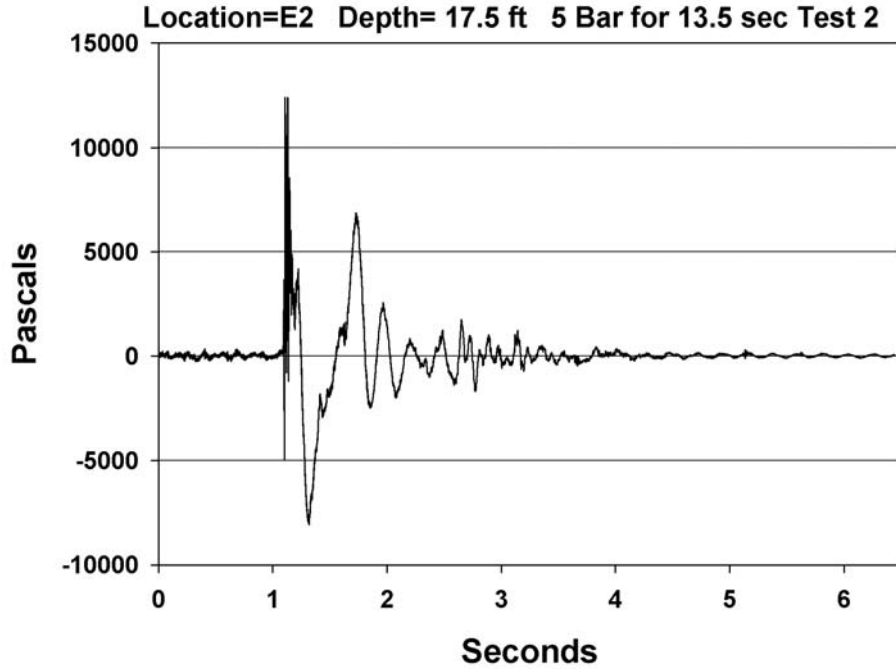


Figure 13.3. Pressure Versus Time for PJM Overblow with 500 kPa (5-bar) Drive Pressure. Hydrophone measurements were taken 1.9 ft from PJM centerline at the elevation of the PJM discharge.

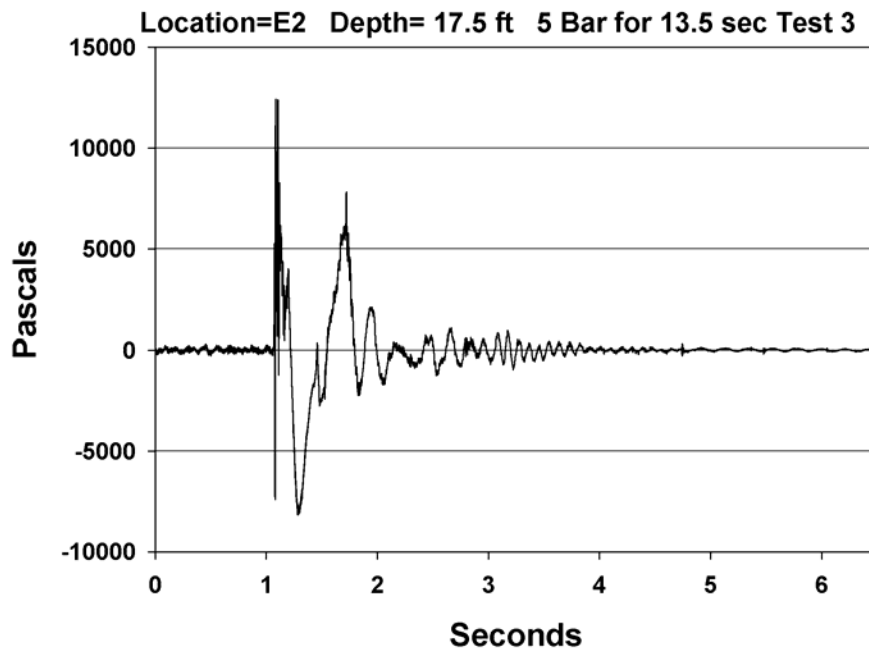


Figure 13.4. Pressure Versus Time for PJM Overblow with 500 kPa (5-bar) Drive Pressure. Hydrophone measurements were taken 1.9 ft from PJM centerline at the elevation of the PJM discharge.

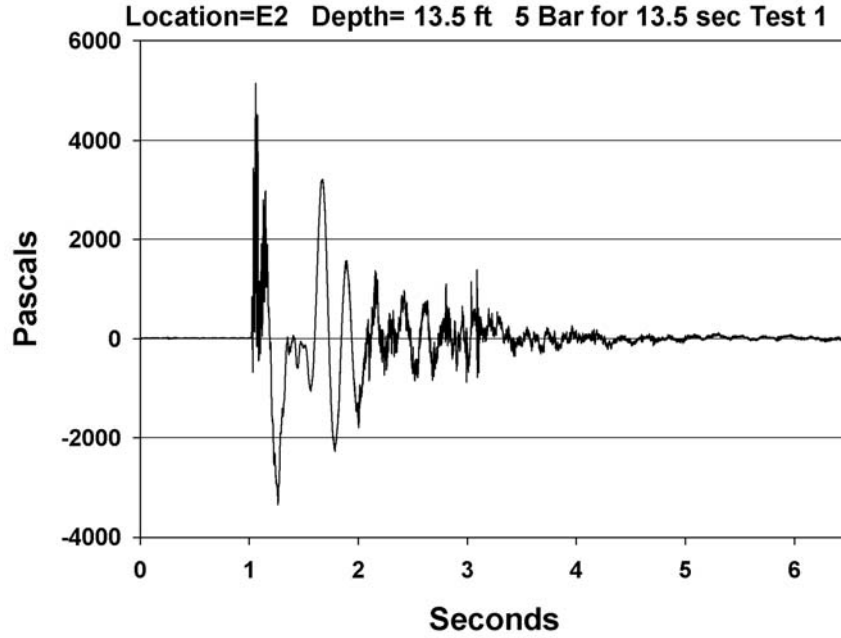


Figure 13.5. Pressure Versus Time for PJM Overblow with 500 kPa (5-bar) Drive Pressure. Hydrophone measurements were taken 1.9 ft from PJM centerline and 4 ft above the PJM discharge elevation.

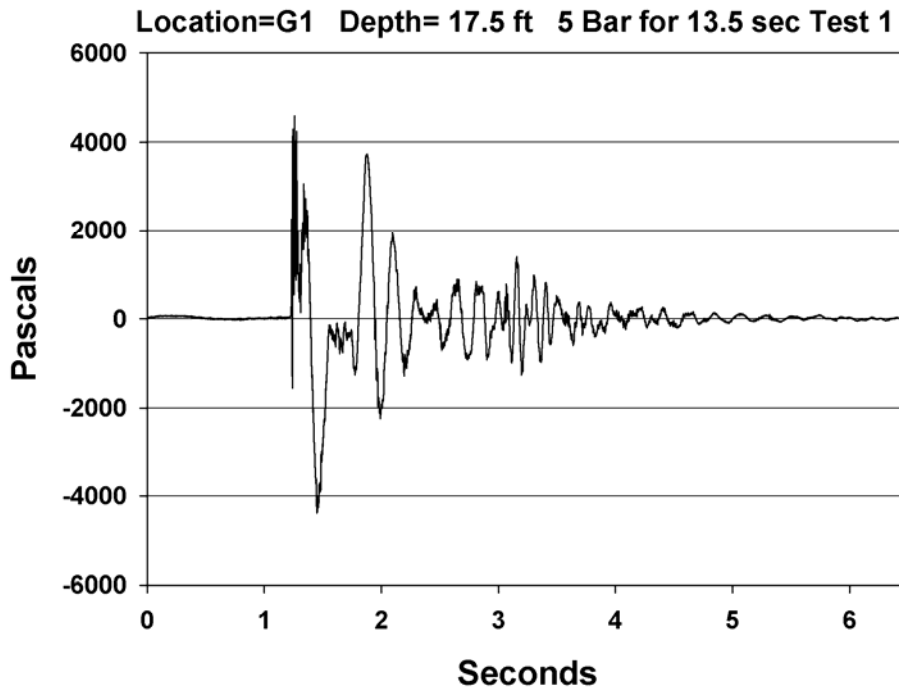


Figure 13.6. Pressure Versus Time for PJM Overblow with 500 kPa (5-bar) Drive Pressure. Hydrophone measurements were taken 4.8 ft from PJM centerline and 4 ft above the PJM discharge elevation.

Figure 13.5 provides comparative pressure measurements obtained at a radius of 1.9 ft and an elevation 4 ft above those presented in Figure 13.2 through Figure 13.4. For a drive pressure of 500 kPa, measurements taken 4 ft above the nozzles discharge, at a radius of 1.9 ft, were approximately 60% less than those measured in the plane of the nozzle at the same radius.

Figure 13.6 provides comparative pressure measurements obtained at an elevation of 1.1 ft and a radial distance of 4.8 ft from the PJM centerline. For a drive pressure of 500 kPa, the hydrophone measurements indicated that an increase in radial distance of 38 in. from the PJM, in the plane of the nozzle, reduced the peak pressure by 65%.

14.0 Discussion and Conclusions

Due to the mathematical complexities of multi-phase fluid dynamics, scale-up or scale-down of sparging systems will likely produce different results. For this reason, large-scale tests were performed at a scale comparable to the WTP design. The large-scale tests performed in support of the PJM hybrid mixing concept can be interpreted to produce the following picture of the fluid mechanics of sparging of non-Newtonian fluids. First, ZOI measurements performed with surface tracers and a video imaging technique (see Section 6.0) correlate well with measurements performed in the subsurface using ultrasonic techniques (see Section 7.0) and PIT tags (see Section 8.0). From the ultrasonic measurements, the ZOI region appears to begin slightly below the sparger nozzle. These data indicate that the ZOI region below the sparge nozzle is linear and follows the correlation shown in Figure 14.1. Ultrasonic measurements also indicate that the ZOI boundary for all flow rates intersects at a point 16 inches above the sparger nozzle and 28 inches radial distance from the sparge tube (see Figure 7.3). This suggests that the tank wall is having a significant limiting impact on the ZOI boundary in this area as air flow increases. Using three spatial points, including surface tracer correlations as a function of air flow at a nozzle depth of 120 inches, ZOI boundary below the sparger nozzle as a function of air flow, and the intersection point 16 inches above the sparger nozzle and 28 inches radial distance from the sparge tube, the ZOI boundary can be estimated over the air-flow range of 5 to 40 ACFM and a nozzle submergence depth of 0 to 120 inches by the set of equations shown below. Additionally, the ROB can be estimated by using the surface tracer correlation between ZOI and ROB at the same air-flow rate.

$$D_{ZOI} = a(z - c)^b \quad (14.1)$$

$$D_{ROB} = \frac{D_{ZOI}}{3} \quad (14.2)$$

$$a = \frac{56}{(16 - c)^b} \quad (14.3)$$

$$b = \frac{\ln\left(\frac{17}{28} Q_{air}^{0.34}\right)}{\ln\left(\frac{120 - c}{16 - c}\right)} \quad (14.4)$$

$$c = -0.188Q_{air} + 0.0459 \quad (14.5)$$

where D_{ROB} = ROB diameter (in)
 D_{ZOI} = ZOI diameter (in)
 Q_{air} = actual volumetric flow rate of the air in slurry at the end of the sparge tube (ft³/min).
 a = Fitting parameter (in^{1-b})
 b = Fitting parameter
 c = Fitting parameter (in.).

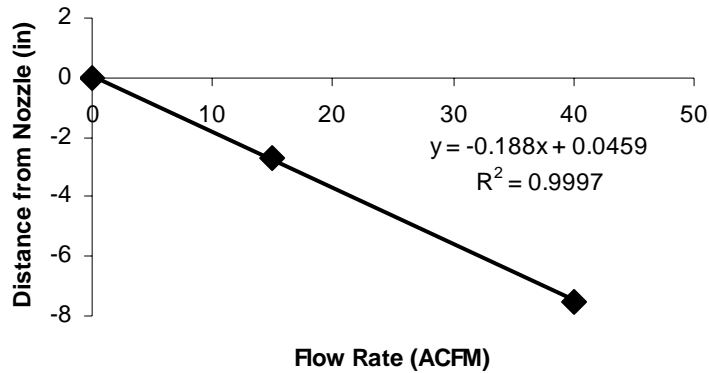


Figure 14.1. ZOI Boundary Below Sparger Nozzle as a Function of Air-Flow Rate

These equations produce the ZOI and ROB boundaries shown in Figure 14.2. Note that this fluid flow pattern is driven entirely by buoyant forces caused by the density difference between sparged air and the test fluid. Tracer tests described in Section 10.0 indicate that the sparging flow patterns consist of four regions, a transition region from ZOI to ROB, ROB, transition from ROB to ZOI, and ZOI. When tracer is injected next to the sparge tube near the nozzle outlet, the tracer reaches the surface quickly on the order of seconds. This indicates a significant upflow because of rising bubbles near the sparge tube. When tracer is added near the sparge tube on the fluid surface, the tracer appears near the outer ZOI boundary relatively quickly, indicating velocities in this region on the order of 20 mm/sec. When tracer is added near the outer ZOI boundary on the surface, the tracer appears near the midpoint of the sparger relatively quickly, indicating velocities in this region on the order of 10 mm/sec. However, the tracer appears near the sparge tube bottom several minutes later, indicating velocities in this region on the order of 3 mm/sec.

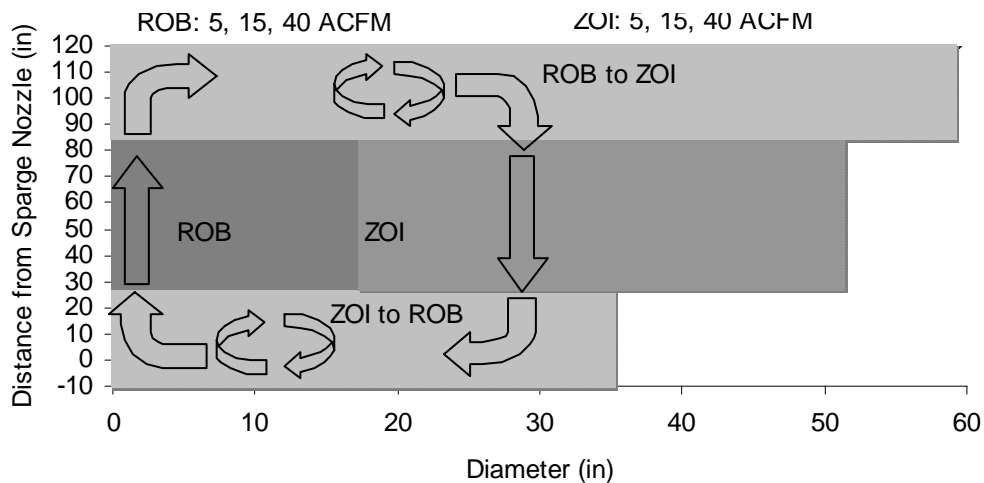


Figure 14.2. Summary Diagram of Non-Newtonian Sparger Boundaries and Flow Patterns

The transition region ZOI to ROB appears to consist of a significant recirculation zone that lengthens the trajectory of the tracer and lowers the overall tracer velocity between two points. This can be seen by the relatively large delay between the tracer first appearing near the sparge tube bottom and the arrival of the peak tracer concentration several minutes later. The source of the recirculation zones is likely the rotating flow that occurs in the transition regions, ZOI to ROB and ROB to ZOI. These flow patterns are illustrated in Figure 14.2.

Ultrasonic velocity probe data and measurements of surface tracer positions discussed in Sections 7.0 and 6.0, respectively, provide insight into the establishment of the flow patterns due to sparging. These tests show that the flow on the surface in the ROB to ZOI region and subsurface in the ZOI region is quickly established after the sparging system is started. Consequently, the full flow circulation patterns appear to begin nearly simultaneously with the start of air flow.

Gas retention and release experiments with a multi-tube sparge system were performed. These tests indicate that the multi-tube sparging is very effective, removing a majority of the gas very rapidly, and most of the gas was released during the sparging operations. There is no evidence of a long-term sparger gas holdup, based on the simulant surface level changes and simulant density measurements.

15.0 References

- Bamberger JA, and MS Greenwood. 2001. *Development of a Density Sensor for In-Line Real-Time Process Control and Monitoring of Slurries during Radioactive Waste Retrieval and Transport Operations at DOE Sites*. PNNL-13719, Pacific Northwest National Laboratory, Richland, WA.
- Bamberger JA, and MS Greenwood. 2004a. *Measuring fluid and slurry density and solids concentration noninvasively*. Ultrasonics (42) 563-567. PNNL-SA-40035, Pacific Northwest National Laboratory, Richland, WA.
- Bamberger JA, and MS Greenwood. 2004b. *Using ultrasonic attenuation to monitor slurry mixing in real time*. Ultrasonics (42) 145-148. PNNL-SA-40033, Pacific Northwest National Laboratory, Richland, WA.
- Bamberger JA, MS Greenwood, and HK Kytomaa. 1998. *Ultrasonic Characterization of Slurry Density and Particle Size*. FEDSM1998-5075, American Society of Mechanical Engineers, New York, NY.
- Bamberger JA, MS Greenwood, and K Witwer. 2001. "Development of an Ultrasonic Sensor to Measure Density of Radioactive Waste Slurries during Pipeline Transport." In: *ANS 9th International Topical Meeting Robotics and Remote Systems*, Seattle, Washington, March 4-8, 2001. PNNL-SA-34125, Pacific Northwest National Laboratory, Richland, WA.
- Bamberger, JA, HK Kytomaa, and MS Greenwood. 1998. "Slurry Ultrasonic Particle Size and Concentration Characterization." In: *Science and Technology for Disposal of Radioactive Tank Wastes*. WW Schulz and NJ Lombardo, eds. Plenum Press, New York, NY. PNNL-SA-29277, Pacific Northwest National Laboratory, Richland, WA.
- Bontha JM. 2003. *Large Scale PJM Test Data for Fluent Validation*. WTP-RPT-081, PNWD-3303, Battelle—Pacific Northwest Division, Richland, WA.
- Greenwood MS, JL Mai, and MS Good. 1993. "Attenuation measurements of ultrasound in a kaolin-water slurry: A linear dependence upon frequency." *J. Acoust. Soc. Am.* 94(2), Pt. 1, August.
- Greenwood, MS, JR Skorpik, and JA Bamberger. 1998. "On-line Sensor to Measure the Density of a Liquid or Slurry." In: *Science and Technology for Disposal of Radioactive Tank Wastes*. WW Schulz and NJ Lombardo, eds. Plenum Press, New York, NY. PNNL-SA-29278, Pacific Northwest National Laboratory, Richland, WA.
- Perry RH, and DW Green. 1977. *Perry's Chemical Engineer's Handbook*. McGraw-Hill, New York, NY.
- Poloski AP, PA Meyer, LK Jagoda, and PR Hrma. 2004. *Non-newtonian Slurry Simulant Development and Selection for Pulse Jet Mixer Testing*. WTP-RPT-111 Rev 0, PNWD-3495, Battelle—Pacific Northwest Division, Richland, WA.
- Seinfeld JH, and SN Pandis. 1998. *Atmospheric Chemistry and Physics, 2nd ed.* John Wiley & Sons, Inc., New York, NY.

Tilton JN, and TWF Russell. 1982. "Designing Gas-Sparged Vessels for Mass Transfer." *Chemical Engineering* 89(24):61-68.

Workman J, Jr, DJ Veltkamp, S Doherty, BB Anderson, KE Creasy, M Koch, JF Tatera, AL Robinson, L Bond, LW Burgess, GN Bokerman, AH Ullman., GP Darsey, F Mozayeni, JA Bamberger, and MS Greenwood. 1999. "Process Analytical Chemistry." *Analytical Chemistry* 71(12):121R-180R.

Appendix A

Surface Tension and Yield Stress Measurements on Kaolin/Bentonite Clay Simulant and Simulated Pre-Treated AZ-101 High Level Waste Slurries

Appendix A: Surface Tension and Yield Stress Measurements on Kaolin/Bentonite Clay Simulant and Simulated Pre-Treated AZ-101 High Level Waste Slurries

**L. A. Snow
A. P. Poloski
B. J. Cook**

Introduction

The surface tension and yield stress of various non-Newtonian WTP simulant slurries used for PJM testing was measured. Surface tension is a significant property for understanding the behavior of bubbles and aerosols in WTP flow sheet slurry systems. Bubble detachment when sparging, bubble coalescence during mixing, and aerosol generation are all a function of surface tension between the gas and slurry phases. Non-Newtonian slurries possess a yield strength that competes with surface tension during typical measurement techniques. This task will determine a correlation of surface tension in the interstitial fluid of the Kaolin/Bentonite clay and simulated AZ-101 high level waste (HLW) slurries. Slurry solid phases were added in known amounts to the interstitial fluid and correlations between surface tension and solids loading and yield stress and solids loading were obtained. The measurements of surface tension are only valid in the absence of yield stress so we tested over a range of solids concentrations to get measurements with little to no yield stress. The correlation can be used to extrapolate surface tension to higher solids loadings.

Experimental

Determination of Solids Concentration

For each slurry, six vials were pre-weighed. Approximately 10 grams of slurry was placed in each vial. The vial plus sample was then weighed, and the sample mass determined by difference. The lids were removed from the vials, and all samples were placed in an oven to dry at 80°C. After one day, the temperature was raised to 100°C. The samples were weighed daily until the sample mass was constant. The weight percent solids were then calculated as the residual mass divided by the initial sample mass multiplied by 100%. A solids concentration of 29.0 wt% was determined for the Kaolin/Bentonite slurry. The simulated HLW slurry was determined to contain 20.9 wt% solids.

Sample Preparation

Samples of the two slurries were then centrifuged and the supernatant liquid removed. Supernatant liquid was added to the slurries in varying amounts in order to make several samples with different solids loading. Sample names and total weight percent solids are shown in Table A.1 for the Kaolin/Bentonite slurry and Table A.2 for the simulated HLW slurry.

Surface Tension Measurement

Surface tension measurements were made on all samples using a Kruss K12 tensiometer. Once a week, a calibration was performed by doing a balance adjustment on the instrument. The balance adjustment serves to adjust the balance which is installed in the headpiece of the measuring unit. A performance check of the instrument was conducted prior to performing the first measurement each day and after the final sample measured each day. The performance check was conducted using DI water which has a surface tension of 72.75 mN/m at 20°C (Lide, <http://www.amazon.com/exec/obidos/ASIN/0849304687/weisstein-20> 1991). The tensiometer performance check was considered acceptable if the measured value for water was 72.8 ± 0.3 mN/m.

The Wilhelmy Plate method was used to measure surface tension. This method consists of a thin plate made of roughened platinum. It is assumed that all liquids totally wet roughened platinum, so the contact angle θ is assumed to be zero. Consequently, the surface tension force acts directly downward on the plate. The plate is suspended from a balance, and zeroed while suspended in the air. The sample is raised until it is brought into contact with the plate. The plate is then pulled into the sample by the surface tension force. The force (f_s) applied to the plate from above is then increased to bring the bottom of the plate level with the surface of the liquid. Since the measuring procedure is static, the plate can be left at this level and surface tension measured continuously for any amount of time. The surface tension (γ) is calculated from the force measurement as shown in equation 1 (Thiessen, 2000):

$$\gamma = \frac{f_s \cos \theta}{[2(l + t)]} \quad \text{Eq. 1}$$

where l is the length of the plate (19.9 mm), t is the thickness (0.2 mm) and f_s is the surface tension force. The contact angle θ is assumed to be zero. A schematic is shown in Figure A.1.

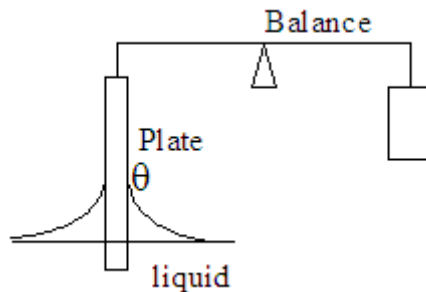


Figure A.1. Schematic of Wilhelmy Plate Method

Prior to each measurement, the Pt plate was rinsed with water and acetone and dried in a Bunsen burner's flame until it turned red. The sample containers were rinsed with deionized water and dried with clean compressed air. Each day measurements were made, the surface tension of deionized water was measured three times for five minutes each, both before and after the samples were measured. Samples were run for 2, 5, 10, or 15 minutes. The software was set up to take 1,000 data points every 5 minutes.

Yield Stress Measurement

Yield stress measurements were made with a Thermal Analysis AR 2000 Rheometer utilizing a 15 mm cup with a 14 mm diameter and 42 mm high, recessed end bob. The measurement temperature was 25°C. The run program for thicker samples was programmed for a linear increase in shear rate (1/s) from 0 to 1000 s⁻¹ over a 5 minute period, followed by a 1 minute hold at 1000 s⁻¹ and then by a 1000 to 0 s⁻¹

rate reduction over 5 minutes. The maximum shear rate and run times were reduced for the thinner samples as needed to record only the linear section of the curve. An anodized aluminum cup and bob were used for clay samples and a stainless steel cup and bob were used for the simulated HLW samples. The data was fit to a Bingham model to determine the yield stress. In both slurries, yield stress decreased with decreasing solids content, becoming nearly zero for 5 wt% solids. Therefore, samples containing less than 5 wt% solids were considered to have a yield stress value of zero, and yield stress measurements were not made on these samples.

Results and Discussion

A stock solution of Kaolin/Bentonite clay slurry containing approximately 28 wt% solids and a stock solution of simulated HLW slurry containing approximately 20 wt% solids were obtained. In order to accurately determine the weight percent solids of both slurries, six sub samples of each slurry were removed from the stock solution and dried in an oven. The value of percent solids was determined for each of the six samples for each slurry. The average value for each slurry was calculated. The average values obtained were 29.0 ± 0.03 wt% solids for the clay slurry and 20.9 ± 0.03 wt% solids for the simulated HLW slurry. Sub samples of both slurries were then removed from the stock solutions and centrifuged. The liquid was removed from the solids. For the Kaolin/Bentonite clay slurry, thirteen samples of varying solids concentrations were made by adding the liquid in varying proportions to the slurry. For the simulated HLW slurry, ten samples of varying solids concentrations were made by adding the liquid in varying proportions to the slurry. For each slurry, two additional samples were also prepared, one of the undiluted slurries and one sample of the liquid from each of the slurries.

Yield stress and surface tension will both contribute to the force required to pull the Wilhelmy plate from the slurry. PNWD therefore considered means to separate these effects as now described. Yield stress measurements were made on eleven samples of the clay slurry and eight samples of the simulated HLW slurry. Figures A.2 and A.3 show the yield stress as a function of weight percent solids for the Kaolin/Bentonite Clay and simulated HLW slurry, respectively. A line was fit to each set of data and is shown in the plots. For the Kaolin/Bentonite Clay, the yield stress begins to rise above zero at approximately 12.5 wt% solids. For the simulated HLW slurry, the yield stress begins to rise at approximately 10 wt% solids.

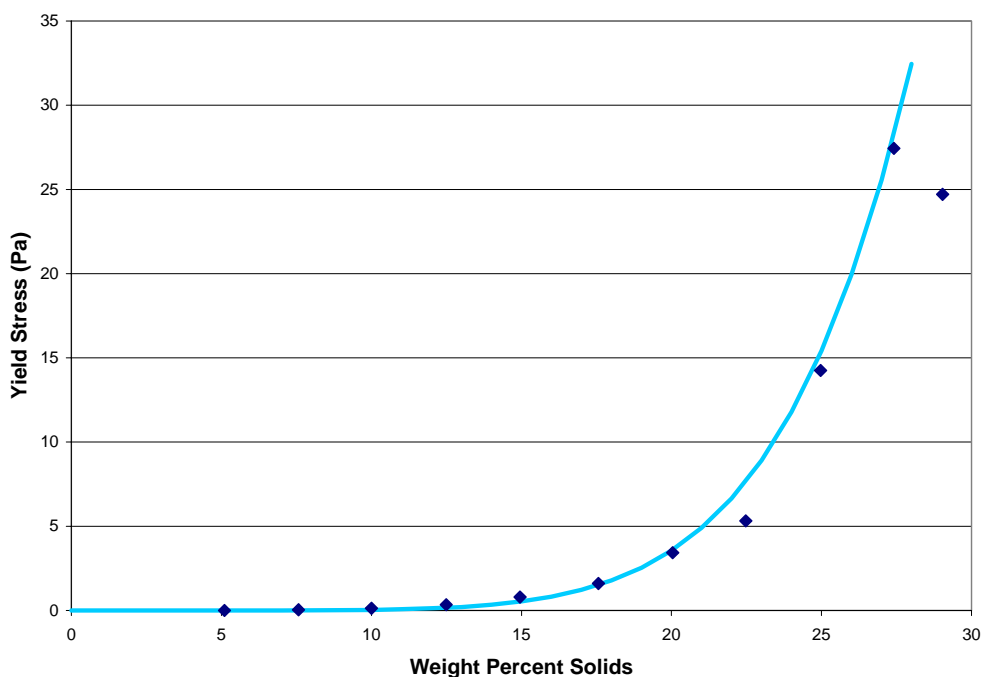


Figure A.2. Correlation Between Bingham Yield Stress and Kaolin/Bentonite Clay Slurry Concentration at Ambient Temperature

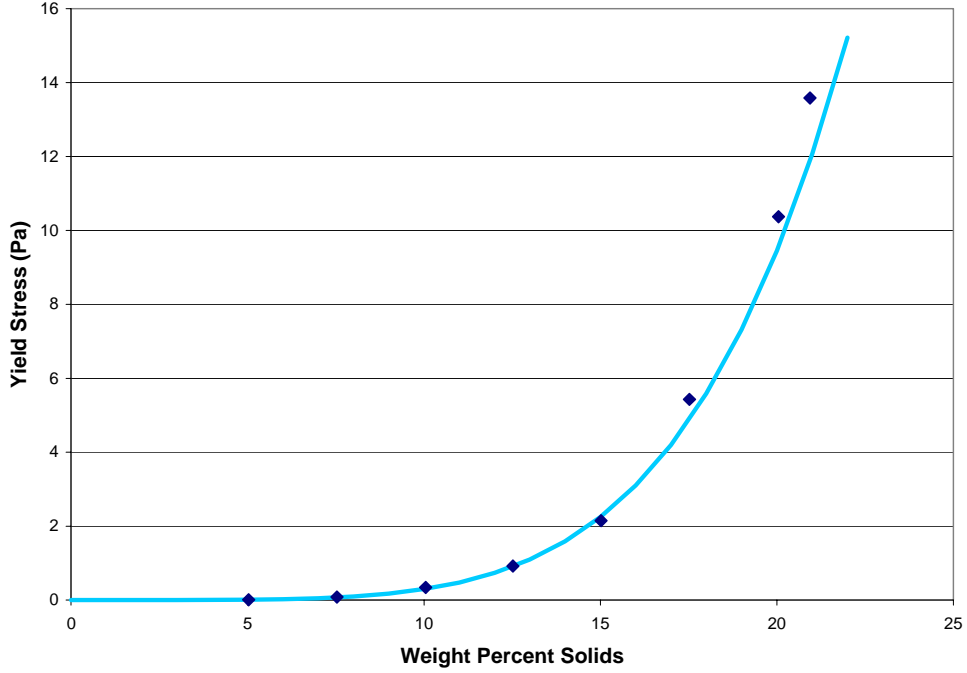


Figure A.3. Correlation Between Bingham Yield Stress and Simulated HLW Slurry Concentration at Ambient Temperature

From the Wilhelmy Plate method used to measure surface tension, we have the equation relating surface tension to surface tension force (Eq. 1). The contact angle θ is assumed to be zero, so the equation becomes:

$$f_s = 2 \cdot (l + t) \cdot \gamma \quad \text{Eq. 2}$$

The yield stress force is the yield stress multiplied by the surface area of the portion of the plate that is submerged in the sample:

$$f_y = \tau \cdot [(l \cdot t) + (2 \cdot l \cdot z)] \quad \text{Eq. 3}$$

where τ is the yield stress and z is the height to which the plate is submerged in the slurry. The value of z is difficult to measure precisely. An estimate of 0.5 ± 0.2 mm will be used for the value of z .

Then the ratio of the yield stress force to the surface tension force is:

$$ratio = \frac{f_y}{f_s} = \frac{\tau [(l \cdot t) + (2 \cdot l \cdot z)]}{2 \cdot (l + t) \cdot \gamma} \quad \text{Eq. 4}$$

Since $l \gg t$, we can approximate as:

$$ratio = \frac{\tau \cdot [t + (2 \cdot z)]}{2\gamma} \quad \text{Eq. 5}$$

We want to measure the point at which the surface tension force dominates over the yield stress force. So a ratio of 0.01 (1:100 yield stress to surface tension) will be used. Using a value of 72.8 mN/m for the surface tension, with a ratio of 0.01, and z equal to 0.5 mm, $\tau = 1.2$ Pa. Therefore, for a ratio of 0.01, we want to consider only measurements with a yield stress lower than ~ 1.2 Pa. This value of yield stress occurs above about 15 wt% solids for the clay and above about 12 wt% solids for the simulated HLW. This corresponds to the point where surface tension apparently begins to rise for both slurries because the yield stress starts to contribute to the force required to pull the plate from the slurry.

As the solids content increases, the samples become non-Newtonian. At this point, the measured values of surface tension apparently begin to increase rapidly with increasing solids content, and the measured value is actually a combination of yield stress and surface tension for these samples. By using an equation for the total force of the system, the measured values of yield stress and surface tension can be used to calculate the actual value of surface tension for these non-Newtonian samples. The total force of the system can be measured by the sum of the surface tension force and the yield stress force:

$$f_t = f_s + f_y \quad \text{Eq. 6}$$

Substituting the functions for each component into equation 6, we can get an equation to calculate the actual surface tension:

$$2 \cdot (l + t) \cdot \gamma_t = 2 \cdot (l + t) \cdot \gamma_s + \tau \cdot [(l \cdot t) + (2 \cdot l \cdot z)] \quad \text{Eq. 7}$$

where γ_t is the measured value of surface tension, and γ_s is the actual value of surface tension.

Solving for the actual surface tension:

$$\gamma_s = \frac{2 \cdot (l + t) \cdot \gamma_t - \tau \cdot [(l \cdot t) + (2 \cdot l \cdot z)]}{2 \cdot (l + t)} \quad \text{Eq. 8}$$

The surface tension of the Kaolin/Bentonite clay slurry was measured for the thirteen diluted samples, along with a sample of the undiluted slurry and a sample of the liquid from the slurry. Five measurements were made on each sample. The results from each measurement, as well as the average surface tension and the standard deviation, are shown in Table A.1. The average surface tension values are plotted in Figure A.4. Error bars represent a single standard deviation. Samples containing less than 15 wt% solids had measured surface tension values of 72.2 – 73.0 mN/m. As determined above, the samples become non-Newtonian above 15 wt% solids. The measured values of surface tension in samples having more than 15 wt% solids are actually a combination of yield stress and surface tension.

Equation 8 was used to calculate the actual values of surface tension. Values were not calculated for the first four samples because yield stress measurements were not made on those samples. The calculated values of surface tension are shown in Figure A.4. As expected, the calculated values begin to deviate from the measured values for samples having greater than 15 wt% solids. The error bars on the calculated values indicate how the values would change if a different value of z is used in the calculation. The calculated points used z equal to 0.5 mm. The upper limit on the error bars represent the values that are obtained when $z = 0.3$ mm is used. The lower limit on the error bars represent the values that are obtained when $z = 0.7$ mm is used.

A plot of the surface tension versus time is shown in Figure A.5 for representative samples. This plot shows how the surface tension curves changed with varying solids content. Based on how these curves changed with time, decisions were made as to where on the curve the data should be averaged over to obtain the final result. Samples 1 through 7 were run for 5 minutes, with the data being averaged over the 5 minutes. As can be seen in Figure A.5, with sample 7 a slow decline in surface tension over time was seen. The remaining samples (8 through 15) were run for 10 minutes. As the solids concentrations went up in the samples, an initial steep decline in surface tension followed by a leveling off over time was reproducibly observed. Because of the steep decline in the value of surface tension for these measurements, the reported value of surface tension came from averaging the data over the last 2 minutes of each run for samples 8 through 15. The surface tension measurements provide a fairly reproducible method of understanding the behavior of the solids. Sample Clay_14 is plotted on the right y-axis because the measured surface tension was at much higher values than the other samples shown in the plot.

Table A.1. Measured Values of Surface Tension (mN/m) for Kaolin/Bentonite Clay Simulant Slurry

Sample Name	Total Percent Solids	Measurements of Surface Tension (mN/m)					Average Surface Tension (mN/m)	Standard Deviation
		A	B	C	D	E		
Clay_1	0.0	72.1	72.3	72.3	72.4	72.5	72.3	0.12
Clay_2	1.1	72.4	72.4	72.5	72.4	72.3	72.4	0.05
Clay_3	2.1	72.7	72.7	72.6	72.5	72.6	72.6	0.08
Clay_4	3.1	72.9	72.8	72.7	72.8	72.7	72.8	0.05
Clay_5	5.1	72.6	72.7	72.7	72.6	72.8	72.7	0.07
Clay_6	7.6	72.8	72.7	72.7	72.7	72.7	72.7	0.06
Clay_7	10.0	72.8	72.8	73.0	72.9	72.9	72.9	0.05
Clay_8	12.5	72.3	72.3	72.3	72.1	72.1	72.2	0.08
Clay_9	15.0	73.1	73.1	73.0	72.9	72.8	73.0	0.12
Clay_10	17.6	73.8	73.4	73.9	73.8	73.6	73.7	0.18
Clay_11	20.0	75.3	75.3	75.4	75.2	75.4	75.3	0.10
Clay_12	22.5	77.7	78.4	78.4	78.0	78.3	78.1	0.30
Clay_13	25.0	83.9	83.8	85.2	83.1	84.4	84.1	0.78
Clay_14	27.4	91.1	91.5	91.4	90.4	92.3	91.4	0.68
Clay_15	29.0	93.9	94.9	95.2	95.8	98.0	95.6	1.53

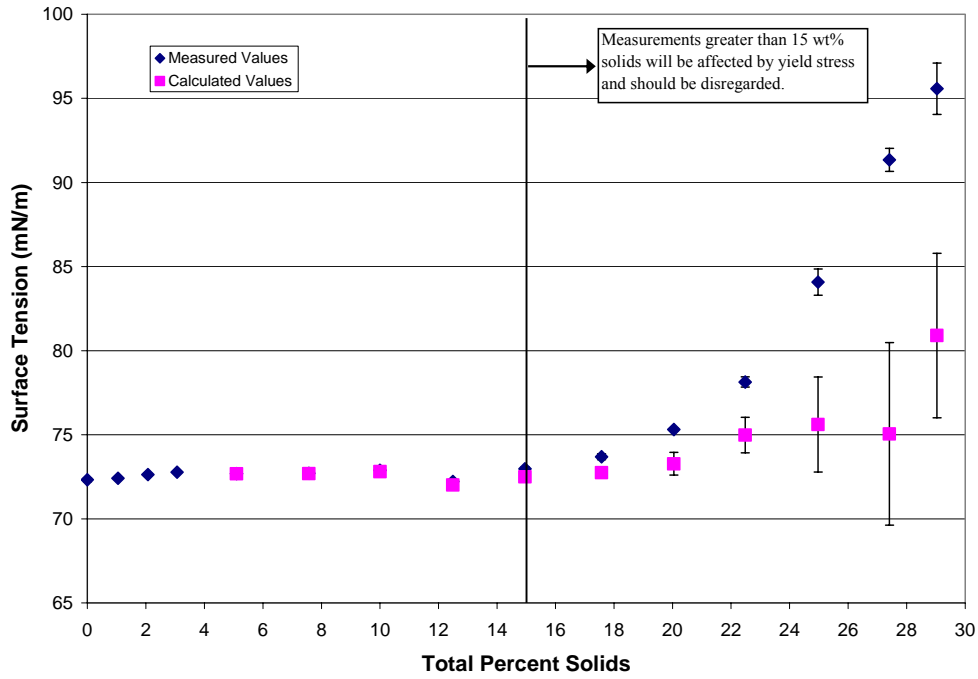


Figure A.4. Surface Tension of Kaolin/Bentonite Clay Simulant Slurry as a Function of Percent Solids

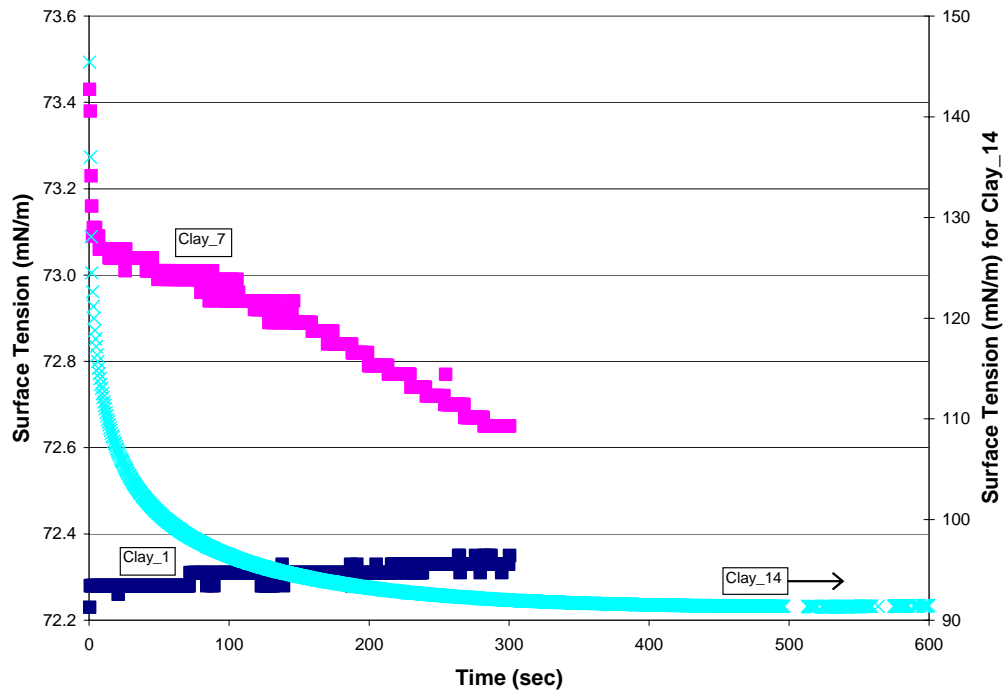


Figure A.5. Surface Tension of Diluted Kaolin/Bentonite Clay Slurry for Representative Samples. Clay_1 and 8 are plotted on the left y-axis, and Clay_14 is plotted on the right y-axis.

The surface tension of the simulated HLW slurry was measured for the ten diluted samples, along with a sample of the undiluted slurry and a sample of the liquid from the slurry. Four to five measurements were made on each sample. The results from each measurement, as well as the average surface tension and the standard deviation, are shown in Table A.2. The average surface tension values are plotted in Figure A.6. Error bars represent a single standard deviation. Samples containing less than 12 wt% solids had measured surface tension values of 73.1 – 74.4 mN/m. As determined above, the samples become non-Newtonian above 12 wt% solids. The measured values of surface tension in samples having more than 12 wt% solids are actually a combination of yield stress and surface tension.

Equation 8 was used to calculate the actual values of surface tension. Values were not calculated for the first four samples because yield stress measurements were not made on those samples. The calculated values of surface tension are shown in Figure A.6. As expected, the calculated values begin to deviate from the measured values for samples having greater than 12 wt% solids. The error bars on the calculated values indicate how the values would change if a different value of z is used in the calculation. The calculated points used z equal to 0.5 mm. The upper limit on the error bars represent the values that are obtained when $z = 0.3$ mm is used. The lower limit on the error bars represent the values that are obtained when $z = 0.7$ mm is used.

A plot of the surface tension versus time is shown in Figure A.7 for representative samples. The lower percent solids samples settled very quickly. Sample 1 was the liquid from the slurry, so it was run for 5 minutes and the data was averaged over the full 5 minutes of the run. Samples 2 through 5 settled within minutes, and only the first 30 seconds of data were averaged to obtain the values of surface tension. Samples 6 and 7 were each run for 5 minutes. Sample 6 began to settle in 5 minutes, so the average was taken of the first 3 minutes of data, and for sample 7, the average was taken of the first 4 minutes of the data. The remaining samples took longer than 15 minutes to settle, so surface tension was measured for longer times in order to allow the samples to reach a steady value of surface tension. Sample 8 was run for 10 minutes, and the average was taken of the last 5 minutes of the data. Samples 9 through 12 were run for 15 minutes, and because of the steep decline in the value of surface tension for these measurements, the reported value of surface tension came from averaging the data over the last 5 minutes of each run. Sample QARD_12 is plotted on the right y-axis because the measured surface tension was at much higher values than the other samples shown in the plot.

Table A.2. Measured Values of Surface Tension (mN/m) for Simulated HLW Slurry

Sample Name	Total Percent Solids	Measurements of Surface Tension (mN/m)					Average Surface Tension (mN/m)	Standard Deviation
		A	B	C	D	E		
QARD_1	0.0	73.4	73.5	73.5	73.6	73.7	73.5	0.12
QARD_2	1.1	72.9	73.0	73.2	73.2	73.4	73.1	0.19
QARD_3	2.0	73.5	73.4	73.5	73.7	73.6	73.5	0.10
QARD_4	3.0	72.6	73.1	73.3	73.5	73.5	73.2	0.39
QARD_5	5.0	73.2	73.4	73.6	73.8	73.8	73.6	0.25
QARD_6	7.5	73.5	73.7	73.8	74.0	74.0	73.8	0.21
QARD_7	10.1	73.9	73.9	74.0	74.0	74.0	74.0	0.08
QARD_8	12.5	74.4	74.5	74.5	74.4	NA	74.4	0.06
QARD_9	15.0	75.7	75.5	75.6	75.5	75.7	75.6	0.06
QARD_10	17.5	78.8	79.0	79.3	79.5	80.0	79.3	0.11
QARD_11	20.1	78.3	79.0	77.9	78.9	79.1	78.7	0.47
QARD_12	20.9	79.7	79.2	80.5	79.6	NA	79.8	0.54

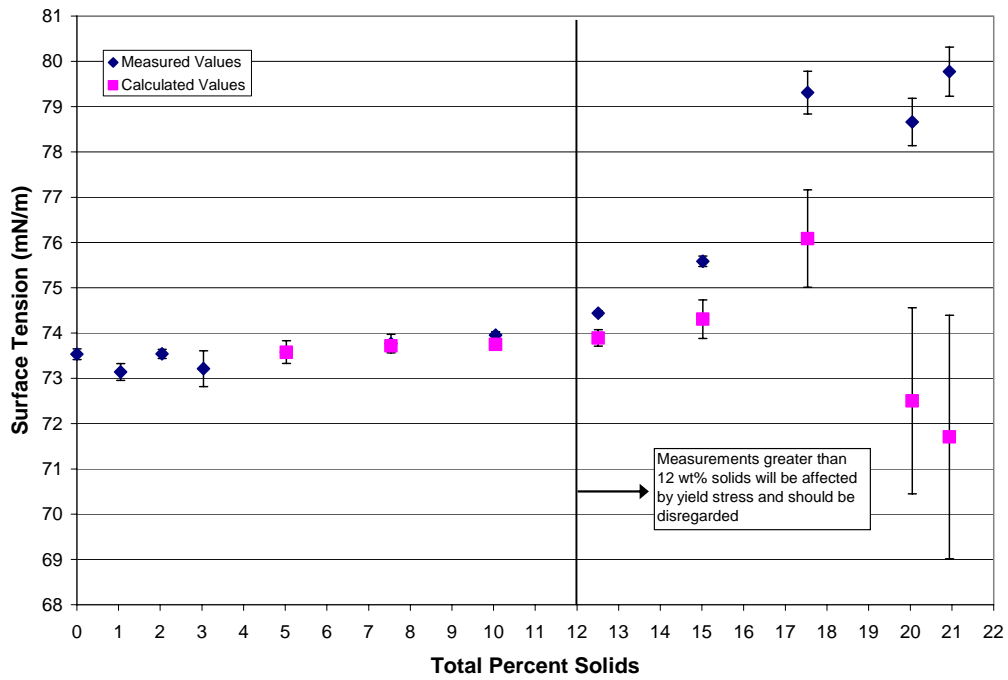


Figure A.6. Surface Tension of Simulated HLW Slurry as a Function of Percent Solids

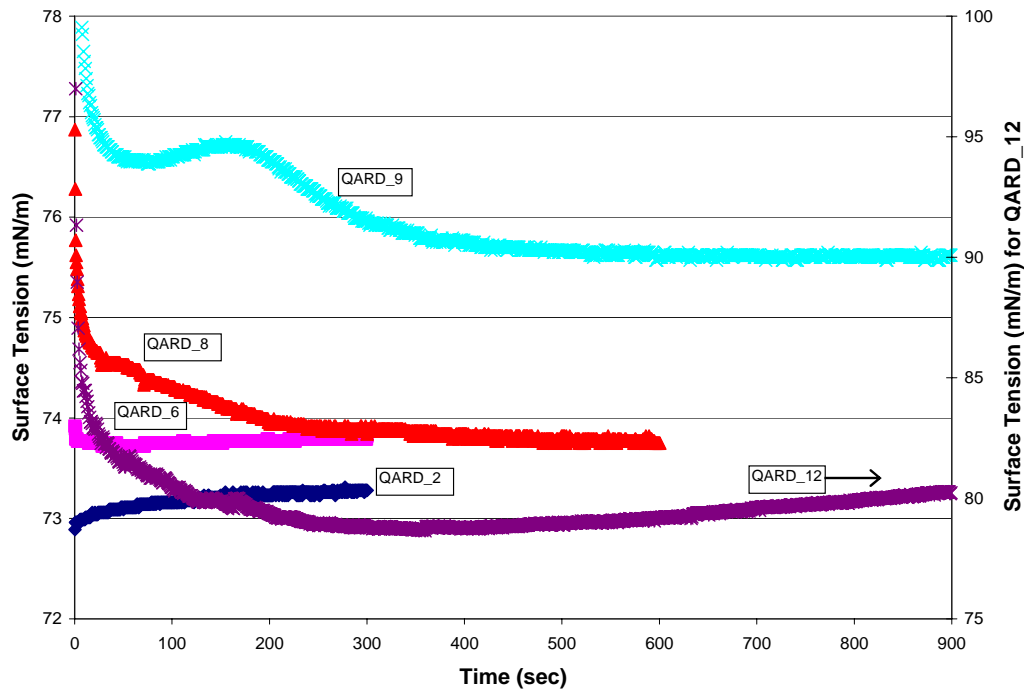


Figure A.7. Surface Tension of Diluted Simulated HLW Slurry for Representative Samples. QARD_2, 6, 8, and 9 are plotted on the left y-axis, and QARD_12 is plotted on the right y-axis

These two slurries, most notably the simulated HLW slurry, have dissolved salts in the interstitial liquid. Dissolved salts in water can change the surface tension of the liquid. Two of the main salts found in the simulated HLW slurry are sodium hydroxide (NaOH) and sodium nitrate (NaNO₃). Table A.3 shows how the surface tension changes as a function of weight percent of the two solutes in water (Lide, <http://www.amazon.com/exec/obidos/ASIN/0849304687/weisstein-20> 1991). These salts raise the surface tension of water. The sample of liquid from the simulated HLW slurry had a measured surface tension of 73.5 mN/m, slightly above the value of 72.75 mN/m for pure water. This slight deviation from pure water in the liquid from the slurry is due to the presence of these dissolved salts in the slurry. For the salts in water, the surface tension scales linearly with salt concentration. However, our measured values are nonlinear and do not follow this behavior.

Table A.3. Effect of Dissolved Solids Content on Surface Tension

Solute	Wt %	Surface Tension (mN/m)	Temperature (°C)
NaOH	2.72	74.35	18
NaOH	5.66	75.85	18
NaOH	16.66	83.05	18
NaOH	30.56	96.05	18
NaOH	35.90	101.05	18
NaNO ₃	0.85	72.87	20
NaNO ₃	4.08	73.75	20
NaNO ₃	7.84	73.95	20
NaNO ₃	14.53	75.15	20
NaNO ₃	29.82	78.35	20
NaNO ₃	37.30	80.25	20

Conclusions

Samples of Kaolin/Bentonite Clay and simulated HLW slurries were made at varying levels of solids concentrations. Surface tension and rheology measurements were made on the samples. It was seen that both surface tension and yield stress values begin to rise appreciably in both slurries when the samples have between 12 and 15 weight percent solids. At this point, the samples become non-Newtonian and the measured values of surface tension are actually due to both the surface tension and the yield stress. Using the measured values of surface tension and yield stress, the actual values of surface tension were calculated. As expected, it was seen that the calculated values begin to deviate from the measured values at 15 wt% solids for the Kaolin/Bentonite clay slurry and at 12 wt% solids for the simulated HLW slurry. The calculated values of surface tension account for errors due to yield stress in the slurries in the surface tension measurements.

For the Kaolin/Bentonite clay slurry, the measured values of surface tension were 72.2 – 73.0 mN/m for samples up to 15 wt% solids. The calculated values stayed in this range until samples reached 22 wt% solids, at which point the calculated values of surface tension began to rise. For the simulated HLW slurry, the measured values of surface tension were 73.1 – 74.4 mN/m for samples up to 12 wt% solids. The calculated values stayed in this range until samples reached 15 wt% solids. The sample containing 17.5 wt% increased above this range of surface tension, and samples containing 20 and 21 wt% solids decreased below this range.

The measured values of surface tension for both the Kaolin/Bentonite clay slurry and the simulated HLW slurry do not change much for the 0 to 12 wt% range. This indicates that the effect of solids on surface tension is small and the surface tension of the interstitial liquid can be used for slurry applications involving surface tension as a critical parameter.

References

Lide, D. R. (Ed.). Handbook of Chemistry and Physics, 72nd ed. Boca Raton, FL: CRC Press, 1991.

Thiessen, D.B., K.F. Man. 2000. "Surface Tension Measurement." In: *Mechanical Variables Measurement. Solid, Fluid, and Thermal*. Webster, J.G. (Ed.), CRC Press LLC, Boca Raton, Florida, p. 12-1 – 12-13.

Distribution

**No. of
Copies**

**No. of
Copies**

OFFSITE

ONSITE

1 Savannah River National Laboratory
Richard Edwards
Westinghouse SA
Aiken, South Carolina 29808-0001

22 Battelle—Pacific Northwest Division
S. T. Arm P7-28
J. A. Bamberger K7-15
B. Barnett K6-81
R. S. Brown K6-85
B. J. Cook P7-25
C. W. Enderlin K7-15
M. S. Fountain P7-27
M. Friedrich K5-16
B. G. Fritz K6-75
D. E. Kurath P7-28
R. P. Mueller K6-85
F. Nigl K7-15
Y. Onishi K7-15
A. P. Poloski P7-25
L. A. Schienbein K5-20
L. A. Snow P7-22
S. Tzemos K7-22
M. White K7-15
Project Office (2) P7-28
Information Release (2) P8-55

8 Bechtel National, Inc.
H. Abodishish H4-02
A. S. Bronner H4-02
S. M. Barnes H4-02
C.E. Corriveau, Jr. H4-02
J. F. Doyle (2) H4-02
D. Larson H4-02
G. L. Smith H4-02